Effect of Encapsulation and Light-soak on Charge Transport Properties in Organic Semiconductor –based Diodes

Sanyasi Bobbara

UNIVERSITE BRETAGNE LOIRE

université angers

Thèse de Doctorat

Sanyasi Rao Bobbara

Mémoire présenté en vue de l'obtention du
grade de Docteur de l'Université d'Angers
sous le sceau de l'Université Bretagne Loire

École doctorale : *3MPL*

Discipline : *Physique*
Spécialité : Optique
Unité de recherche : *UMR 6200*

Soutenue le *22 septembre 2017*
Thèse N° : *(10)*

Effect of Encapsulation and Light-soak on Charge Transport Properties in Organic Semiconductor –based Diodes

JURY

Rapporteurs :	**Dr. Gregory Jerkiewicz**, Professor, Queen`s University
Examinateurs :	**Dr. Jun Gao,** Professor, Queen's University, Ontario, Canada **Dr. Clara Santato**, Professor, École Polytechnique de Montréal, Québéc, Canada **Dr. Kevin Stamplekoskie**, Assistant Professor, Queen's University, Ontario, Canada
Invité(s) :	**Prof. Marc Dignam**, Head of the Department of Physics, Queen's University, Ontario, Canada
Directeur de Thèse :	**Jean-Michel Nunzi**, Professor, Queen's University (Canada)
Co-directeur de Thèse :	**Régis Barillé**, Professeur, Université d'Angers

Abstract

Organic semiconductors (OSs) have garnered a great attention in the recent years due to their ease of processibility, optical and electrical property-tunability, and to their cost-effectiveness. They form the class of materials most suitable for flexible electronics and bioelectronics, especially in association with solution-processable inorganic/hybrid materials. However, the charge mobility in these materials is strongly affected by their structural and energetic disorder introduced by the defects that 'trap' the charge carriers. Depending upon the physical location of the traps and their distribution in energy, they could significantly affect the charge transport in a device. The present work strives to probe the interface and bulk defect states in polymer-based diodes. In lieu of that, a part of the study involved characterizing the device with and without encapsulation, using techniques to record steady-state current-voltage (I-V) behaviour, transients of charge extraction by linearly increasing voltage (CELIV) and dark-injection transient currents (DiTC), as well as photoluminescence (PL) and electroluminescence (EL) off the devices. The same characteristics have been carried out to observe the effect of ultra-violet (UV) light-soak on the devices. All the tests were performed on three different polymers, namely P3HT, MDMO:PPV and PCDTBT. The comparison of the encapsulated versus unencapsulated devices gives an insight into characteristic differences in the measurables upon exposure to air and

moisture. The light-soak tests indicate the modification of the cathode work function after a UV-assisted oxygen desorption off the polymer/cathode interface. A simultaneous effort went into an in-situ investigation of charge transport dynamics in organic semiconductors over wide time range at a microscopic scale.

Co-Authorship

All the P3HT-based and P3HT:PCBM-based samples were fabricated by me, while the devices based on PCDTBT and MDMO:PPV were fabricated by my colleague/visitor from Egypt, Mr. Ehab Salim. All the tests and analysis for all the devices were performed solely by me.

Contents

List of Tables

List of Figures

Acronyms

AFM Atomic Force Microscopy.

APD Avalanche Photodiode.

BHJ Bulk-Heterojunction.

CELIV Charge Cextraction by Linearly Increasing the Voltage.

CT Charge Transfer.

DiTC Dark-injection Transient Current.

EA Electron Affinity.

EL Electroluminescence.

EPR Electron Paramagnetic Resonance.

FB Forward Bias.

HCTE Hybrid Charge Transfer Exciton.

IPCE Incident Photon-to-Current Efficiency.

IPES Inverse Photoelectron Spectroscopy.

ITO Indium Tin Oxide.

KPM Kelvin Probe Microscopy.

LBIC Laser Beam Induced Current.

LSPR Localized Surface Plasmon Resonances.

MIM Metal-Insulator-Metal.

MO Metal Oxide.

MTR Multiple Trap and Release.

OECTs Organic Electrochemical Transistors.

OEIPs Organic Electronic Ionic Pumps.

OFET Organic Field-Effect Transistors.

OLED Organic Light Emitting Diode.

OS Organic Semiconductor.

P3HT Poly(3-hexylthiophene-2,5-diyl).

PCBM Phenyl-C61-butyric acid methyl ester.

PL Photoluminescence.

RB Reverse Bias.

RFID Radio Frequency Identification.

SCLC Space-Charge Limited Current.

TAS Transient Absorption Spectroscopy.

TCS Thermally Stimulated Current.

UPS Ultraviolet Photoelectron Spectroscopy.

Chapter 1

Introduction

1.1 Semiconductor Electronics

Semiconductors are a class of materials that conduct electricity under favourable conditions which otherwise are insulators. Conventionally, insulators are considered to be 'high-resistivity' and 'wide-optical-bandgap' materials at room temperature, to distinguish it from the 'low-resitivity' under proper ohmic contacts and 'narrow-bandgap' semiconductors. Some of the fascinating findings of semiconductors in their inception were Faraday's observations of negative temperature coefficients in 'Sulphuret of Silver'[1], photovoltage by shining light on the surface of one of the electrodes of the battery cell measured by Bacquerel[2] and the enhanced conductivity upon light exposure on Selenium[3] discovered by W.Smith to mention few. A proper understanding was not given until the formulation of Quantum mechnanics in the early twentieth century.

Inorganic semiconductors, especially Silicon (Si), Germanium (Ge), gave a kickstart to the high speed electronics that we use today. The revolutionary invention of the transistor based on polycrystalline Ge in 1947 by Bardeen, Brattain and Shockley

[4, 5] has enabled a precise control of the electricity. With the ability to control the crystallinity, purity and dopant concentration in these materials, it has made these semiconductors superior material in the industry of electronics. Although Ge was the first material the transitor was built upon, Si has superceded Ge in terms of applicability owing to its abundance and its higher breakdown field endurance. Also the relatively higher bandgap of Si leads to a lower dark current due to thermal charge carriers. Doping Si was also a lot easier than Ge, as Si has the ability to form SiO_2 readily, which in turn helps protecting the dopant atoms. From that point on, most of the research and development went in purifying, improving switching speeds, reducing the size and integrating with many components on a chip for compactness. This goes on to show how the significance of stability and cost play a key role in a product's sustainability.

With the constantly increasing dependence on automated commodities and the fast-depleting non-renewable energy resources, any additional sources of useful energy and/or storage devices are sought the most at this point of time. Needless to point out the impact of burning the fossil fuels has on the environment. One of the promising sources to counter these issues is solar energy.

The electricity generation using sunlight, based on Si, came into practicality in 1954 from Bell Labs [6]. Largest share of the current market is dominated by silicon based solar cells. Other thin-film based devices include a-Si, CdTe, GaAs, InGaAs, $\mathrm{Cu(In,Ga)Se_2}$ (CIGS), which fill up rest of the photovoltaic market share. However they do come with some setbacks and concerns. For example, Indium and tellurium are scarce and expensive, cadmium is toxic (although CdTe, being highly stable product, is not toxic), a-Si suffers from low carrier mobility, GaAs demands high purity

for lattice matching in the case of multilayered devices etc. Although a-Si has a relatively lower mobility, a-Si devices did find a place in the current market due to their low-cost of production. Unlike c-Si, the a-Si can be deposited in the form of thin films $(1-2)\mu m$ at relatively low temperatures. This opened up the possibility of depositing them on flexible substrates and over large areas. There is a constant drive for flexible and large-area production towards the 'printable electronics' to further cut down the cost[7]. Other potential candidates that fit into this spectrum are based on small molecules, polymers, ceramics (most recently, the Perovskites), semiconducting quantum dots - commonly termed as third generation photovoltaic materials.

Alongside are another elite group of compounds called metal oxides like ZnO, TiO_2, MoO_3, V_2O_5 etc[8]. that are transparent in the optical spectrum. Their tunable conductivity and the advantage of being processed in the form of solution makes them a promising category of compounds towards printed-electronics. Other areas of technological advancements in hybrid electronics include displays based on electrophoretics [9, 10, 11] and Organic Light Emitting Diodes (OLEDs) [12], flexible batteries [13, 14], Organic Field-Effect Transistors (OFETs) [15], Radio Frequency Identification (RFID) tags [16, 17], and more recently in bio-electronics, to mention a few. Organic Semiconductors (OSs), although quite promising, come with setbacks especially with the controlling the defect states that trap charges, fast aging and stability.

Some of the (semi-)conducting polymers like polypyrrol (PPy), poly (3,4-ethylene dioxythiophene) (PEDOT), polyacetylene (PA), polythiophene (PT), polyaniline (PANI) etc., showed great potential in biological applications. In order to monitor, control

and treat some of the biomedical issues, especially in-vivo, the organic-based electronic devices are the top priority. Their soft mechanical properties would make them compatible with the soft biological tissues; their ease of chemical modification helps to optimize case-specific changes. For example, Organic Electronic Ionic Pumps (OEIPs)[18, 19] is used to transfer ions between two ion reservoirs electrophoretically. In another application, Organic Electrochemical Transistors (OECTs) based sensor[20, 21], the conductivity of across source and drain is controlled by doping/dedoping the conducting polymer, ex. PEDOT:PSS, which is in contact with the electrolyte by varying the bias to the electrolyte. A very good review of the concepts and applications based on the organic conductors/semiconductors towards organic bio-electronics has been put together in the book by Fabio Cicoira and Clara Santato [22].

Clearly organic electronics seems to hold an optimistic future. But it is also clear that unless they are cheaper, stable in behaviour and last longer, they may not persevere in the market. The present work is focussed towards improving the stability and longevity of the semiconducting polymers by understanding the charge transport dynamics and the effect of bulk/interface defect states in the devices based on polymers.

1.2 Motivation

The motivation behind the project was to study the spatial and energetic location of defects states and how they would affect the charge transport in the organic semiconductors. Most of the photovoltaic devices based on either Bulk-Heterojunction (BHJ) or bilayered or organic-inorganic hybrid type devices are commonly studied

to improve their device efficiency. The present work however started with an intent to understand one layer of active medium. This obviates the complexity of the structure and helps disentangling the contributions of bulk from the interface affects. Poly(3-hexylthiophene-2,5-diyl) (P3HT) was chosen to start with considering its already well-documented tests and hence it would serve us calibrate our measurements and devices as well.

For a stable polymer like P3HT the measurements, like current-voltage characteristics, changed over time when left inside the glovebox and even more drastically when the tests were being performed outside the glovebox over extended periods of time. In order to understand and distinguish the trap states due to extrinsic entities like O_2 and moisture from the intrinsic defects, the devices were studied both with and without encapsulation. On a substrate with four devices, two of the devices were encapsulated while the other two were not encapsulated. The encapsulation has also enabled us to do multiple optical studies on the encapsulated devices with minimal photodegradation of the active medium.

In order to speed up the process of degradation and/or oxidation of the polymers, thereby modifying the trap states distribution, it was decided that the devices be soaked under white light.

1.3 Layout of the Thesis

The Chapter 2 is a concise description addressing upto date literature review relevant to materials and devices that were used in this work, as well as different characterization techniques with an emphasis on the physics behind the techniques. A significant portion of time that went towards device fabrication, caliberations, data acquisitions

and building techniques to probe the device are detailed in Chapter 3.

Chapter 4 gives detailed tests, results and discussion on P3HT-based sandwich-type diodes. The tests include the study of effect of encapsulation on the steady-state dark current-voltage and dynamics through the Charge Cextraction by Linearly Increasing the Voltage (CELIV) and Dark-injection Transient Current (DiTC) characteristics, along with Photoluminescence (PL) and Electroluminescence (EL) studies as well. Further the same tests were performed to observe the effect of soaking the devices under white and UV light. P3HT:PCBM-based devices were also tested in order to compare the effect of unintensional defects induced by external factors to that intensional electron traps and structural disorder introduced by adding PCBM acceptor molecules.

Chapter 5 does a comparative study using P3HT, MDMO:PPV, PCDTBT polymers with the same layered configuration as were used in Chapter 4. P3HT and MDMO-PPV are of nearly same conduction edges but with an offset in the valence band edges. PCDTBT is a low bandgap material with relatively deeper conduction and valence band edges. The relative energy levels of the conduction and valence bands with respect to the fixed contact work functions would help us identify the plausible interface barriers. Each polymer has a different chemical structure and hence different molecular conformation/morphology in a thin film; degree of crystallinity and hence different glass transition temperatures. Comparision of the above polymers and other kinds have been performed by Mateker et al. [23] in terms of photostability and degradation. The work presented in this chapter forms only fraction of the complete picture considering the wide range dissimilarities of the three polymers. However, the intention was towards finding the physical properties in terms of charge

mobilities, dielectric permittivity, impact on the current voltage characteristics as well as charge storage capacity from CELIV, interfacial properties etc. and to rule out any insignificant possibility whereever possible, in order to simplify the overall understanding.

Chapter 6 is constituted of all-imaging based on bright-field, fluorescence and Laser Beam Induced Current (LBIC) on the above mentioned devices to check for the effect of encapsulation like top-electrode pinholes and edge degradation, and UV illumination. There are four appendices attached towards the end, in which Appendix B and Appendix C describe the steps taken to calculate the charge mobilities from space-charge limited current regime in I-V characteristics and CELIV, respectively. The intention was also to highlight some of the difficulties and pitfalls associated with the extracting the charge mobilities out of the so-called 'simple' techniques. Appendix A and Appendix D include some supporting information in the aide of Chapter 4 and Chapter 5, respectively.

Chapter 2

Background

2.1 Organic Semiconductor Electronics

The electrical conductivity in an organic material is believed to be envisioned and first realized by D.D. Eley in 1948 [24], followed by a systematic work of Akamatu and Inokuchi [25, 26] which paved the way further towards organic semiconductor studies. A very good compilation of analytical and experimental study of current injection in solids like in valence crystals, ionic crystals, organic and inorganic molecular crystals has been presented in the book called 'Current Injection in Solids' by Lampert and Mark [27]. While there was no mention of conducting polymers in the book, polymer electronics started gaining attention after Shirakawa's accidental findings of conduction in doped Polyacetylene.The book on 'Conjugated Polymers and Molecular Interfaces' by Salaneck,Seki and Kahn[28], is a great resource on giving an overview of most of the experimental observations and techniques employed on understanding the role of the organic-organic and organic-contacts interfaces.

C.W. Tang [29] fabricated the first bilayered organic solar cell of about 1% efficiency. A major problem with those organic solar cell was that the exciton diffusion

length was less than 20nm and hence exciton recombination losses would dominate over the charge dissociation. This problem was addressed by A.J. Heeger group [30] by blending the acceptor molecules and donor polymer making Bulk Heterojunction (BHJ) cells. This increases the probability of finding the interfaces for the exciton dissociation, showing an improved efficiency of about 3%. Since then a lot of research has gone into optimizing the cells in terms of material and morphology. For example, selecting appropriate solvent and/or annealing of the solution-processes polymer:molecule blended solar cells lead to a better morphology [31]. Likewise in plasmonic solar cells, the emphasis is on scattering the incident light by the localized surface plasmon resonances into the active medium [32] is another such strive. Synthesizing stable low bandgap polymers for PVs in order to cover long wavelength spectrum of sunlight is another interesting topic of research [33]. Conduction in organic semiconductors originates from the alternating double bonds along the chain of the polymer or in a molecular unit. The interaction between the neighbouring molecular units of a polymer leads to the opening up of the band gap and the improved conductivity is due to the delocalization of charges over the overlapping $\pi - \pi$ orbitals. A very small energy difference between the two configurations where the double-bond could prevail on either, but one, side of a carbon atom at a time, leads to a state of degeneracy where the conduction without barrier can be assumed. Figure 2.1 shows one such polymer called polyacetylene with two possible configurations. Note that there are also conjugated polymers that can take non-degenerate configurations.

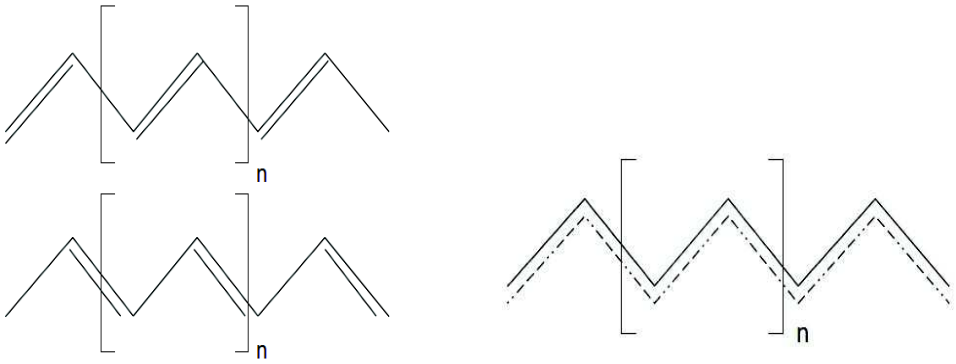

(a) (b)

Figure 2.1: Skeletal formula of polyacetylene showing (a) two probable energetically favoured configurations, (b) superposition of two equally probable configurations.

In contrast to the conjugated polymers, polymers like polyvinylene, polyallenes etc. behave like an insulator in the absence of conjugation. The relatively longer single bonds lead to lesser interaction between the basic units and hence minimal dispersion in energy levels, leading to a larger energy gap. The conduction and valence bands originate from the bonding structure of the polymers. In contast to their inorganic counterparts, the band edges of organic semiconductors are usually not sharp but instead they have tail states leading into the band gap. The tail states arise from the intrinsic defects arising from the morphological disorder and differences in local conditions that are ubiquitous to the amorphous nature of these polymers. There can be unintentional extrinsic defects introduced before, during or post synthesis that leads to mid-gap deep or shallow states [34]. Figure 2.2 shows a cartoon of density of states distribution in energies in amorphous semiconductors in general.

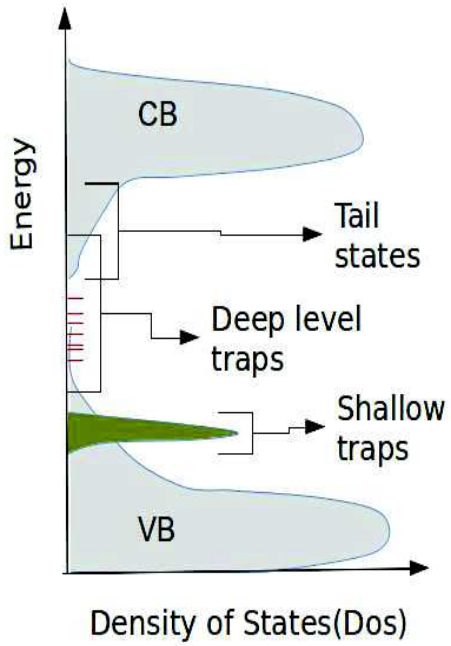

Figure 2.2: A schematic of the distribution of energy levels in amorphous solids. CB- Conduction band, VB- Valence Band

Semiconducting polymer DoS

In order to understand the charge transport in these semiconductors better, it is necessary to identify the conduction(valence) bands as well as the spatial and energetic location of the trap states. Ultraviolet Photoelectron Spectroscopy (UPS) [35, 36, 37] and Inverse Photoelectron Spectroscopy (IPES) [38, 39] techniques are often used to identify the occupied and unoccupied energy states respectively. To determine the gap states at the interface or bulk, tests have been done in either frequency-domain [40, 41, 42], time-domain [43], or temperature-controlled steady state [44]. Impedance spectroscopy to reconstruct the trap-DoS in which a very small ac signal perturbation is frequency-swept at various dc biases. MacKenzie et al. [43] used transient photocurrent after a short optical pulse excitation to relate to the DoS of

P3HT:PCBM based devices. It is very well understood now that molecular oxygen physically adsorbed to the conjugated polymers can affect polymer's conductivity, where in most of the cases, act as a p-type dopant and/or as a mid-gap trap statess. The electron affinity of O_2 molecule is known to be about $(0.451 \pm 0.007)eV$ [45], and the ionization potential of most of the semiconducting polymers is between (5-6) eV. The Electron Affinity (EA) values of the O_2 in a polymer or its surface is different from its value measured in gaseous, as the solid-state polarization effect due to the surrounding material[46] needs to be taken into consideration.

The relatively weaker covalent bonds in polymers make them susceptible to photo-oxidation and -degradation. Depending on their packing structure i.e. morphology during film formation, or side chains that are modified to enhance their solubility in a solvent and/or the functional groups attached to the polymer backbone, the rate of these processes might vary. Photoxidation is the process where the polymer gets oxidized in the presence of light. Photooxidation could be a reversible process i.e. the initial state of the polymer could be retracted by using some processes like thermal annealing or by vacuum pumping. However, prolonged exposure to light and oxidizing agent may lead to irreversible photodegradation.

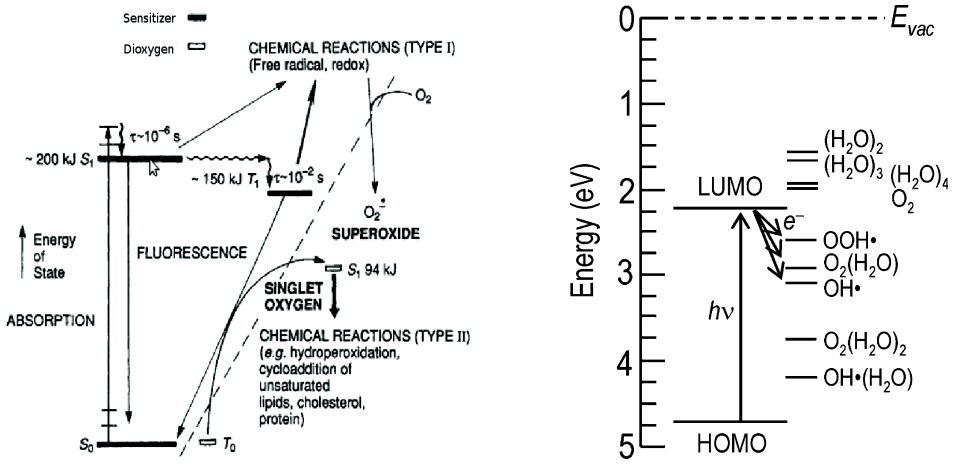

(a) (b)

Figure 2.3: a) Jablonski diagram indicating routes of energy and charge exchange phenomena between the sensitizer and an oxygen molecule [47], b) Energy levels of various species associated with oxygen and water with respect to the energy levels of the Polymer. Picture courtesy [46].

There have been studies already done in detail to understand the process of photooxidation and degradation [48]. For example, the electrophilicity of the molecular oxygen and the nucleophilicity of the Sulphur atom in P3HT leads to a Charge Transfer (CT) complex, when the two entities are in proximity. This was confirmed from the increase in Electron Paramagnetic Resonance (EPR) signal of P3HT in the presence of O_2 , and the effect was reversible[49]. The increase in signal is indicative of the ionic character of the complex. The charge transfer complex formation of P3HT with oxygen is shown in Figure 2.4(a). The photolysis of this complex, can lead to generation of singlet oxygen $^1O_2$ or superoxide ions ($O_2^{\cdot -}$) which can further lead to reversible or irreversible change to the CT state, as shown in the Figure 2.4(b). The common consensus to date is that singlet oxygen is the key culprit in expediting the polymer degradation process.

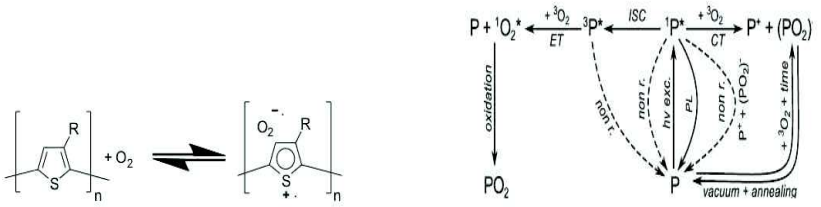

(a) (b)

Figure 2.4: a) Representation of Charge-Transfer complex of P3AT and oxygen [49], b) Possible routes of chemical mechanisms involved in photolysis of a polymer in the presence of molecular oxygen.[50].

Mechanism Photo and thermo-oxidation of P3HT was revisited by Manceau et al [51]. Based on the infrared and UV-visible spectroscopy, the authors conclude that the singlet oxygen doesn't play a key role degradation mechanism, but instead it was proposed that the oxidation of the side chains and followed by the degradation of thiophene rings.The energetic location of these trap states would mostly determine the overall device behaviour, and it is very important to include their contribution in the physical model.

Different models have been proposed in order to describe the charge transport in organic semiconductors. One of them being Multiple Trap and Release (MTR) model, according to which, the charge remains trapped in a defect but with a non-zero probability of being excited to a continuum of states of the semiconductor, before being trapped again by the defect. The propagation direction is decided by the bias applied. The escape probability of the trapped electrons (holes) into the continuum of states depends on the energy difference between the trap level and the conduction (valence) band [52]. Hopping or percolation theory of conduction is the another model in which the charge instantaneously hops between the neighbouring localized states [53, 54].

A comprehensive review on the charge transport is given by Schmechel et al. [34] and Klauk Hagen [55]. Experimentally, performing multiple techniques in conjunction is the way to go to describe the charge transport in these disordered materials correctly and consistently. It is quite important to track the dynamics ranging from ultrafast sub-femtosecond phenomena like charge creation and separation to very slow detrapping phenomena that range upto few seconds or even days. While varying strength of the external perturbation in the form of optical or electrical pulses and probing the relaxation processes is one of the ways, probing by varying the temperature or pressure or even the gas type of the ambience are other commonly employed tests. What follows next is a very brief description of some of the commonly used techniques employed to charaterize the devices and physical phenomena ascribed to the characteristics observed so far.

2.2 Characterization techniques and the device physics

2.2.1 Current-voltage characteristics in dark

Figure 2.5(a) below shows current-voltage characteristics in semi-logarithmic scale for one of the diodes studied. The device is constituted of ITO/ZnO/P3HT/MoO_3/Ag on a glass substrate, Zinc Oxide (ZnO) is hole-blocking layer and Molybdenum Oxide (MoO_3) helps forming an ohmic contact to the polymer. In the forward bias, the top metal contact (Silver, in this case) participates in hole-injection and Indium Tin Oxide (ITO) forms the hole-collection side of the device making it a 'hole-only' device at small voltages (about less than 2V). In the reverse bias, the ZnO prevents from any hole-injection from the ITO side into the device, although there is some leakage current.

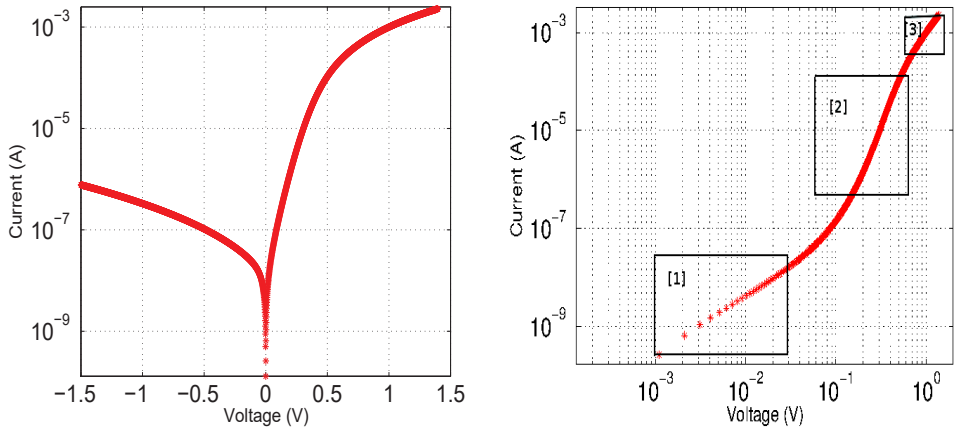

(a) (b)

Figure 2.5: Current-Voltage characteristics in a) semilogarithmic scale, and b) log-log scale where [1] represents the ohmic regime, [2] represents the diffusion- and trap-limited regime and [3] represents trap-filled SCLC regime.

Ohmic Regime

In ohmic regime, denoted by (1) in the Figure 2.5(b), the current is mostly dominated by the intrinsic thermally generated carriers, possibly from intentional or unintentional donors whose energy levels are shallow with respect to the valence band.

From the Ohm's law,

$$J = ep_0\mu(V/L) \tag{2.1}$$

where p_0 is thermally generated free hole concentration, μ is the hole mobility, L is the device thickness and V is applied bias voltage. The ohmic behaviour terminates when the injected charges are comparable to the thermally-generated charge density, p_0. In a more recent work, similar behaviour was shown to be followed by an insulator [56] due to the diffusion current component although the current density varies inversely proportional to L^3 and not to L as in equation2.1. By measuring the charge and

current densities using CELIV technique, one can measure the charge mobility in the ohmic regime using Equation 2.1.

Diffusion-limited Current/trap-assisted regime

The diffusion current for a P-N junction type device is given by the classical Schockley diode equation [57] is well known.

$$J = J_0[e^{(qV/\eta kT)} - 1] \tag{2.2}$$

where J_0 is the reverse saturation current, and η is the ideality factor. For a Metal-Insulator-Metal (MIM) kind, the current-voltage dependence is given by [57],

$$J = \frac{q\mu N_v(V_{bi} - V)[e^{(qV/kT)} - 1]}{L[e^{(qV_{bi}/kT)} - e^{(qV/kT)}]} \tag{2.3}$$

Space-charge Limited Current regime

Beyond the Ohmic regime, the voltage is high enough such that the transit time for the charge injected to traverse the device, $L/(\mu V)$, is shorter than the dielectric relaxation time, (ϵ/σ), the device enters the deep trap filling regime followed by space-charge limited regime. Charges injected and extracted ohmically is now only limited by the uncompensated space-charge inside the device i.e. the charge being injected experience an opposing field from the charges already present in the device. The current-voltage characteristic follow the Mott and Gurney's law (2.4) for a trap free insulator where current through the device is proportional to the square of voltage.

$$J = (9/8)\epsilon_0\epsilon_r\mu_0(V^2/L^3) \tag{2.4}$$

The regime 3 in Figure 2.5(b) shows the current and voltage proportionality with slope of about 2. The above equation assumes that the injecting/extracting contacts are ohmic and that there is no built-in field due to difference in work functions of the electrodes. This is accounted for by replacing the bias voltage, V, in equation2.4 by $V - V_{bi}$, where V_{bi} is the built-in voltage

Considering only a single shallow trap level close to the conduction (valence) band, the current-voltage characteristics are modified to the following equation (2.5),

$$\begin{aligned} J &= (9/8)\epsilon_0\epsilon_r\mu_0\theta(V^2/L^3) \\ \text{where, } \theta &= \frac{n_{trap}}{n_{trap} + n_{free}} \end{aligned} \tag{2.5}$$

Introducing a discrete shallow traps is a very simple case, although in general there could be a distribution of traps states. For example, the current-voltage characteristics derived for the case of exponential distribution of trap states, the space-charge current-voltage characteristics follow the equation (2.6)

$$J \propto V^{l+1}/L^{2l+1} \tag{2.6}$$

where $l = T/T_t$ and T_t is the temperature parameter that describes the exponential trap distribution such that $N_t(E) = N_0 exp[(Ev - E)/kT_t]$. N_t is the concentration of traps per unit energy, and E_v represents the energy level of the valence band edge. The parameter l is derived for the gaussian distribution of traps by Steiger et al. [58]. However it was observed in some cases that the slope is more than 2, which has been explained based on Murgatroyd's work [59] that considers the field-dependence of

mobility. An exponent of 3 is reported to be seen in the case pure insulators [60].

$$J \simeq (9/8)\epsilon\mu_0(V - V_{bi})^2 exp(0.89\sqrt{((V - V_{bi})/E_0 L)}))/L^3 \tag{2.7}$$

It has also been shown theoretically by Roichman et al. [61] and experimentally by Tanase et al. [62] and Pasveer et al. [63] that carrier mobility strongly depends on charge carrier density. According to their work, while at room temperature the charge mobility depends on the charge density, at lower temperatures and higher electric fields, the charge density dependence on the field is significant.

The above discussion on SCLC assumes that there is single carrier injection (extraction) hence the radiative recombination has not been considered. However, it is also of great interest to know the SCL current-voltage characteristics in the case of double-carrier injection followed by recombination processes. Paramenter et al.[64] showed that Mott-Gurney's law of SCLC for single-carrier injection case can be extended to the double-carrier injection case by just replacing with the effective mobility that is a function of electron and hole mobilities. Theoretical work Lampert et al. [60] on the reduced SCLC due to recombination processes and higher ohmic current due to enhanced minority carriers has been supported by my experimental work (Chapters 3 and 4) in polymer-based diode.

2.2.2 Current-Voltage characteristics under light

Most of the work presented in this thesis is aimed at understanding the physics of organic semiconductors. However the idea behind initiating the project was to understand and improve the material characteristics, in order to enhance the photovoltaics

efficiency. Here I would like to introduce some of the device's most common characteristic parameters, so that one can appreciate the significance of these parameters in the future discussion.

The mechanisms prior to observing the photocurrent off a solar cell can be categorized into following sequence:

- Exciton generation
- Exciton diffusion
- Exciton dissociation
- Charge carriers transportation/extraction

Photons absorbed by the active medium in a solar cell create electron-hole pairs called excitons. The excitons must be able to diffuse to the nearest donor:acceptor interface for dissociation. The excess energy i.e. the difference between the LUMO(or HOMO) of donor and the LUMO(or HOMO) of acceptor, should be large enough to overcome the binding energy of an exciton. At the interface the exciton splits into free charge carriers to be transported to the respective electrodes with the help of built-in field created by the difference in electrodes' work functions. Therefore it is important to chose electrodes for optimum performance of the device. These processes are shown in Figure 2.6.

Organic materials have very high absorption coefficients in the order of $\sim 10^5 cm^{-1}$ in the visible spectrum, allowing very thin active medium of about (100-300) nm to absorb a large fraction of incident photons. One of the setbacks in organic semiconductors however is that most of them have large bandgap but narrow absorption width. Hence only a small fraction of higher energy of optical spectrum overlaps with

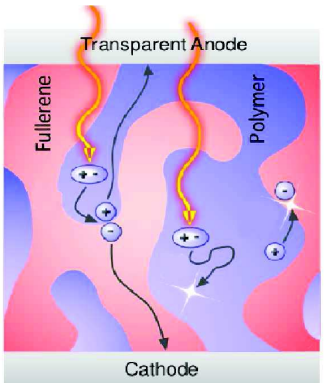

Figure 2.6: A cartoon depicting the mechanisms of exciton generation, diffusion, dissociation and charge recombination/transportation. Reprinted with permission from [65]

Solar spectrum. Some material engineering in this regard is being investigated to cover up for the loss, for example, by introducing metal nanoparticles in the active medium to enhance the absorption through Localized Surface Plasmon Resonancess (LSPRs), or by making multilayer cells with various low-bandgap material [66] etc.

Unlike in inorganic material, the binding energy of excitons in Organic materials is as high as (0.5-1)eV due to weak screening between charges offered by low effective dielectric constant (3-5 as compared to ~ 12 for silicon). In addition, the amorphous nature of organic materials leads to shorter (few tens of nanometers) exciton diffusion length. The problem of short diffusion length is circumvented in BHJ photovoltaics by making the blend of donor:acceptor material types such that the two material interfaces are available within the average diffusion length.

A serious limitation of BHJ OPVs is that there is a huge disorder in the blend and the acceptor/donor do not always percolate towards the right electrode. Therefore a fraction of the dissociated charges may end up unextracted and eventually recombine with some trapped charges from earlier excitations. A common fix to this

kind of situation is introducing charge-selective layers between the active medium and electrodes. Although these layers do not prevent the flow of 'uninvited' charges to an electrode, but instead mitigate the recombination losses which is prominent at the direct polymer-electrode contacts due to surface defects. The photogenerated charges that make their way to the electrodes are obtained as usable external current. In short, for a very efficient photovoltaic device, the absorption spectra of the active medium should cover the wide portion of solar spectrum, a very efficient exciton dissociation, and as least recombination losses as possible before reaching the electrodes.

A commonly presented figure of merit describing a solar cell behaviour is the Power Convertion Efficiency (PCE). PCE is defined as ratio of maximum extractable electrical power for the incident optical power. The efficiency of a solar cell is measured under standard conditions known as AM1.5 spectrum which simulates the solar spectrum on Earths surface,and it is given by.

$$\text{Efficiency}, \eta = \frac{FF * V_{oc} * I_{sc}}{P_{in}} \tag{2.8a}$$

$$\text{Fill-Factor,FF} = \frac{V_{max} * I_{max}}{V_{oc} * I_{sc}} \tag{2.8b}$$

From the definition, some of the important parameters are open-circuit voltage(V_{oc}), short-circuit current density (J_{sc}) and the product $V_{max}J_{max}$, the maximum extractable power, as indicated in the figure 2.7. The fill-factor is dictated by the series resistance (injection barriers and sheet resistances) and shunt resistance(for instance, charge losses due to recombination and charge transport to unintended electrodes). For a high-performance solar cell, the slope correnspondingto R_s should be as low as

possible and the slope at zero bias should be as flat as possible for a high R_{sh}. One should aim to improve the J_{sc}, V_{oc}or$J_{sc} * V_{oc}$ alongside the fill-factor for a better cell performance.

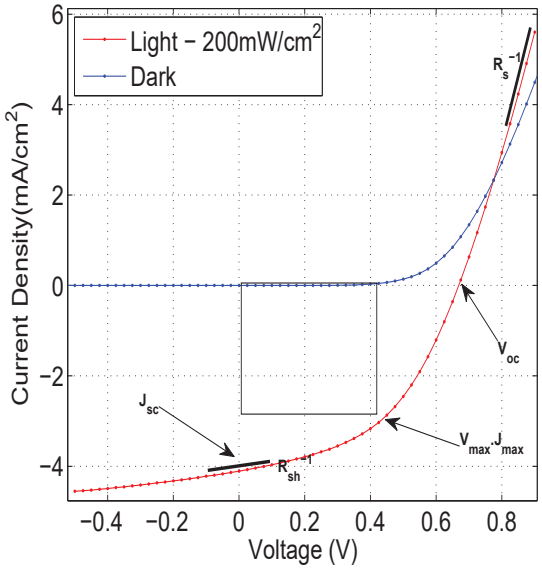

Figure 2.7: Current-voltage characteristics of a P3HT:PCBM-based BHJ device tested under dark and light of intensity of $200mW/cm^2$.

Light soaking effects and stability issues

For organic semiconductors to find a niche in the photovoltaics market, it is quite important that they have longer life and a stable performance. It has already been documented that exposure of devices to light, especially in the presence of extrinsic agents like oxygen, moisture etc., can drastically affect the device performance [67]. The optical treatment not only affects the chemical structure of the active medium, but can also modify the contact-semiconductor interface like the interface states, barrier heights etc. For example, in the current-voltage characteristics of bulk-heterojunction

solar cells, the light-soaking is known to cure the S-shape [68, 69], as shown in the Figure 2.8. Clearly the S-shape is detrimental to photovoltaics by reducing the fill-factor and hence the efficiency. The possible causes for the s-shape is argued to be either from the difference in the electron and hole mobilities [70] or due to inefficient charge extraction at one of the contacts [71]. Likewise, Light soaking is also shown to reduce the charges extracted in the CELIV experiment [72] emphasizing the modifications to the interface energetics.

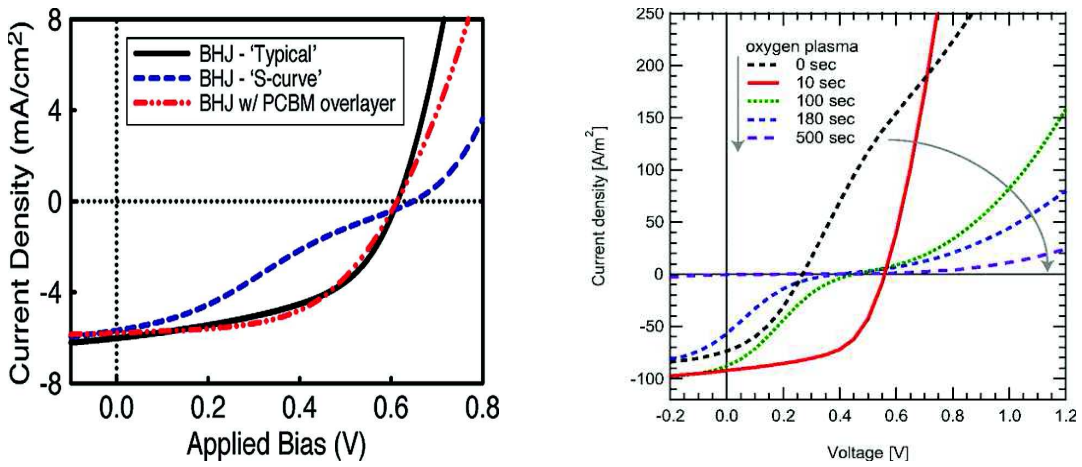

(a) (b)

Figure 2.8: The S-shape in current-voltage characteristics, that is usually observed in organic photovoltaics, is cured by modifying the cathode contact interface by using a) additional layer of material[71], or b) Ozone-plasma treatment of ITO substrates before depositing active layer,[68].

Recombination types and losses

Recombination of polarons is one of the mechanisms responsible for reducing the short-circuit current (J_{sc}) and the fill-factor (FF), thereby reducing the cell efficiency. Recombinations can be radiative or non-radiative in kind. The recombination

losses can be characterized under geminate and non-geminate recombination processes. Geminate recombination is the recombination of the polarons that split at the interface but fail to fully dissociate and are held back by weak coulomb attraction. Non-geminate recombinations, like trap/surface assited recombinations or bimolecular recombination, are the recombinations of the dissociated carriers occur through independent events. The bimolecular recombination may either follow Langevins or Shockley-Read-Halls mechanism [73]. Langevins recombination happens when there is a finite probability of finding the oppositely charged carriers from an uncorrelated event. Shockley-Read-Hall recombination, on the other hand, occurs via levels in the forbidden energy gap, introduced by impurities and lattice defects. It is basically a trap-assisted recombination. Geminate recombinations are prominent when operating under short-circuit condition, but away from the short-circuit condition and toward the open-circuit condition, both geminate and non-geminate losses affect the I-V characteristics significantly [74, 75]. It is understandable that under flat-band conditions, when the built-in field is annulled , the probability of finding the opposite charge centers is quite high thereby increasing the non-geminate recombination losses. Recent reports show that, under the flat-band conditions, the dissociation efficiency of the photogenerated charges carriers and hence the geminate recombination may be affected too. Earlier studies on the time scales over which different mechanisms occur in OPVs are compiled here:

- The ultrafast charge transfer at acceptor:donor interface occurs usually between (100-250)fs [76].
- Interchain energy transfer between polymer chains occurs over few 100s of picoseconds, explained by forster-type hopping process [76, 77]

- Geminate recombinations can occur upto few tens of nanoseconds (few nanoseconds in polyfluorene copolymer/PCBM blend systems).

- Radiative recombinative lifetimes of about 660ps was observed using time-resolved photoluminescence studies. It was shown by probing the sample using both TAS and PL techniques [78]. In the former case, the lifetime of decay was 660ps that included losses due to all radiatively and non-radiatively recombining excitons, where as only 200ps from the latter study is just due to the radiative excitons, emphasizing the non-radiative routes of energy transfers.

- Charge transportation towards the electrode can take about few microseconds to milliseconds [79].

2.2.3 Charge Extraction by Linearly Increasing Voltage(CELIV):

CELIV technique was intially designed by Juska et al. [80] to study the charge carrier mobility and concentration in microcrystalline silicon ($\mu c - Si\colon H$). The technique was deviced especially to the study very thin films of submicron thicknesses and those that have relatively high conductivity.

Replacing Time of Flight(ToF) - For thin film devices, the photogeneration of charges is across the full volume of the device, and hence the identification of the kink indicating the transit time of the charges reaching the opposite electrode is complicated which is already affected by the dispersive charge transport in amorphous materials. Another important requirement for the ToF tests is that the photogenerated charges experience a constant electric field in presence of the external bias. In a case where the semiconductor is doped(say, $\sim 10^{16} cm^{-3}$), the formation of depletion

layer at the interface of metal-semiconductor interfaces can alter the electric field distribution making it non-uniformly distributed across the device thickness with most of the external supply voltage droping at the depleted interface, while little across rest of the device. The higher the doping induced free thermal carriers, the shorter the dielectric relaxation time($\tau_\sigma = \frac{\epsilon\epsilon_0}{en_0\mu}$). If the device is operated under low-field conditions leading to a long transit time($t_{tr} = \frac{d^2}{\mu V}$) such that $t_{tr} >> \tau_\sigma$, it is possible that the photogenerated signal is already lost before reaching the respective electrode. In addition to that optical excitation creates both kinds of charges. For bulk generated charges, the resultant mobility is biased towards the slower charge-type. In dark-CELIV, only kind of charges are injected until they are in equilibrium before extracting them. As the charge-scooping ramp starts immediately, the materials with relatively higher conductivity i.e. shorter relaxation time, τ_{sigma}, can be studied with dark-CELIV, which otherwise is a limitation for ToF. Dark-CELIV also has a limitation that the initial injection voltage is limited to the voltage setpoint where SCLC dominates. At and above this setpoint, the conductivity of the device for the specific charges is way to high and hence τ_{sigma} is very short, that fraction of additional injected charges are already lost under thermal equilibrium.

In order to perform CELIV, it is necessary that there is one injecting/ohmic contact and one blocking contact, so that only charges filled in the devices are extracted and there is no additional injection of the charges from the opposite electrode during the charge extraction process.

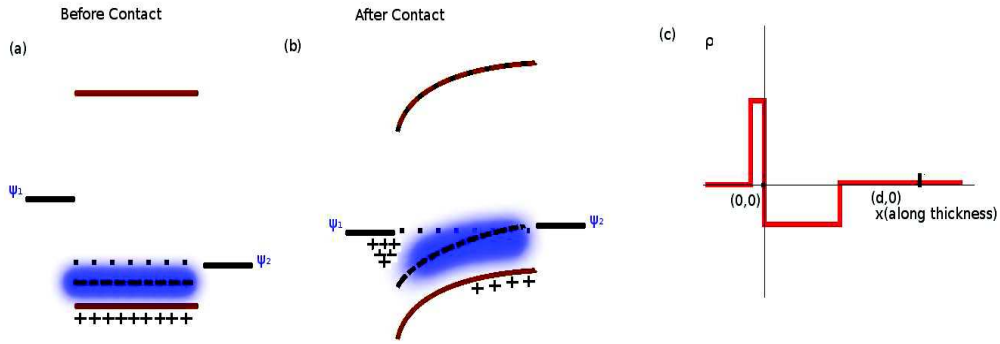

Figure 2.9: Energy level alignment a) before and b) after contact, c) Charge density redistributed after contact. The dotted line represents the fermi-level of the polymer, ψ_i represents work functions of cathode (i=1) and anode (i=2), the dashed line in blue band represent the negative acceptor ion shallow traps, + sign are the mobile holes in the polymer.

CELIV - Analytical framework

According to Gauss' law,

$$\frac{dE(x,t)}{dx} = -\frac{eN_A^-}{\epsilon} \qquad 0 \leq x < l(t) \tag{2.9a}$$

$$= 0 \qquad l(t) \leq x < d \tag{2.9b}$$

where l(t) is the space depleted of mobile or trapped charges, d is the device thickness, ϵ is the dielectric permittivity of the active medium and N_A^- the acceptor acceptor entity density. The negative superscript indicates the acceptor molecule is ionized negatively by accepting electron. Figure 2.9(a) and (b) show the energy level alignments between a cathode (ψ_1), ptype semiconducting polymer and anode (ψ_2) before and after contact. The blue band with the dashed line (representing negative charge

held by the shallow traps) close to the HOMO of the polymer represents the acceptor dopants level and dotted line is the Fermi level of the polymer. The charge redistribution within the device is approximated with abrupt step-like charge density as shown in Figure 2.9(c).

Integrating Equation (2.9a) within the limits leads to,

$$E(x,t) = \frac{-eN_A^- x}{\epsilon} + E(0,t) \qquad 0 \leq x < l(t) \tag{2.10a}$$

$$= E(d,t) \qquad l(t) \leq x < d \tag{2.10b}$$

with the boundary conditions E = E(0,t) at x = 0(Cathode contact) and E(d,t) at x = d(Anode contact).

Integrating the Poisson's equation over the full length of the device,

$$E(d,t) - E(0,t) = \frac{-eN_A^- l(t)}{\epsilon} \tag{2.11a}$$

Voltage drop across the device in terms of electric field is,

$$V(t) = \int_0^d E(x,t)dx \tag{2.12a}$$

$$= \frac{-eN_A^- l^2(t)}{2\epsilon} - [E(d,t) - E(0,t)]l(t) + E(d,t)d \tag{2.12b}$$

$$= \frac{eN_A^- l^2(t)}{2\epsilon} + E(d,t)d \tag{2.12c}$$

In CELIV, $V(t) = Rt - (V_{offset} - V_{bi})$, where R is rate of change of voltage called ramprate, t denotes time, V_{bi} is the built-in voltage and V_{offset} is the initial steady-state offset voltage set before(after) the onset(termination) of ramp pulse.

Equation of continuity, assuming no creation or destruction of charges, states

$$\overrightarrow{\nabla}.\overrightarrow{J} + \frac{\partial \rho}{\partial t} = 0 \tag{2.13a}$$

Integrating the Equation (2.13a) through x, knowing that the current is from the undepleted region (d-l(t)), gives

$$J = e\mu_p pE(d,t) = ep\frac{\mathrm{d}l(t)}{\mathrm{d}t} \tag{2.13b}$$

$$\Rightarrow E(d,t) = \frac{1}{\mu_p}\frac{\mathrm{d}l(t)}{\mathrm{d}t} \tag{2.13c}$$

From the Equations (2.12c) and (2.13c), the time evolution of the the depletion region in device is given by,

$$\frac{\mathrm{d}l(t)}{\mathrm{d}t} + \frac{ep\mu_p}{2\epsilon d}l^2(t) = \frac{\mu V(t)}{d} \tag{2.14a}$$

Current density due to mobile holes is given by,

$$J_h(x,t) = ep\mu_p E(x,t) + \epsilon\frac{\mathrm{d}E(x,t)}{\mathrm{d}t} \tag{2.15a}$$

where the first term on the right hand side is contribution from field-dependent drift current and second term is the displament current due to time-varying electric field inside the device. By averaging out the internal current over the length of the device

leads to,

$$J(t) = \frac{1}{d}\int_{l(t)}^{d} ep\mu_p E(x,t)\mathrm{d}x + \frac{\epsilon R}{d} \tag{2.15b}$$

$$= \frac{ep\mu_p}{d}E(d,t)[d - l(t)] + \frac{\epsilon R}{d} \tag{2.15c}$$

Only the free hole carriers in the region $l(t) < x < d$ participate in the net current. From Equation (2.13c) & (2.15c), the current transient is given by,

$$J(t) = \frac{\sigma}{\mu_p}[\frac{\mu_p V(t)}{d} - \frac{\sigma l^2(t)}{2\epsilon d}][1 - \frac{l(t)}{d}] + \frac{\epsilon R}{d} \qquad \text{for } t < t_{tr} \tag{2.15d}$$

$$= \frac{\epsilon R}{d} \qquad \text{for } t > t_{tr} \tag{2.15e}$$

where t_{tr} is the transit time of the slowest group of charges.

Voltage-step excitation:Dark-injection Transient Current(DiTC)

From the application of ramp pulse in CELIV, the voltage resets from the peak in reverse bias to the offset voltage applied before the onset of ramp pulse. The offset voltage could be in the contact-limited space-charge free(SCF) regime or be in space-charge limited current(SCLC) regime. Using CELIV, therefore it is not only possible to extract the information of charge stored, dielectric constant of the medium and charge mobility distribution from the 'ramppulse-front', but it is also helpful to visualize the current transients from the rear of the ramp pulse. Depending on time ranges that are being investigated, the current transients give information about the transit time of the injected charges which depends on the transport parameters which in turn depend on the defect structure of the specimen. It is also possible to study

the trapping/detrapping phenomenon before the free and trapped charges reach an equilibrium, which basically means one can watch the evolution of quasi-fermi level in the device.

The Space-charge-limited Transients

Figure 2.10 shows DiTC of the device where the voltage steps up from -1.8V to the offset voltage of 1.2V, which is in the SCLC regime. The device configuration used in this figure is ITO/ZnO/P3HT/MoO_3/Ag. Here MoO_3 forms the ohmic contact for hole injection, while ZnO serves as a hole blocking layer. From the J-V characteristics in a P3HT-based device, it can be understood that the SCLC regime begins at voltage higher than $\sim$ 650 mV for these devices. The initial fast rise in the signal is the displacement current($\partial E/\partial t - \infty$) due to the step signal input, followed by the RC relaxation transient as the step voltage approaches constant value and then with an overshoot(indicated by the arrow) before settling to the steady state current value. The physical explanation for the overshoot of the current is explained as follows. At the offset voltage, the current is mostly dominated by the diffusion component with the high hole concentration that are injected at the anode interface and holes that are extracted at the cathode interface. Under the influence of external voltage, there is also a drift component that assists the charge transport to the opposite electrode. However, as the charges approach to the opposite electrode, the depletion zone between the cathode and leading edge of the injected charges gets shorter with time. Therefore the electric field between the two edges rises with time. This in turn causes the charges to be drawn faster towards the cathode, leading to the current overshoot, shown in the Figure 2.10. The drift mobility of the holes can then be determined using, $\mu_{h,sclc} = 0.786L^2/t_{peak}V - bias$, where L is the device thickness,

t_{peak} is the current overshoot peak position, and V_{bias} is the applied voltage.

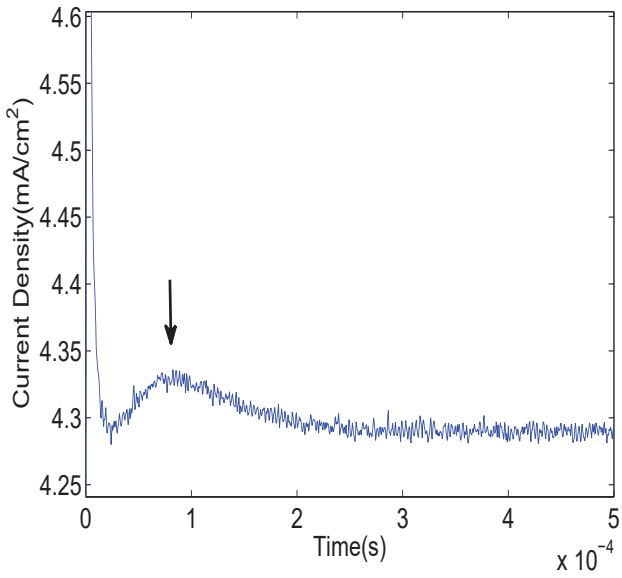

Figure 2.10: Dark-injection current transient of a P3HT-based device, for a step voltage of amplitude 3V from negative reverse bias towards forward biased offset voltage of +900mV, which puts the device under SCLC regime.

The Contact-limited current transients Unlike in SCLC regime, the charge injected into the device is very small compared to the net charge storage capacity of the device ($Q_{inj.} < \epsilon A/L$) at a given voltage. This could mean that charge injection was contact-limited or that external optical pulse used for excitation is very weak. This implies that the field inside the device can be considered almost constant across the device ($E = V_{bias}/L$). Solving the drift-diffusuion equations (ignoring diffusion for simplicity), the current density is given by,

$$j(t) = \mu Q V/L^2 \tag{2.16}$$

$$\text{Space-charge-free transit time is given by,} t_{tr} = L^2/\mu V \tag{2.17}$$

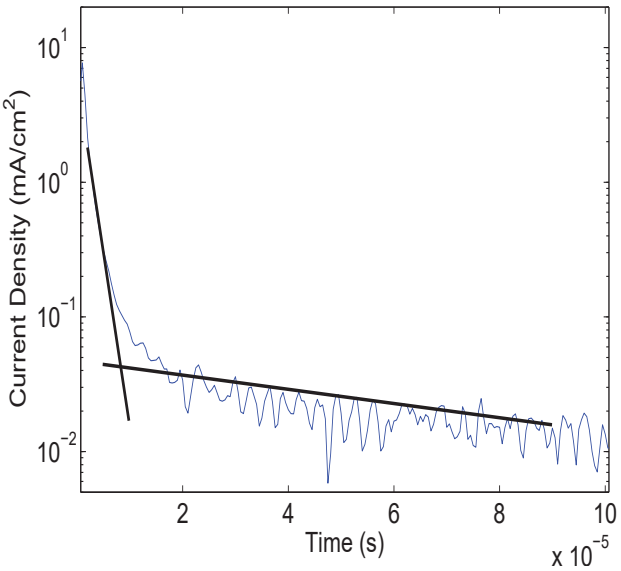

Figure 2.11: Contact-limited dark current transients tested on the same P3HT-based device.

where Q is the charge injected at t = 0. The injected charges undergo trapping/detrapping and dielectric relaxation loses before attaining steady-state current. Figure (2.11) shows the current transients after a step pulse drops from -3V to the final bias set at 100mV. The current decay indicates two slopes. The fast component is associated with dielectric relaxation process, while the slow one is associated with charge trapping and detrapping phenomenon.

2.2.4 Photovoltage

The actual operating point of a photovoltaic device depends on the external load attached to the PV cell, which is reminisced by the fourth quadrant (the lower right quadrant in figure 2.7) of the light-IV characteristics. By flipping the sign of the applied voltage, the V_{ext} is same as built-in voltage (V_{bi}). The built-in voltage in the

device is what leads to a measurable short-circuit photocurrent. It is important to know the built-in voltage, (V_{bi}), precisely in order to be able to measure the charge mobility accurately from the dark IV characteristics as well. One can find V_{bi} by either electroabsorption spectroscopy [81], or by measuring the open-circuit voltage, (V_{oc}), [82] by saturating the device optically or from capacitance-voltage measurements [41, 83]. The photovoltaic measurement is a simpler method to estimate the built-in voltage though. The bias applied in order to nullify the photocurrent or measuring photovoltage of the PV cell under saturation conditions is, an underestimate but, a measure close to built-in voltage. The open-circuit voltage depends on temperature, excitation light intensity, electrode work functions, morphology, density of states of the active medium itself. Brabec et al. [84] showed experimentally that V_{oc} scales proportionally to the difference in potential corresponding to HOMO of the donor and LUMO of the acceptor material, where the LUMO of the acceptor material was tuned by choosing appropriate acceptor molecules (Fullerene derivatives). In the same work, it was shown that the V_{oc} was independent of the cathode work function which was tuned from Calcium ($\phi_{Ca} \sim 2.87eV$) to Gold ($\phi_{Au} \sim 5.1eV$). The change in V_{oc} was seen to be mere $\sim 200mV$, while change in the cathode work function was over 2 eV. This is explained on the possibility of band-bending of the semiconductor at the surface due to metal-semiconductor bonding-induced surface states. The metal contact's work function would then be pinned to surface work function of semiconductor irrespective of what metal is chosen. Mihailetchi et al.[85] showed that V_{oc} for a device with ohmic contacts on both sides is decided by the HOMO of the donor and LUMO of the acceptor (with some loss in field due to the band bending inevitable at the ohmic contacts), whereas for a device with non-ohmic contacts it is simply the

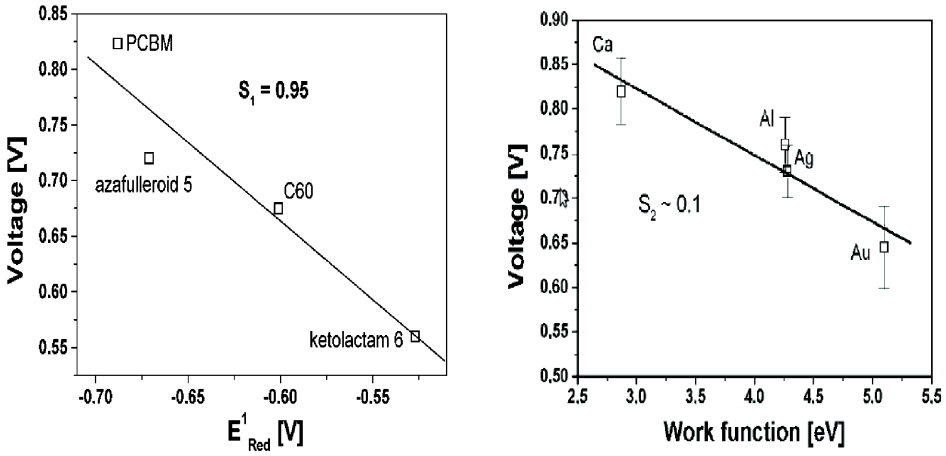

(a) (b)

Figure 2.12: a) Open-circuit voltage versus reduction potential (or LUMO) of the acceptor molecules, b) Dependence of open-circuit voltage on the cathode work function. Reprinted with permission from [84].

difference in contacts' work functions.

Blakesley's[86] theoretical work on V_{oc} dependence on the effective bandgap of the active media while considering disorder and recombination induced losses. Experimental work was attempted by Garcia et al.[87] tried to show the effect of disorder on the open-circuit voltage. In their work, two different kinds of acceptor molecules (Phenyl-C61-butyric acid methyl ester (PCBM) and DPM_6, both being fullerene derivatives) were used to dope the donor material(P3HT) separately, in order to measure the disordered DoS while keeping the LUMO of the acceptor same in both the cases. Blakesley's and Garcia's work point to the common understanding that higher the disorder, the smaller is the V_{oc}. Likewise, V_{oc} is shown to decrease with the increase in temperature.

Depending on the Fermi level (i.e. on the doping concentration) of the semiconductor and on the work-function of the metals/oxide-based contacts chosen, there can

be 'band-bending' that needs to be taken into consideration so that the fermi-levels of the two media align at the interface[88]. According to Mott-schottky model, it was assumed that post-contact of a metal and semiconductor, the vacuum level is common at the interface. However, it is now understood that the the vacuum levels may or may not align at the interface and there could be a possible vacuum level 'shift'. It must however be borne in mind that there is no Vacuum level at the interface, but it is concept adapted to conveniently describe the interface energetics. The Vacuum level shift at the interface is explained as due to interfacial dipole formation as a result of chemical bonding between metal and semiconductor. The fermi-level pinning is a direct consequence of these interface chemical-bonding states. UPS and Kelvin Probe Microscopy (KPM) [89] are commonly used to measure the energy levels. The vacuum level shifts are studied by measuring the bare metal contact first, followed by layer-by-layer deposition of the organic material. Theoretical understanding of these interface states can be found in Tung's recent works and review [90] and Braun et al.[91] for experimental investigations.

Zinc Oxide- adsorption and photodesorption of Oxygen- Tuning the Fermi level:

The ultimate goal for a high-efficiency device is to improve the built-in voltage, in other words, obtain a high photovoltage. Especially in the case of inverted photovoltaic devices it is preferred that the work function of the bottom cathode contact be low [92]. In lieu of this, Metal Oxides (MOs) that are used as interface buffer layers offer tunability of their work functions to play with. MOs are known for their high energy band gap, available with wide range of EAs and IPs. Their efficient orbital hybridizations in an amorphous state, allows the charges in the medium very high mobilities [93]. This unique combination of large optical band-gaps and high charge

mobilities renders their use as tranparent (semi)conductors. With a proper choice of materials, one can use them as buffer layers that can support transport of one type of charge carrier, while blocking the other kind [94].

ZnO has an unintensional n-type semiconductor characteristics, the origin of which is debated to be either from impurities like Hyderogen[95], or possibly be from native defects Oxygen vacancies and cation interstitials[96]. Thin layers of ZnO or TiO_2 overlaid on ITO surface are used to reduce the work function of ITO [97]. In the presence of contaminants (like Oxygen, moisture) the real work function of these metal oxides is pushed away from the conduction band, leading to larger work function. Under UV light exposure, the oxygen molecules that are physisorbed/trapped in the grain boundaries of the nanostructures of these MO can be released- the phenomenon termed as photodesorption [98]. The work function of the MO therefore resumes to the trap-free case. It has been one of the key components in my studies in understanding the overall device behaviour. As you will notice in Chapter 3, multiple tests prompted towards possible modification of the interface at the cathode (ITO/ZnO and Polymer) which makes it very important to understand the energetics of these MO layers.

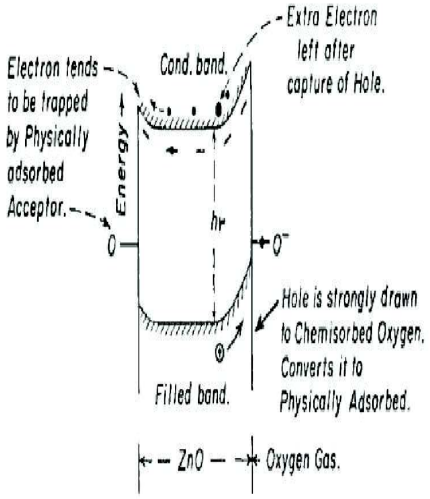

Figure 2.13: Photophysics of conduction in ZnO in the presence of O_2 defects on the surface.[99]

2.2.5 Other Experiments

Transient photovoltage (TPV)/ Photocurrent (TPC):

The experimental technique as mentioned in [100] is used to measure the lifetime of charge carriers in the device. The device is optically-saturated by soaking the device in high intensities of white light while measuring the photovoltage. As the external impedance is very high ($\sim 1M\Omega$), the photogenerated charge carriers have nowhere to go, but dissipate by recombination and/or by leaking slowly through the external resistance. During this soak period, the device is excited with a weak short optical pulse ($\sim< 1ns$) and the transients of the pulsed photovoltage is recorded. The article proposes that by measuring the decay time constant, one can deduce the lifetime of charge carriers in the device. The experimental setup of TPC[100] is similar to TPV, except that the device is operated under short-circuit conditions. The photocurrent

is measured by measuring the voltage across a very small resistance (close to short-circuit conditions). The area under the transient is integrated to measure the total number of photogenerated charge carriers.

Transient Absorption Spectroscopy (TAS)/Time-resolved Fluorescence (TRF)

Transient Absorption Spectroscopy (TAS) [101] is one of the non-circuit (no electrodes needed) experimental techniques used to probe the excited state kinetics of the photoactive samples. This especially is a handy techique when there is little to no luminescence efficiency, or in other words, probes all decay routes including radiative and non-radiative 'dark' channels. It is based on a pump-probe method, where the sample is excited by an optical pulse whose wavelength is chosen to be with the absorption spectrum of the sample, followed by a pump pulse (pulse width is subject to how fast dynamics are to be resolved)at variable time delays. The change in the probe absorbance spectrum is plotted for various delays between pump and probe. In simple cases when there is an apriori knowledge of slow decay dynamics (assuming slower than the fast photodiodes), the probe can be a continuous wave light. With the fast photodiodes in availability, there is no need of varying time delays between pump and probe. And where the absorption spectra of the excited state is known apriori, the decay dynamics of a narrow band probe absorbance needs to be tracked using a fast photodiode. Soon Y. W. et al. [102] used this technique to correlate the polymer triplet state quantum yield and the singlet oxygen generation. TRF is a useful technique when radiative recombination is the dominant decay channel. Like TRA, TRF gives valuable information about the excited state relaxation processes.[103]

Thermally Stimulated Current (TSC):

Thermally Stimulated Current (TCS) [104, 44] is used to measure trap levels and their concentrations. The trap states in the device are filled either by applying a bias or by soaking in light, while simultaneously reducing the temperature in order to freeze the trapped charges. External bias or illumination is now cut-off, leaving the device off thermal equilibrium. From this point, as the temperature of the device is slowly increased, the trapped charges are released and the current reaches a maximum before dropping to zero(almost). Thereby giving an estimate of the energetic location of the trap states. The current maximum position and amplitude depends on the rate of temperature sweep as well.

Chapter 3

Experimental Setup

3.1 Introduction

This chapter focuses exclusively on the device preparation procedure and the experimental techniques employed to characterize them. Many cycles of tests had been conducted on some of the samples over long periods of time intermittently. When not under study, the devices were stored either in the dark place for the tests that were performed over short periods of time or in the dark and dry-glovebox ($O_2 < 10ppm, H_2O < 5ppm$) for long periods of storage. Prolonged optical and electrical tests were possible especially on the devices that were encapsulated without any significant degradation.

3.2 Sample Preparation

All the devices made and tested were two-terminaled and 'sandwich-type' in layer stacking. Figure 3.1(a) on the next page shows the device configuration implemented for the studies. The bottom-most material is a transparent glass substrate, followed by a transparent conducting material Indium Tin Oxide (ITO). On top of that are a

hole-blocking layer of ZnO, active medium based on P3HT, MDMO:PPV, PCDTBT, P3HT:PCBM, finishing with a layer of MoO_3 and silver. This configuration is referred to as 'inverted-type' for the reason that the cathode is a stable low-workfunction contact made out of ITO/ZnO, while silver is the top anode contact with relatively higher work function. While the ZnO layer also serves as a hole-blocking layer in the reverse bias, the Molybdenum oxide (MoO_3) layer serves as ohmic contact between silver and the active layer for hole injection, due to its very deep lying conduction band edge.

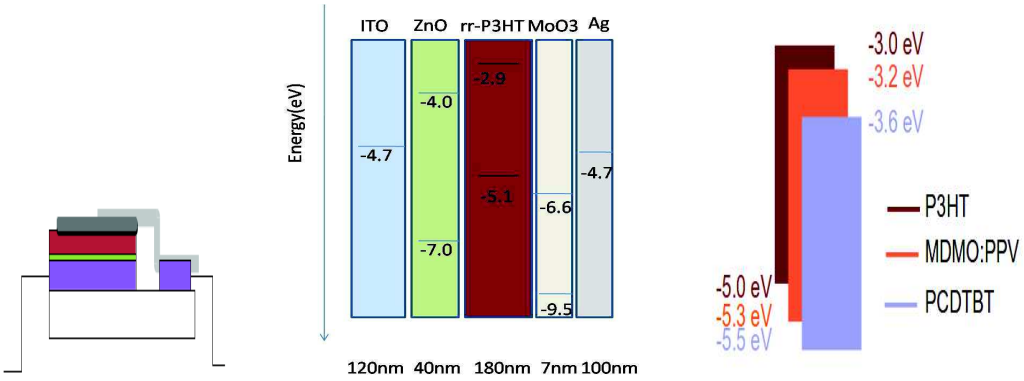

(a) (b) Energy levels of the layers before bringing them in contact (c) LUMO and HOMO energy levels of the polymers

Figure 3.1: a) Device' layer configuration, Band-edge energy levels of a) each layer of the device and c) polymer used.

Contacts:

Zinc Oxide/ITO - Transparent bottom contact (cathode)

0.75 M of Zinc acetate dihydrate $Zn(CH_3COO)_2 \cdot 2H_2O$ in 2-methoxyethanol $(CH3)_2CHOH$ along with monoethanolamine $(OHCH_2CH_2NH_2)$ that acts as a stabiliser [105]. The solution was stirred outside glovebox for 24 hours before spin-coating on a freshly oxygen-plasma treated ITO coated glass substrates, in the open

air conditions at room temperature (20℃). The spin-coating speed of 3000 rpm for 40 s was chosen to obtain a film thickness of about $40nm \pm 5nm$.

Molybdenum Oxide/Ag - Top contact (Anode) Silver is the top contact serving as anode, while Molybdenum oxide facilitates a proper ohmic contact for all the polymers mentioned above, with silver.

Active Media:

Poly (3-hexylthiophene-2,5-diyl),P3HT

P3HT of regioregularity (90-94)% and molecular weight of (50-70)kDa was used as received from Reike's metals. The solution of P3HT and dichlorobenzene was dissolved by stirring under dark conditions for 48 hours inside the glovebox. All the tests carried out in Chapter 4 are with P3HT/dichlorobenzene concentration of 20 mg/mL.

Poly[2-methoxy-5-(3,7-dimethyloctyloxy)-1,4-phenylenevinylene]

MDMO:PPV MDMO:PPV with molecular weight $\sim 50kDa$ was used as received from Organic Nano electronic 1m. The polymer was stirred in dichlorobenzene for about 48 hours under dark conditions inside the glovebox. A concentration of 7 mg/mL of the solution was used to prepare all the MDMO:PPV based devices described in Chapter 5.

Poly[N-9'-heptadecanyl-2,7-carbozole -alt-5,5-(4',7'-di-2-thienyl-2',1',3'-benzothiodiazole)]

PCDTBT: PCDTBT with molecular weight (20-40)kDa was used as received from Solariz. The polymer was stirred in dichlorobenzene for about 48 hours under dark

conditions inside the glovebox. A concentration of 7 mg/mL of the solution was used to prepare and test all the devices mentioned about in Chapter 5.

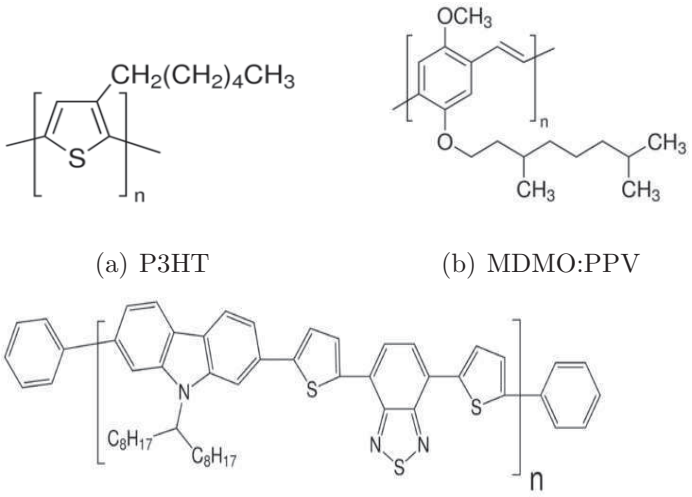

(a) P3HT (b) MDMO:PPV

(c) PCDTBT

Figure 3.2: Chemical Structures of the polymers. Image courtesy: Sigma-Aldrich, www.sigmaaldrich.com

Device preparation: The glass substrates with etched ITO were cleaned by sonicating the slides in iso-proponol, soap water, distilled water and acetone for 5 minutes sequentially. The air-dried slides were then cleaned further for surface contaminants using oxygen plasma for 5 minutes. A layer of ZnO, prepared as mentioned above, was spin-coated on top of the ITO side of the substrate in open air at an angular velocity of 3000 rpm for 40 s and annealed at 180 ℃for 15 minutes. The open air preparation, spin-coating and annealing is necessary to prepare n-type doped ZnO layer. The active layers were spin-coated at 600 rpm for 60 sec inside the glovebox. The spin-coated substrates were immediately transferred on to a hot plate at 120℃to thermally anneal the active layers for 10 mins. The as-prepared substrates are then

Layer	Thickness (nm)	Preparation Method	Specifications
ITO	120		
ZnO	40 ± 5	Spin-coating	3000 rpm for 40 s, $T_{annealing} \sim 280$℃
P3HT	180 ± 20	Spin-coating	rr - (90-94)% M_w -(50kDa-70kDa) Mfr: Reike Metals
MDMO:PPV	190 ± 20	Spin-coating	$M_w \sim 50kDa$, PDI 2.2 Mfr:1-m Materials
PCDTBT	70 ± 10	Spin-coating	M_w=(20kDa-40kDa) Mfr: Solariz
MoO3	7.0 ± 0.5	Thermal Evaporation	Deposition rate 0.5A/s
Ag	100	Thermal Evaporation	Deposition rate 0.5A/s

Table 3.1: Device's layer-deposition methods and settings.

transferred within the glovebox into the physical vapour deposition chamber. The MoO_3 followed by Ag layer were thermally vapour-deposited at a vacuum pressure of 1E-6 mBar. The table below summarizes all the relavant information of each layer.

Encapsulation: The encapsulation of the devices were done using super glue 15350 single use epoxy 5 minutes set. An equal proportion of the resin and hardner of the super glue was made just few seconds before the encapsulation procedure. A miniscule drop of the mixture, just enough to cover the top electrode ($\sim 0.07cm^2$, in our case), was placed on top of the metal electrode, followed by gently pressing the glass cover against the device. The encapsulation is let to set under ambient pressure for few hours. The whole procedure of encapsulation is performed within the glovebox. The current voltage characteristics were compared for the cases before and after (1 hour) encapsulation and no noticeable differences were seen.

Figure 3.3: Two off the four devices encapsulated using glass and epoxy super glue.

3.3 Experimental techniques and their set-ups

Current-Voltage Characteristics: The steady state current-voltage measurements were performed using either Keithley 4200 SCS or Keithley 2400 SMUs. Although for the observational purposes, the scans were performed by sweeping in both forward and reverse directions, all the I-V characteristics presented here are those for forward sweep i.e. by applying negative bias to the anode (Ag) and swept towards positive bias with respect to the cathode (ITO). The hold time for after each step of increment in bias is set to be 500 ms. The halogen and Mercury arc lamps attached to the optical microscope were used to perform light-IV characteristics and light-soaking tests. The optical spectra of the two lamps are shown in the Appendix D.

Variation of device open-circuit voltage, V_{oc}, with light soak:
The devices were soaked under halogen lamp at an intensity of about $60 mW/cm^2$ to record the V_{oc} variation with the soak time. The V_{oc} was meaured across the device with the oscilloscope's (Keysight infiniivision, DSO 2000 series) input resistance set at $100 M\Omega$. The excitation intensity fluctuations, although negligibly small, were monitered using another Silicon photodiode. The data is acquired at fixed intervals using Labview.

Charge Extraction by Linearly Increasing Voltage (CELIV): CELIV was used

to extract the charges stored in the device at different injection levels. Figure 3.4(a) shows the circuit used to perform CELIV and the Figure 3.4(b) shows a typical input voltage and current dynamics through the circuit. The ramp signal of constant slope and fixed ramp period is applied to circuit with the device under test (DUT) in series with a 50Ω sensing resistor at a fixed repetition rate.

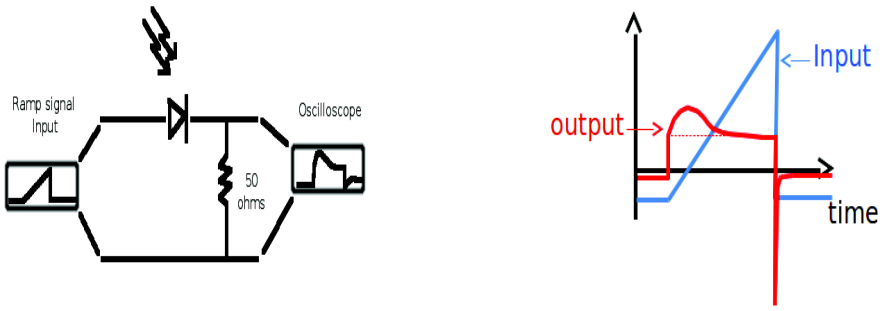

(a) (b)

Figure 3.4: a) Circuit diagram for CELIV, b) Typical input ramp voltage and corresponding output signal in CELIV experiment.

The intial offset/injection level is varied in steps from reverse bias to forward bias. The key idea of this experiment is to fill up the trap states with charges injected at different levels at a steady state, before being extracted by the linearly increasing ramp signal towards the reverse bias. The charges extracted are quantified by integrating the current above the displacement current over the ramp period.

Dark injection current transients (DiTC): The pulse's rear edge of CELIV where the ramp drops from the peak to the different initial offsets has been studied for DiTC. The ramp signal is designed using function/arbitrary waveform generator, Agilent 33220A 20 MHz, while the output signal is monitored and acquired using Keysight's Infiniivision DSO-X 2000 series (GBW 200 MHz). The waveform generator was externally triggered due to the limited DAC depth bits, which otherwise

would generate discrete steps of the ramp voltage when operated under low pulse repetition rate.

Luminescence Studies: For the steady-state and time-resolved luminescence studies, the tests were carried out using Time-Correlated Single Photon Counting (TCSPC) technique. For photoluminescence transient studies, the sample under study was excited with a polarized optical pulses of width $\sim$ 45ps at a wavelength of $(405 \pm 5)nm$ or $(465 \pm 5)nm$ coupled into the optical microscope (Carl Zeiss). The filter set with excitation clean-up filter at the chosen wavelength, a dichroic mirror with a cut-on wavelength at $(488 \pm 10nm)$ and an approriate emission filter was chosen, depending upon the sample under test. The photoluminescence detection was carried out under epifluorescence mode, where the objective that is used to excite the sample is also the one to collect the emitted photons. The very low-light signal, a prerequisite for the TCSPC technique, was directed towards the Avalanche Photodiodes (APDs) (MPD, micro photon devices). The excitation intensity was chosen so that the ratio of rate of emission to the excitation pulse repetition rate is less than 0.01 with the help of a counter (Philips PM 6671 high resolution time/counter 120 MHz). This ensures that there is either one photon or no photon detected per optical excitation in order to avoid the 'pile-up' distortion. The NIM negative signal from the detector was fed to the Ortec 436 100 MHz Constant-fraction discrimator (CFD), the output of which was then fed to the 'START' Time-to-Amplitude Converter input of the timing module (SensL technologies). The clock output of the SensL module, was used as 'STOP' input to the SensL itself as well as to trigger the laser excitation source for synchronization. The arrival time of the detected photons with respect to the excitation

pulse is then histogrammed over required length of time to record the luminescence decay dynamics. The same set up was used for the electroluminescence tests except that there is no filter set en route the luminescence emission detection. For low light steady-state electroluminescence studies the square pulse from the CFD, corresponding to the photon detected, was connected to NI-DAQ 6000 series card counter input. For EL and simultaneous I-V characteristics, the Keithley 2400 SMU and the DAQ were synchronized using Labview.

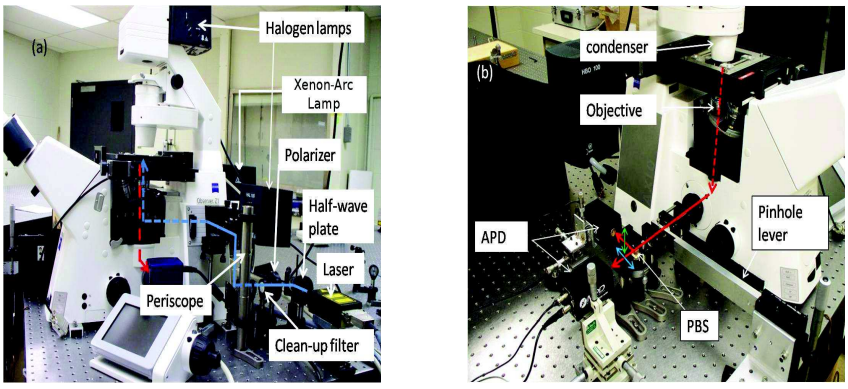

(a) (b)

Figure 3.5: a) Experimental set-up with optical microscope and external laser source coupled into it, b) Detection side of the set-up for very low intensity photons detection using APDs and other opto-mechanical elements for light collection and collimation.

For imaging purposes, the sample was excited using Mercury Arc lamp (HBO) in conjunction with the same filter set described as above and the luminescence was directed towards the CCD camera (AxioCam HRmTime) with controllable exposure times. For steady-state photo and electroluminescence spectra, the emission signal was steered towards the eyepiece of the microscope and captured using OceanOptics spectrometer. The flip mirror that comes with optical microscope is used to steer the signal either towards the camera and/ spectrometer or towards the APDs with a very

good precision.

Topography and profiling: Atomic Force Microscope(AFM), Ambios Technologies, was used to scan for nanometric surface topology in non-contact mode for roughness. For film thickness measurements, white light interferometer() and/or profilometer was used.

Laser Beam Induced Current (LBIC): The LBIC scans were performed using a diode laser at a wavelength 532nm as optical excitation, coupled into the inverted optical microscope with focussing objective of numerical aperture 0.75. The diode laser was electrically triggerred for optical pulse output of width $75\mu s$ and a repetition rate of 440 Hz. A TTL output from the triggering source was used as reference signal to the lock-in amplifier (LIA), while the photogenerated short-circuit current from the locally excited device area is connected to signal input of the LIA in a transimpedance mode. The average optical power at the focus of the objective was measured to be $(285 \pm 5)nW$, which for an excitation diameter of $(4.0 \pm 0.5)\mu m$ at the focus of the objective. The excitation power was monitored using a silicon photodiode, PD1 (S2281, Hamamatsu Photonics) by measuring 20% of the power reflected off of the quartz plate. The light reflected/scattered off the sample was collected by the same objective that is used for excitation, and focussed onto a second Silicon photodiode, PD2 (S2281-01, Hamamatsu Photonics). The sample was moved in steps of $5\mu m$ using Thorlabs' motorized stages . The motorized stage and data acquistion from the LIA signal output, excitation reference of PD1 and scattered/reflected light detected by PD2 is synchronized using Labview. The ActiveX controls of the stages were used to control the stage positions, while NI-DAQ6000 data acquisition card was used to acquire data from LIA, PD1 and PD2.

All the optical alignments, electrical connections, data acquisition flow and synchronization are summarized in figure 3.6 & 3.7. Figure 3.6 emphasizes on the ray optics part of the set-up that couples various light sources into the microscope and redirects the signal from the DUT to the associated sensors and/or amplifiers. Figure 3.7(b) shows a block diagram of electrical controls associated with LBIC, IV, TRF and CELIV characteristics. Figure 3.7(a) are the photocurrent amplification and rectification circuits for the PD1 and PD2 photodiodes indicated in figure 3.6.

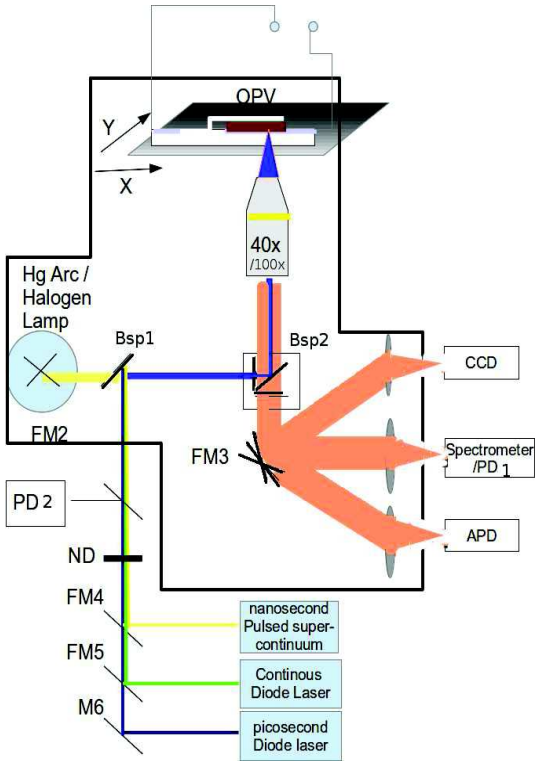

(a)

Figure 3.6: Optical alignment showing different optical sources/emitted signal coupled in and out of the optical microscope. Flip mounts FM4,FM5,FM6 help coupling various lasers; FM2 is used to switch between Halogen lamp and Mercury arc lamp; The Bsp1 is a 50:50 beamsplitter that couples the lasers into the microscope. Bsp2 forms a combination of filters containing selective excitation band, dichroic and emission band wavelengths of light for fluorescence studies or simple a 50:50 beamsplitter for bright-field imaging. FM3 redirects the signal of interest to one (or two) of the three exit ports of the OMS. PD1/2 are the photodiodes, APD is the avalanche photodiode and ND is the neutral density filter turret.

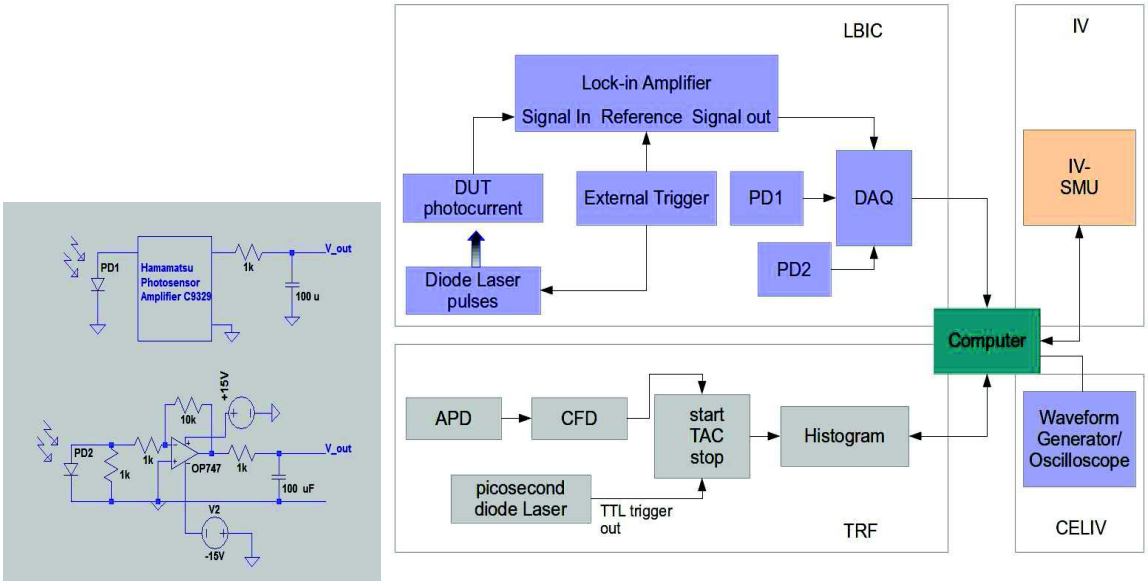

(a) (b)

Figure 3.7: a) Photocurrent amplification and rectification circuits, b) Block diagram of electrical signal flow chart and data acquisition of all the techniques employed.

Chapter 4

Charge Transport in P3HT-based Diodes

4.1 Introduction

This chapter focusses on characterizing the semiconducting polymer P3HT, in order to better understand the blend of the same polymer with other n-type acceptors like PCBM or compare it with other polymers to be discussed in the chapters to follow. The primary interest is to build an understanding of the charge dissociation(in case of photoexcitation) and transport of the charges in these conjugated polymers at a microscopic scale and relating them to the overall device behaviour at a macroscopic scale and in the case of blends. It is well known that over the period of study of any particular sample, the optical and electrical characteristics of the samples would change drastically owing to the ambient conditions [67, 106]. Especially, the presence of Oxygen/moisture in the ambience under UV exposure or thermal variations do act as dopants(shallow traps) or traps, affecting the conductivity of these organic materials [51]. The fact that these effects can be expedited in the presence of light leads to enhanced photodoping and photodegradation of the active medium [107]. Although there are many reports mentioning the effect of O_2 diffusion into these polymer based

devices, the nature of these traps especially their energy levels, dispersion in energy, physical location of traps i.e. whether at the interface or the bulk and process of encroachment into the cell etc., yet needs experimental attention.

In order to disentangle the effect of these scavenging entities from those of intrisic behaviour of the material, it was decided that the devices under encapsulation be used as control for reference. The intention was not just to keep the samples away from unexpected entities, but also to compare them with those that are eventually affected by them. On a glass substrate with four device cells, we chose to encapsulate two of them while leaving the other two unencapsulated. This is to ensure that the devices under comparison underwent almost similar treatment at different steps of fabrication.

The sections 4.2 & 4.3 contains the characterization on the P3HT-based devices that shows the effect of buffer/interface layers and the effect of depositing the active medium inside and outside the glovebox. During these studies it was noticed that the charge extraction and current-voltage characteristics changed noticably upon exposure to light over time. The section 4.4 is alloted to study the light-soaking effects on the charge storage and transport abilities of the devices by monitoring the change in current-voltage studies, CELIV, EL and PL (steady and transient).

The layers constituting P3HT based two terminal devices are shown in Figure 4.1 along with their energy levels LUMO and HOMO apriori contact. As all the tests done in this work were on two terminal devices, from this point onwards, any of the two terminal devices with various layers would be referred by the name of active medium used in the device. For example, the device shown in Figure 4.1, would be refered as P3HT-based device and likewise for brevity, unless otherwise mentioned.

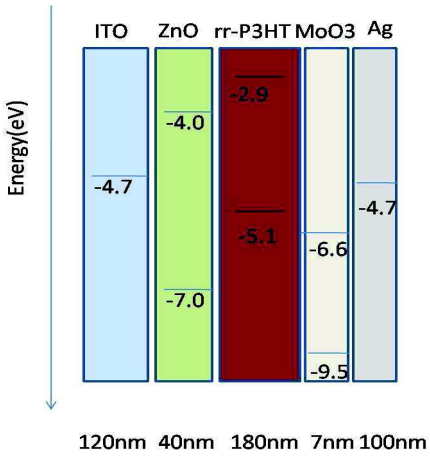

Figure 4.1: Schematic of layers constituiting a P3HT-based device with their energy levels corresponding to LUMO and HOMO before contact.

The work function of Ag in our samples is taken to be between (4.6-4.7)eV [92]. There were no tests conducted to measure the work function of Ag vapour-deposited on an organic polymer surface. Also the work function of ITO is taken to be 4.7eV [92], although it should be noted that the ITO on the glass substrates were oxygen-plasma treated prior to spin-coating ZnO layer. It is very well known that oxygen plasma or UV treatment affects the work function of ITO significantly [108, 109], or may even be manipulated by using other interface layers [92]. Similar is the case of MoO_3 whose pristine work function, $\sim 6.4eV$, can be modified using microwave exposure [110], oxygen/moisture [111] or annealing [112].

4.2 Effect of interface layers

4.2.1 Current-Voltage characteristics

Figure 4.2(a) shows the effect of ZnO and MoO_3 buffer layers on the current-voltage characteristics. This helped to identify the contribution of each layer towards the

built-in field. The presence of ZnO and MoO_3 leads to high open-circuit voltage, while removing ZnO greatly reduces the V_{oc}, and removing ZnO and MoO_3 significantly reduces the open-circuit voltage, as shown in the Table 4.1 tested over multiple devices. Clearly the ZnO layer introduces some interface barrier for hole extraction, and possible series resistance obvious from the reduced slope (dI/dV) at higher voltages. Other characteristics to note is the diode rectification ratio. The devices with ZnO and MoO_3 showed highest rectification ratio of the order of $10^4 - 10^5$ measured at +1V(Forward Bias (FB)) to -1V(Reverse Bias (RB)), indicating the very efficient hole-blocking characteristics of ZnO preventing the hole injection at the cathode in the reverse bias. Figure 4.2(b) shows the effect of presence(circled) and absence(lined) of ZnO layer, while no MoO_3 is included, highlighting the fact again that the ZnO layer provides higher rectification property.

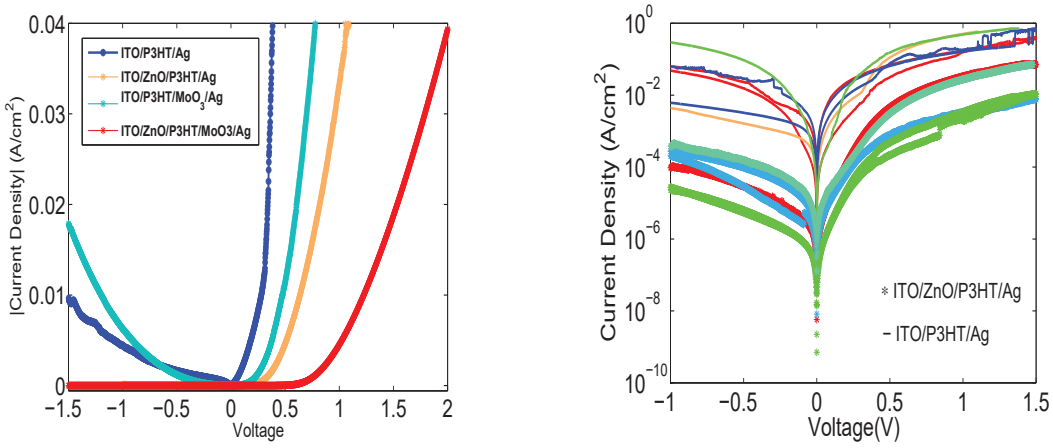

(a) (b)

Figure 4.2: a) |J|-V characteristics of P3HT-based devices in the dark with and without ZnO and/or MoO_3 layers, b) and log(|J|)-V characteristics of P3HT-based device with and without ZnO layer.

ZnO	P3HT	MoO_3	V_{oc}	Number of devices tested
✓	✓	✓	(250-530)mV	9
✓	✓	×	(280-325) mV	5
×	✓	✓	$\leq 3.5mV$	12
×	✓	×	$\leq 3.5mV$	8

Table 4.1: Effect of interface layers on the photovoltage from the P3HT-based devices.

It was noticed that in the absence of MoO3 i.e. with the direct contact of the silver electrodes with the P3HT and unencapsulated, the silver lost its lustre very quickly, even when stored in the nitrogen glovebox(humidity $\sim$ 20 ppm, $O_2 \sim 70$ ppm).

4.3 Effect of Encapsulation of devices

4.3.1 Effect of encapsulation on current-voltage characteristics

Figure 4.3(a) shows the the log(J)-log(V) characteristics of pristine and aged (accelerated by not encapsulating) devices, in order to highlight different regimes that are affected. The annotations in the plot denoted by PE, AE and AU represent pristine/encapsulated, aged/encapsulated and aged/unencapsulated devices respectively, and the numerics are to identify different regimes in each case. The aged devices were tested after 2 months of preparation.

The Ohmic regime: The ohmic regime is not so pronounced in the pristine devices as in the aged device, indicated by AU-1 and AE-1 linear regimes that have slope equal to one. The device that has aged showed a significant ohmic behaviour for as high as 200mV of forward bias, indicating the increased charge density in the device

at thermal equilibrium.

The SCLC regime: The SCLC regimes are indicated by PE-2,AE-2 and AU-2 where the slopes begin to approach values around 2. Clearly the SCLC conditions are attained for relatively lower forward bias in the case of aged and/or unencapsulated cases, again pointing towards the increased conductivity due to extrinsic doping.

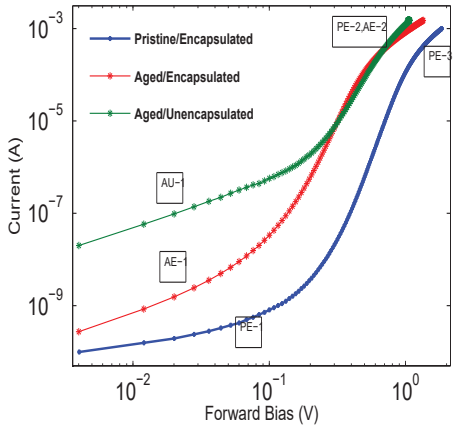

(a)

Figure 4.3: a) I-V characteristics of an encapsulated/unencapsulated and pristine/aged device tested in the dark.

The hole mobility measured in the SCLC regime PE-1 in Figure 4.3(a) is, following Mott-Gurney's square law, calculated to be (20 $\pm$6)x$10^{-4} cm^2/V-s$. The protocol followed to extract the charge mobilities from the SCLC is shown in Appendix B. The bias range chosen for SCLC fit in the above case is (0.8-2)V.

4.3.2 Effect of spin-coating P3HT inside and outside glovebox

Figure 4.4 shows the J-V characteristics of the devices where P3HT is spin-coated inside and outside the glovebox, without MoO_3 layer in either case. So the device

configuration was, ITO/ZnO/P3HT(Glovebox or Open air)/Ag. For the bias voltage less than 500 mV, the devices that were made inside the glovebox showed higher dark conductivity, as compared to the devices in which P3HT was spin-coated outside the glovebox. This is counterintuitive to the argument that the exposure of P3HT to oxygen leads to increased p-type doping that leads to increased conductivity. The difference in the characteristics is stark for low voltages i.e $\lesssim \pm 0.5$V, implying that the exposure to air is most likely affecting the interface barriers. The trap-filled Space-Charge Limited Current (SCLC) coincided for both the cases at about +1.5V rules out the possibility of degradation, atleast not within the testing time.

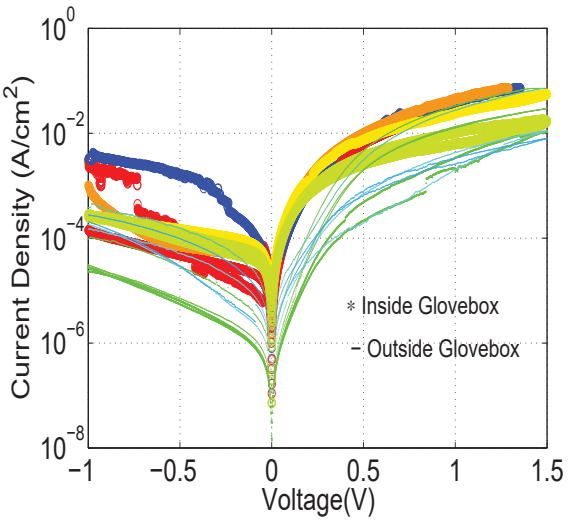

Figure 4.4: Dark J-V characteristics of P3HT-based devices in which P3HT layer is spin-coated inside and outside glovebox and without the MoO_3 layer.

4.3.3 Charge Extraction studies by Linearly Increasing Voltage

The experimental set up has already been described in Section 3.3 in detail. It can be witnessed from the previous experiments on how the ambience can affect the current-voltages characteristics of the devices drastically. In organic diodes, the overall charge

mobility of a given device depends upon the charge already present in the device and the internal field. CELIV technique is used to extract the charges stored in the device at various biases applied to the device. The ramp amplitude chosen to be 3V over $300\mu s$, while sweeping the initial constant DC bias from negative(RB) to forward(FB) direction. CELIV is used to assess the effects of aging and light-soaking on the devices, while simultaneously monitoring the current-voltage characteristics.

Charge extracted at various injection levels

Figure 4.5(a) and 4.5(b) shows the CELIV on freshly prepared P3HT-based device encapsulated and unencapsulated, respectively, by varying the offset voltage from -1V to +1V. The charges extracted is plotted against the offset voltage in Figure 4.5(d). Clearly, there is a fraction of an order of increase in the charge stored(extracted) in(out of) the device that was unencapsulated. Another important feature to be noticed in the case of encapsulated device is the error function characteristic of charges extractable from the device that reaches a saturation level indicating the absence(to a good degree) of any midgap defect states, while the device unencapsulated showed a monotonous increase in charges extracted seemingly superimposed on the error function. The built-in voltage is from the work-function of ITO/ZnO and HOMO band edge of P3HT, which is approximately (0.35-0.4)eV. The bias voltage where the extracted charges approach the plateau regime can be associated with the flat-band condition with in the device.

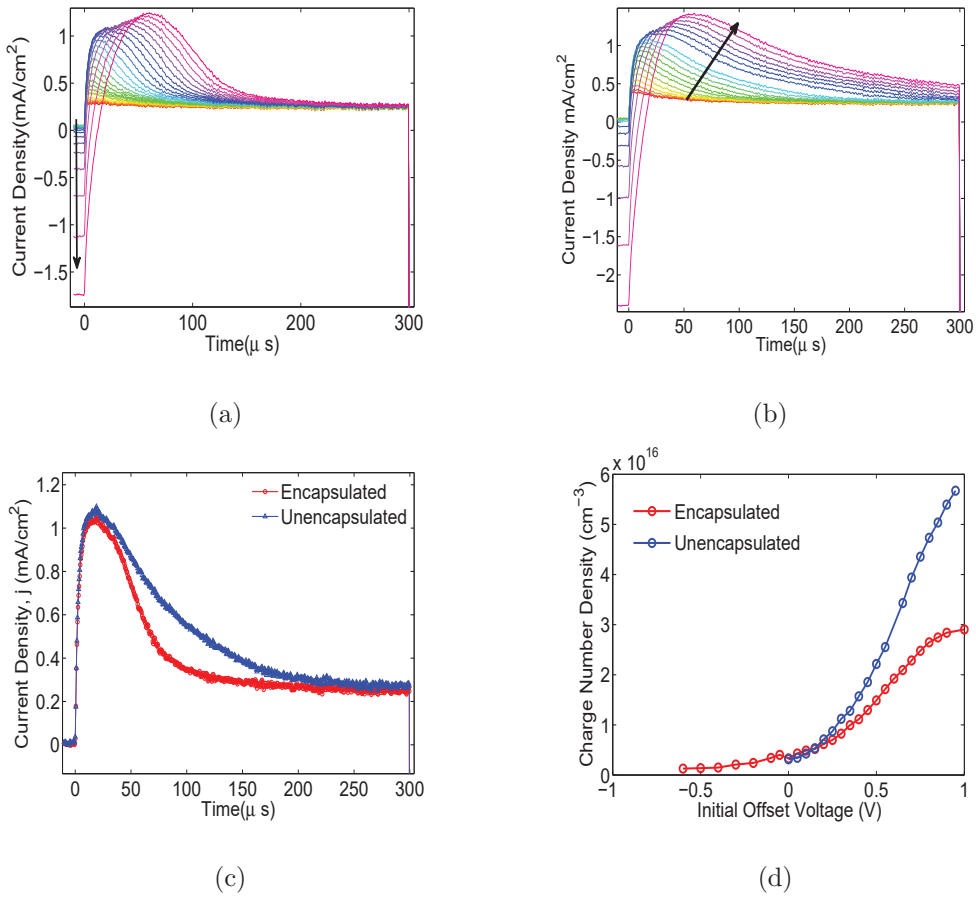

Figure 4.5: CELIV on a) a pristine and encapsulated , b) a pristine but unencapsulated P3HT-based devices, c) a close comparison of CELIV at +550mV initial offset, d) charge extracted for each kind of device. The arrow in a) andn b) indicate the direction of increasing initial offset from reverse-bias towards the forward-bias sweep.

The effective dielectric constant of the P3HT-based device is estimated to be 3.7 ± 0.3 from the displacement current, J_0, using Equation 2.15e.

Dark-injection Transient Currents(DiTC)

The dark-injection current transients (DiTC) is studied using CELIV. The rear edge of the ramp, the point in time where peak of the ramp drops back to the offset voltage

and stays until next ramp signal arrives, was analysed for both cases of encapsulated and unencapsulated devices. Figure (4.6) shows the current relaxation transients less than $30\mu s$ for the cases where the offset voltage of the ramp drops to +600mV. The unencapsulated device's transient is fit to biexponential function with time constants(weightage) $\tau_{short} \sim 0.1\mu s(56\%)$ and $\tau_{long} \sim 2.8\mu s(44\%)$. The encapsulated device also had the two decay components with $\tau_{short} \sim 0.1\mu s(94\%)$ and $\tau_{long} \sim 1\mu s(6\%)$ appears to be significant. The fast component(τ_{short}) is the relaxation of charges residing on the electrodes that contribute to the geometric capacitance (2-5)nF through the external sensing resistor 50Ω. The mechanism behind τ_{long} could be attributed either to 1) the hole transit time ($t_{tr,h}$) or to 2) the ohmic relaxation time ($t_{\Omega,h}$) in which the holes injected attain steady-state by the thermal carriers assisted by fast charge trapping and detrapping events with shallow traps close to HOMO band edge of the polymer. The fastest of the two phenomena is responsible for the observed dynamics. The hole transit time, $t_{tr,sclc} \sim t_{DiTC,sclc}/0.786 \sim 80\mu s/0.786 \sim 100\mu s$. The $t_{DiTC,sclc}$ is taken from the results shown in the Figure 4.7. The transient hole mobility ($\mu_{DiTC,sclc}$) is estimated to be of the order of $10^{-5}cm^2/Vs$. Considering the transient mobility that was calculated above, and considering dielectric constant for P3HT to be ~ 3.7, thermal charge density taken from CELIV with initial offset ranging from (1-500) mV shown in Figure 4.5(a), to be around $\sim 10^{16}/cm^3$, $t_{\Omega,h}is \sim (2-20)\mu s$ (see Section 2.2.1 for the time constant definitions). Therefore, for the device tested τ_{long} is dominated by the ohmic relaxation of the injected holes by the thermal carriers. Considering the weightage of the τ_{long} of both the cases, it infers that the unencapsulated devices which were more prone to the oxygen/moisture insurgency shows significant portion of τ_{long} of the total decay.

There is also a longer decay component, shown in Figure 4.6(c), of time constant $(30 \pm 10)\mu s$ only significant in the unencapsulated device. This decay is associated with the longer time of detrapping from the deeper traps. Once the bias is in the SCLC regime, it is hard to notice the decay due to the overwhelming dark space-charge limited current. The charateristic SCLC transients at higher biases are quite distinct as shown in Figure 4.7. The equation for mobility from the DiTC in SCLC regime, mentioned in Section 2.2.3, gives a hole mobility of about $(16 \pm 4) \times 10^{-6} cm^2/V - s$ at bias voltage of 0.9V. Ideally, plotting the t_{peak} against the bias voltages and extracting the mobility from its slope would give much reliable results. There was a limitation to the initial offset voltage of upto 1V in order to prevent the high currents that could damage the device. As a result, over a narrow range of bias voltage, there was no discernible change in t_{peak}. Nevertheless, a single point mobility measurement would still give the order of precision.

Hole mobility comparison

Hole mobility in the device has been measured from the SCLC regime of the current-voltage characteristics in the steady state, as well as using the CELIV and DiTC transients. Phenomenologically, the measurement regimes are different. The mobility from SCLC regime of steady-state I-V is the regime where all the deeper trap states are filled. In the case of CELIV and DiTC at SCLC, the charge extraction is in direct competition between the trapping and detrapping from the deep traps. CELIV is used to estimate the lower limit of the mobility in the trap-filling limit, while IV gives an upper limit of the mobility.

The built-in voltage is estimated from photovoltage, by saturating the device at

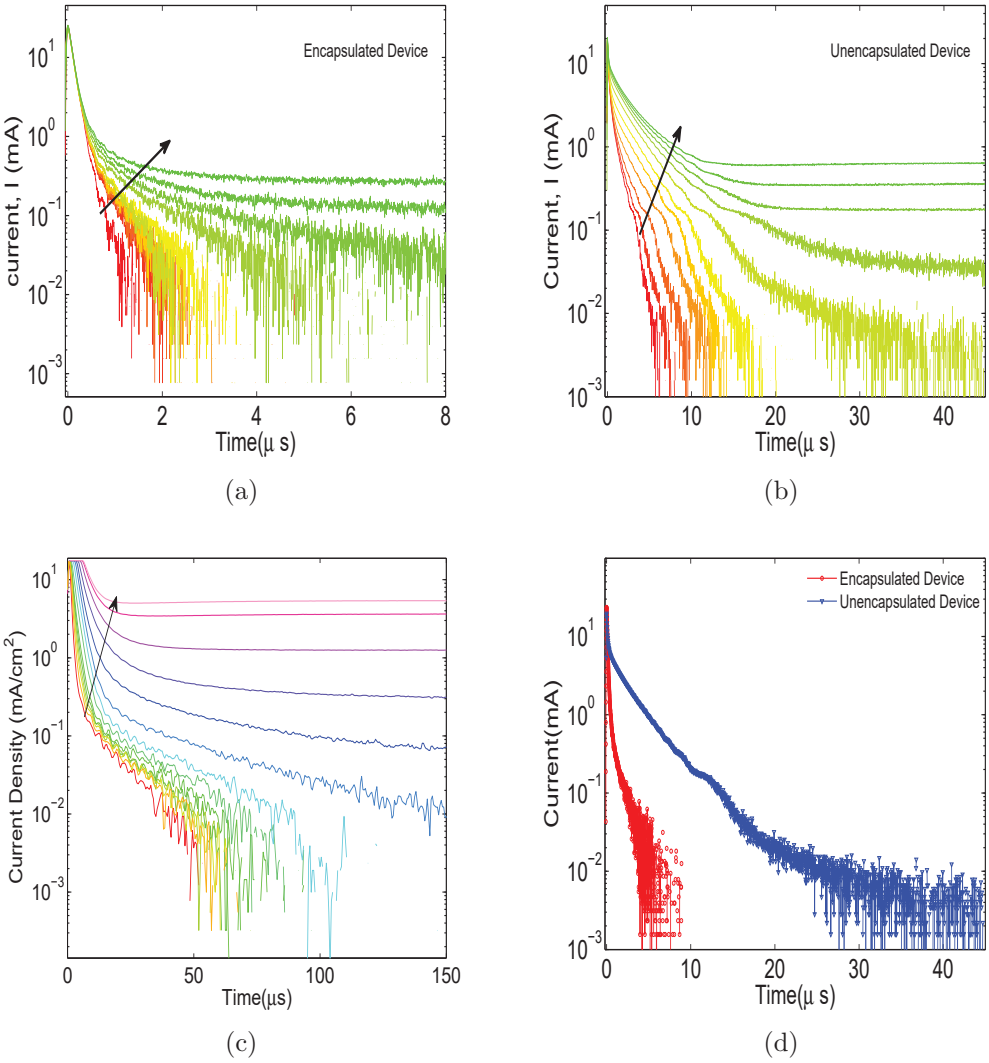

Figure 4.6: DiTC of a) encapsulated, b) unencapsulated, c) unencapsulated(over wider time range) P3HT-based device plotted for various initial offset voltages increasing from -0.5 V to +0.75 V in the direction of arrows annotated, and d) a comparison between the encapsulated and unencapsulated devices for a bias voltage of +600mV.

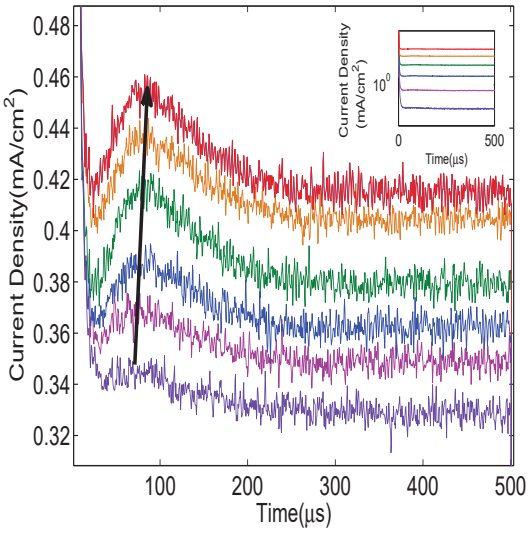

Figure 4.7: DiTC in the SCLC regime from 650mV(violet) to 900mV(red) zoomed in and arbitrarily adjusted current offsets for the ease of comparison. The actual dataset is shown in the inset.

approximately 3 suns intensity under open-circuit conditions, to be $(650 \pm 10)mV$. From the Equation 2.4 for SCLC, the hole mobility is calculated to be in the range of $(2-8)*10^{-4}cm^2/V-s$ for the electric field in the range of $(4-10)*10^4V/cm$. The hole mobility calculated from DiTC at SCLC, is $(16\pm4)*10^{-6}cm^2/V-s$. This value appears to be underestimated. The peak should be some where close to $(1-2)\mu s$ and not as the obvious one at $80\mu s$. Then the question is if this is the result of ringing effects. Hole mobility measured from CELIV over a range of $(0.5-5)*10^4V/cm$ initial offset field and a ramp rate of $10kV/s$ is $(5*10^{-6}-5*10^{-4})cm^2/Vs$. The mobility measured from CELIV equation highlights the relationship that the mobility decreases with increasing CELIV peak time. Although the mobility is inversely proportional to the t_{peak}, the equation does not relate the peak width of the CELIV current above the dispacement current level to mobility. In other words, the equation does not relate

the mobility directly to the charge density in the device. From the experiments, the trend shows that with the increase in the offset voltage of CELIV, the t_{peak} shows a plateau regime(and hence constant mobility) at lower biases up until $V_{offset} = V_{bi}$, followed by a steeper increase in t_{peak}(and hence decreasing mobility), and finally reaching almost constant t_{peak} or mobility. These trends are shown in Appendix C for P3HT. The mobilities measured above were all performed on the same device.

4.4 Effect of light-soak

A series of experiments have been done to assess the impact of soaking the devices in light. In order to compare the device characteristics before and after light-soak, it was made sure that the test sequences were in the order of complete dark, very weak optical pulsed and microscopic excitation, moderate light conditions to intense light-soaking tests, followed by repeating the testing in backward sequence. For example, dark-I-V, dark-CELIV and electroluminescence tests were done in complete dark conditions, and then the time-resolved photoluminescence test using very low energy(fJ) pulse over a microscopic spot, followed by light-IV with weak optical excitation, full exposure of white light/UV light to light-soak the device while recording steady-state photoluminescence and followed by reverse sequence of tests. This is to ensure that there is no unintended modification of the device characteristics from light exposure. The light-soaking tests were performed with either a halogen lamp with relatively lower intensity over long exposure times or with intense Mercury arc lamp over short exposure times.

4.4.1 Effect of light-soak on Current-Voltage characteristics

Figure 4.8(a) and 4.8(b) shows the current-voltage characteristics in logarithmic and linear scale before and after 30 minutes of white light Illumination from a Halogen lamp. The device under encapsulation showed decreased conductivity upon light-soak, whereas the unencapsulated device showed an increased conductivity in the SCLC regime. The photovoltage output from the device during light-soak is shown in Figure 4.8(c), recorded using oscilloscope with 100M Ω input impedance. While the decreasing photovoltage of the unencapsulated device is attributed to the fast photodegradation of the device whose edges and pinholes in silver electrode are exposed to the UV content of lamp in the presence of oxygen and moisture in the ambience; the increasing photovoltage of the encapsulated devices is an unexpected effect that will be discussed shortly.

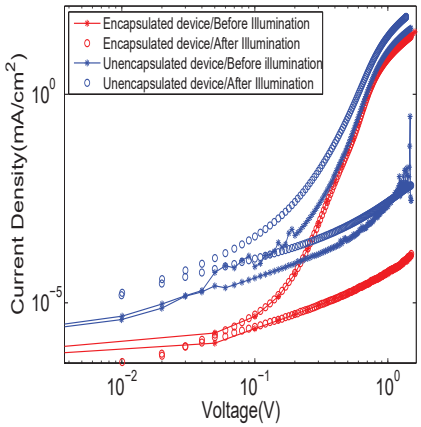

(a)

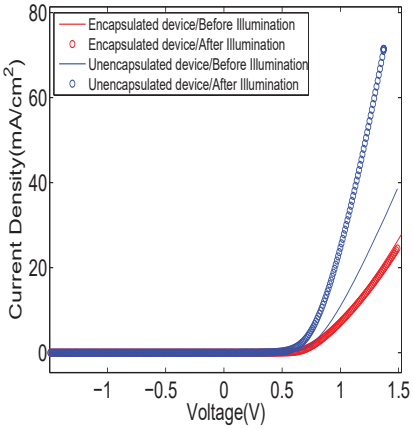

(b)

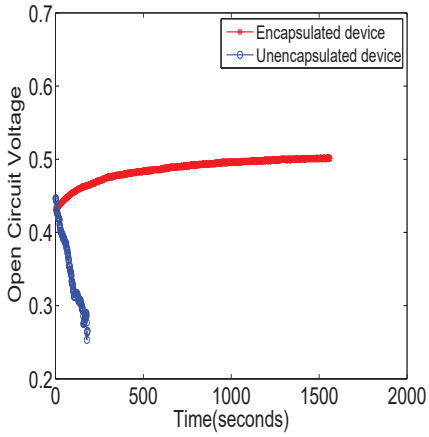

(c)

Figure 4.8: Dark J-V characteristics comparison of the encapsulated and unencapsulated devices before and after 30 minutes of halogen lamp's illumination a) log-log scale, b) linear scale. In c), the photovoltage off the device was simulataneously recorded while soaking the devices under light. The halogen lamp intensity of $(60 - 70)mW/cm^2$ was used for the light-soak.

4.4.2 Effect of light-soak on charge extracted from the device

Figure 4.9(a) shows the effect of soaking the encapsulated and unencapsulated device under Halogen lamp for 30 minutes on CELIV. The devices before and after

light-soaking are shown in the Figure 4.9(b). There is a clear decrease in the charges extracted for both encapsulated and unencapsulated device, although it is quite pronounced for the unencapsulated device. Likewise, the contact-limited DiTC transients for both kind of devices and pre- and post light-soak effects are shown in Figure 4.9(c). The effect of light-soak has consistent effects of reduction in the number of charges extracted and increase in the weightage of slow decay component of the DiTC transient for both encapsulated and unencapsulated device.

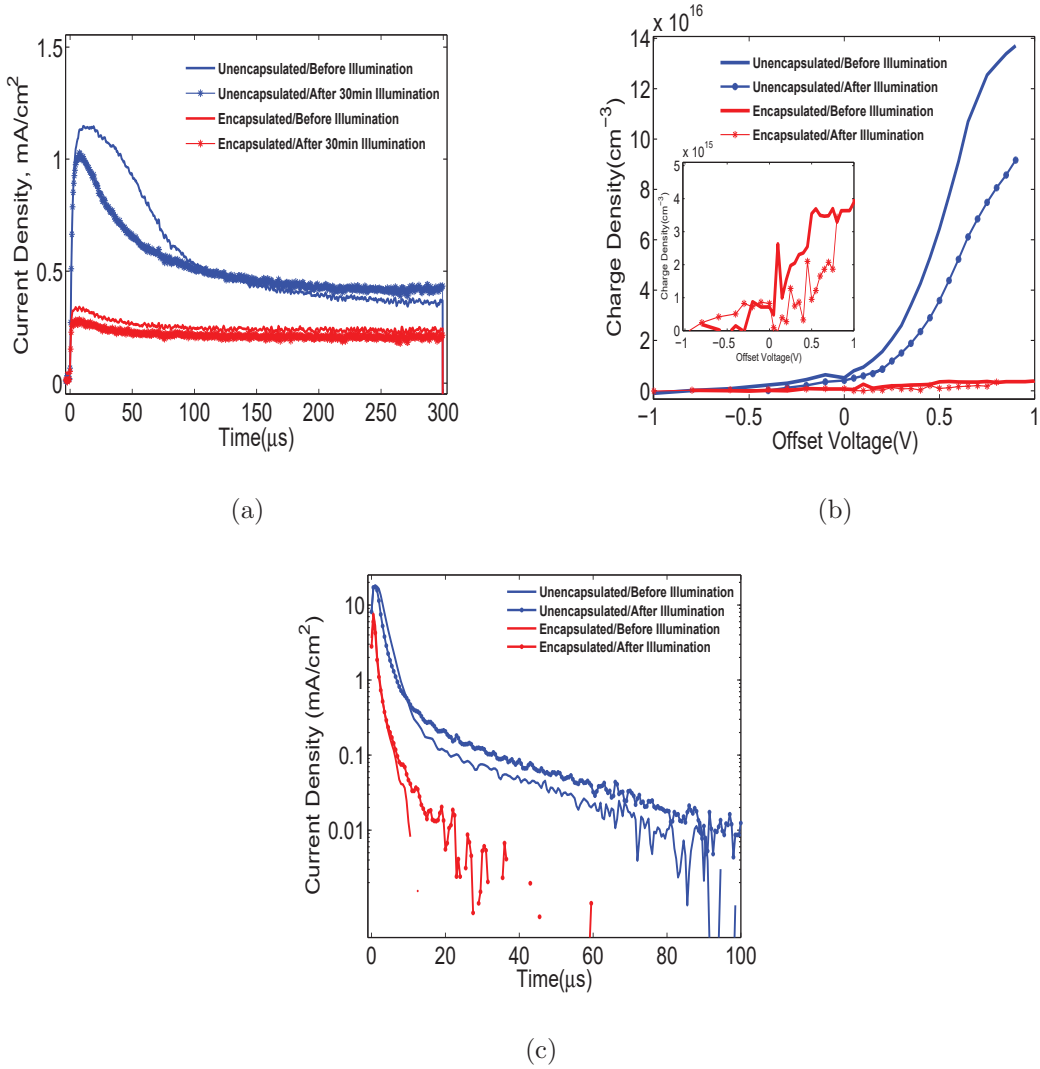

Figure 4.9: Effect of light-soak on an encapsulated/unencapsulated P3HT-based devices on a) CELIV current density, b) total charge extracted per unit volume, c) DiTC dynamics.

Very slow CELIV dynamics

This is the test that was performed on the devices that were used for the experiments above, after repeated illumination tests. There is an obvious 'fatigue' in the devices, especially that were not encapsulated, after multiple cycles of illumination.

This experiment was performed by initially setting a high offset voltage of about 700mV of the CELIV pulse. At time t=0 in the Figure 4.10(a), only the offset voltage is switched to zero volts, while keeping the ramp signal unchanged. The CELIV signal is then acquired from the oscilloscope every 600 ms. The charge extracted from the CELIV plotted against the time is shown in Figure 4.10(b). The repeated illumination has lead to irreversible photodegradation and introducing some deep traps which leads to very slow release of trapped charges. Although photodegradation processes were not explored in details in this work, this method of extraction dynamics could be useful for very slow dynamics.

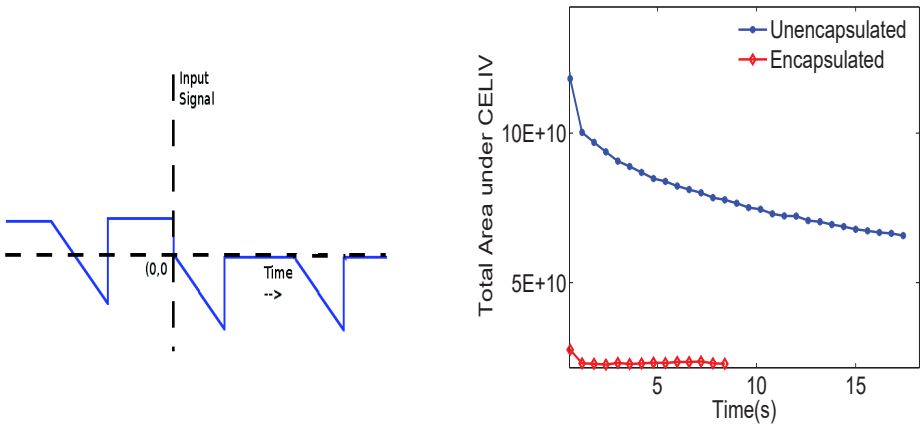

(a) (b)

Figure 4.10: Comparison of long time component of charge extraction from encapsulated and unencapsulated P3HT-based device.

4.4.3 Steady state Photo- & Electro-luminescence Studies

Photoluminescence

In order to make sure that the light-soak is not leading to any irreversible photodegradation, the PL and EL was studied on the devices; during the illumination at 405nm for the former whereas before and after the illumination for the latter studies. Interestingly, the PL from the device area under the top electrode(silver) showed an increase in the emission intensity with time as shown in Figure 4.11(a)[1]. Similar increase in PL was observed even for the unencapsulated. Clearly, the silver has been serving as an effective protective layer from the atmosphere. The simulataneous photodegradation was indeed noticed from the PL image of the unencapsulated device shown in Figure[] in section[]. Under the influence of photodegradation and enhanced PL, it however seems that the rate of degradation is the slower phenomenon. In contrary, the photodegradation was obvious in the case of excitation of the area not covered by silver and/or epoxy encapsulation, indicating the severe impact of the external agents, as shown in Figure 4.11(b).

[1]The enhancement in PL needs to be retested,as the excitation intensity from the arc lamp was not monitored

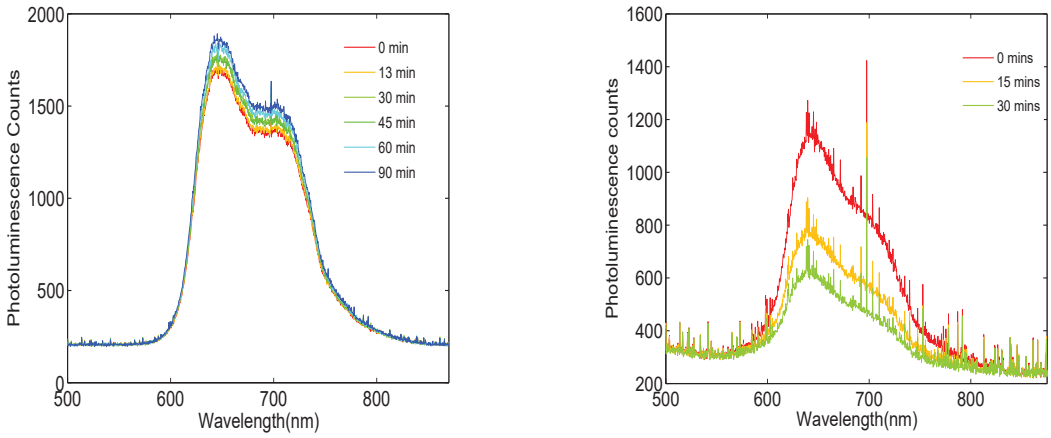

(a) (b)

Figure 4.11: Effect of constant illumination of 405nm excitation wavelength on the photoluminescence from a) the area directly under the silver electrode of an encapsulated device and b) the area uncovered by the silver electrode.

Electroluminescence

The electroluminescence from the encapsulated P3HT-based devices was measured before and after 30-minute white light illumination, to check for changes to the injection barrier potential and/or to change in the luminescence efficiency. Figure 4.12 shows the EL counts from the device before and after Illumination, at various biases. The threshold voltage (V_T) is around (1.40 ± 0.05) V in either case. The luminescence efficiency, however, seems to have increased post illumination.

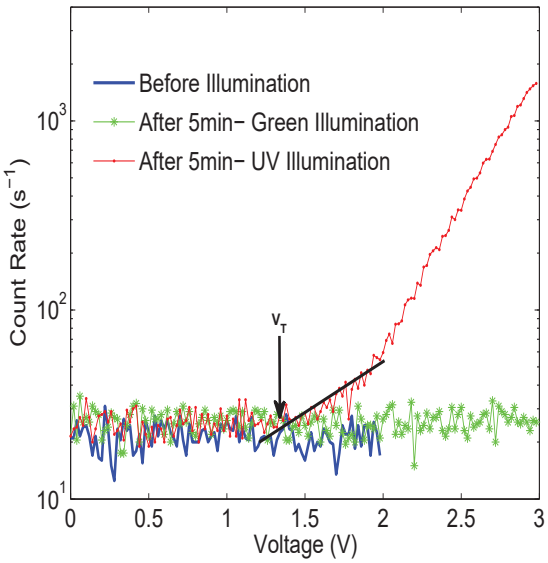

Figure 4.12: Effect of light-soaking on electro-luminescence intensity with respect to the applied forward bias.

4.5 P3HT:PCBM BHJ devices-IV and CELIV tests

P3HT has been mixed with acceptor-like molecules of PCBM with 1:1 wt.%, in order to monitor their effect on the charge transport properties. The current-voltage characteristics of P3HT:PCBM based device shows a clear kink and plateau between the ohmic and SCLC regime, which can be attributed to the possible distortion of the inter- and intra-plane stacking of the P3HT chains due to PCBM. In the work of Mihailetchi et al [113] similar plateau was seen to disappear post thermal annealing the device made of same compounds. Looking at the energy level, the tails states of the HOMO states of PCBM molecules may only contribute to small fraction to energetic disorder but may lead to spatial disorder towards the hole transport in the blend. The PCBM LUMO edge that lies in the mid-gap of P3HT may serve as empty states for electron trap/transport. The Figure (4.13(a)) for P3HT:PCBM

shows a much broader charge extracting CELIV peak as compared to P3HT device. This is most possibly due to the charge extraction that is sum of hole extaction from the HOMO or P3HT/PCBM and electron extraction from the LUMO of the PCBM. Comparing the charges extracted out of the P3HT-based device encapsulated and unencapsulated to that unencapsulated P3HT:PCBM based device, P3HT-based device is more susceptible to the doping due to external agents. Like P3HT-based devices, light-soaking P3HT:PCBM-based BHJ devices reduced the charges extracted using CELIV, although the reduction rate seemed slower.

4.6 Discussion

To summarize the effect of encapsulation and aging on IV, CELIV, photovoltage:

- IV characteristics -
  - Increase in SCL current and ohmic-regime current through the unencapsulated device compared to encapsulated device.
- CELIV characteristics -
  - Total number of charges stored in/extracted out of the device is higher in unencapsulated than in encapsulated devices.
- Contact-limited DiTC -
  - Significant fraction of slow relaxation component and additionally very slow relaxation component observed in the case of unencapsulated device.
- photovoltage -

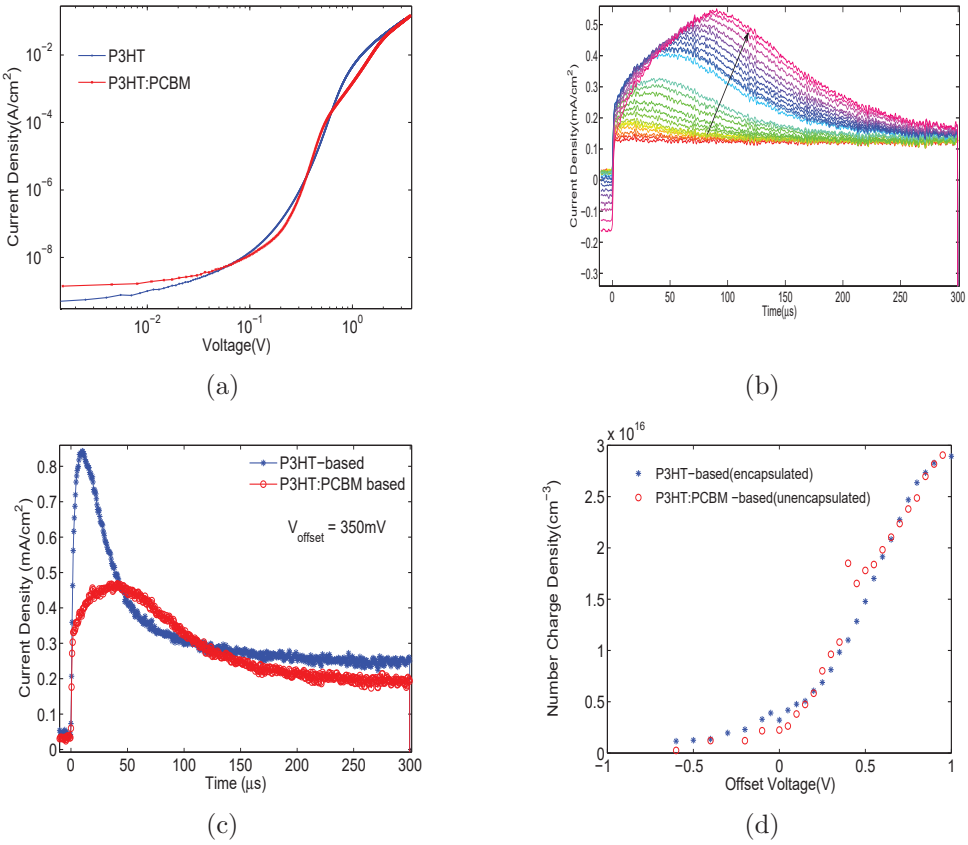

Figure 4.13: a) Dark J-V, and b) CELIV characteristics of P3HT:PCBM-based device. c) CELIV dynamics at forward-bias offset of +250mV and d) number charge density extracted out of P3HT-based and P3HT:PCBM-based device shown for close comparison.

  - photovoltage, at about $60mW/cm^2$ from Halogen-based light source, increased for encapsulated device, whereas decreased for the unencapsulated device.

- Photoluminescence-

  - Higher PL efficiency for encapsulated devices as compared to unencapsulated devices.

The increased ohmic current in unencapsulated device is indicative of increased hole dopants concentration with time and exposure. The same is confirmed from the higher density of charges extracted off the device in CELIV. The decreasing photovoltage and PL efficiency with time indicates the photodegradation that is imminent in the presence of light and oxygen/moisture. The longer relaxation time in the DiTC is associated with the participation of the shallow traps in trapping/detrapping phenomena. The energy band alignments for the encapsulated and unencapsulated devices can be depicted as shown in Figure 4.14.

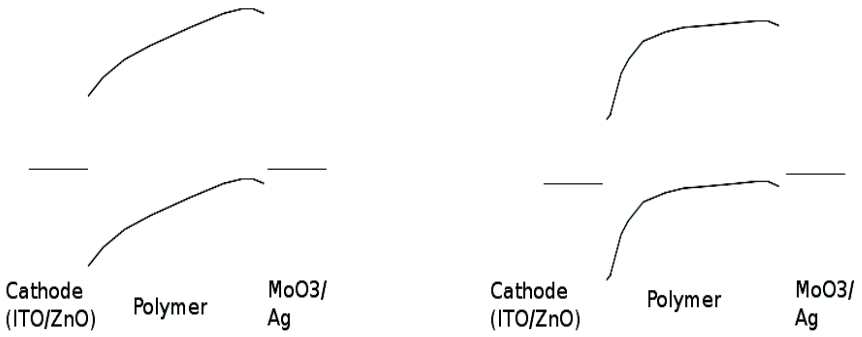

(a) Encapsulated device (b) Unencapsulated device

Figure 4.14: Energy band alignments compared for encapsulated and unencapsulated devices of the same layer configuration.

To summarize the effect of light-soaking on IV, CELIV, photovoltage, photo and electroluminescence on the encapsulated P3HT-based devices:

- IV characteristics-
  - Decrease in SCL current and increase in ohmic-regime current after light soak.
- CELIV characteristics-

  - Decrease in charges stored in/extracted out of the device after light-soak.

- Contact-limited DiTC-

  - Increased weightage of the slow relaxation component after light-soak.

- Photoluminescence

  - PL intensity seemed to be increased with continous excitation with wavelength $\lambda_{exct.} = 405nm$ over a period of 90 minutes.

- Electroluminescence

  - EL efficiency clearly increased post light-soak.

The observations from the effects of light-soak are discussed under possible bulk- or interfacial- related effects. One of the critical issue to be addressed before further discussion is if the effects seen were excitation-wavelength sensitive. In one of the tests, shown in Figure(4.15), where the change in electroluminescence intensity was recorded by soaking the device under different wavelength bands. The bands chosen out of HBO Mercury arc lamp were $[365 \pm 10]nm, [445 \pm 25]nm, [525 \pm 25]nm, [610 \pm 35]nm$. Although the excitation intensities were not uniform over the different bands, the net effective flux of photons incident on the devices was kept almost constant or within an comparable range by varying the exposure time. The test was performed under optical microscope. The excitation area is about $50\mu m$ and excitation bands were picked by varying the interference filters. The same spot on the device was excited starting from long wavelength band and towards shorter wavelength. Figure(4.15) shows that there is a sharp enhancement in the EL when excited with wavelength shorter than 410 nm. In the present case excitation at 365 nm triggers

the drastic enhancement in EL.

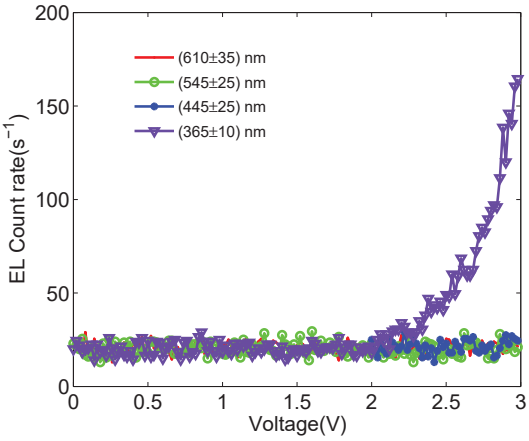

Figure 4.15: Electroluminescence dependence on excitation soak-light wavelength

Likewise, time evolution of charge extracted before and after lights of different wavelengths used to light-soak the device are shown in Figure 4.16. The arrows in the figure show the points of the time where the device was soaked to lights of different wavelengths(colors in the plot) for about 1 minute, followed by charge extraction measurement. The exposures were in the sequence of [525/50]nm, [365/20]nm and [610/70]nm, annotated by the numbers 1,2 & 3 respectively in the figure. One of key features common to all the exposures is the revival of charge extraction to the pre-soak condition. However, for the UV exposure, the reduced charge extraction is instantaneous and drastic compared to the green and orange light soaks. This shows that, all the earlier tests done with white light exposure from the halogen and arc lamp can be assumed to have affected the device characteristics mainly due to the UV component of the white light exposure.

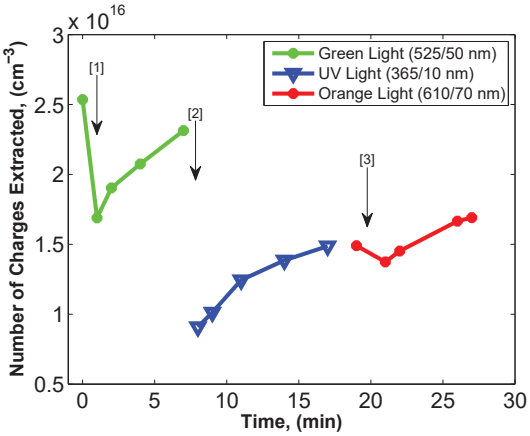

Figure 4.16: Time-evolution of charges extracted using CELIV, with injection at 300 mV, tested for three different wavelengths used for soaking the devices. The arrows indicate the time of light exposure of wavelengths [1] (525/50)nm, [2] (365/20)nm, [3] (610/70)nm .

One or more of the following possibilities could have led to the observations aforementioned:

- Band-bending modification at the ITO/ZnO interface,
- Migration of Oxygen vacancies, Zn interstitials etc within ZnO,
- Photo-desorption of Oxygen,
- Hybrid Charge Transfer Exciton (HCTE) states,
- Polymer doping/dedoping,
- MoO3 is doping the polymer over time,
- Orientation of Polymer molecules themselves at the interface/bulk,

Bulk of ZnO: Migration of Oxygen vacancies/Zn interstitials -

Zinc Oxide exhibits unintentional n-type doping, which some scholars argue it is due

to the interstitial zinc sites or oxygen vacancies while others contend the possibility of traces of hydrogen could as well be responsible for the effects[114, 115]. For the present case, let us assume that the oxygen vacancies are responsible for the extrinsic semiconducting behaviour of ZnO, as irrespective of the origin of the cause, the final interpretation of the results would still not be affected. Oxygen vacancies ,V_O^+, that are positively charged, are known to drift within the crystal under external field[]. Under the forward bias applied to the devices, i.e. when a positive potential is applied to the anode (silver electrode) with respect to the cathode(ITO), the V_O^+ drift away from the anode. The drifting V_O^+ accumulate within ZnO at the ZnO/ITO interface, thereby locally doping the ZnO layer at the interface. This further reduces the depletion width at the interface, making relatively easy conduction channel/ohmic contact between ITO and ZnO by tunnelling across thin depletion region. The drift of these defects is considered one of the causes for hysterisis effect seen in sweeping (sweep-rate 0.02V/s and a hold time of $\sim$ 5sec at the maximum forward-bias voltage before sweeping in the reverse direction) the devices in forward(reverse bias to forward bias) and backward(forward bias to reverse bias) as pointed out by Cheng Li et al [116]. Memristors based on metal/insulator/metal(MIM) configuration are known to exhibit this kind of behaviour [117, 118]. A question yet to be addressed is how UV is affecting these dynamics. Figure 4.17(a) clearly shows that UV and other wavelengths exposure affecting the hysterisis in dark-IV characteristics. While a prolonged green light exposure for 5 minutes suppresses the hysterisis, short UV exposure of 40 seconds results in a drastic suppression of hysterisis. The sharp decrease and current minima in the backward sweeps of voltage at about 300 mV in the case of device not treated by light(black asterix) and as well as treated by $(570 \pm 25)nm$

(red asterix)light exposure in Figure 4.17(a) indicates that there is a new source of electric field formed acting against the applied field. The temporary source of field is nullified in the reverse bias at about -(700 - 800)mV for the same data set. This is where the oxygen photodesorption seems to play a critical role.

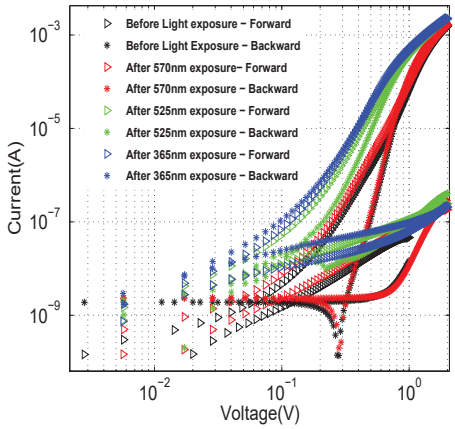

(a)

Figure 4.17: Effect of light of different wavelengths exposure on the a) direction of current-voltage sweep characteristics. Forward direction refers to voltage bias swept from reverse bias to forward bias to the device and backward refers to the other way.

Interface-effect:Possible oxygen-photodesorption from the metal oxide. Like TiO_2, the nanostructured ZnO acts as an oxygen getter from the surrounding, which in our case is from the residual oxygen in the polymer,possibly trapped during synthesis or packaging and/or from the atmosphere as the ZnO layer is spin-coated in open-air conditions. The electronegative oxygen that adsorbs at the interface of ZnO/P3HT, thereby oxidizing ZnO i.e. eventually increasing its fermi level towards intrinsic semiconductor. When photons of energy higher than bandgap of ZnO (typically, 3.2eV) excite ZnO creating e-h pair, the holes aide in reducing the oxygen, eventually aiding

in oxygen desorption [119, 120] from the ZnO surface, thereby raising the fermi-level of ZnO back to pristine case. A similar reduction process can also be assisted by photoexcitation of P3HT as well. This phenomenon could also in turn lead to increasing open-circuit voltage with light-soaking time as witnessed in Figure 4.8(c).

In a similar work by Anton Sundquist et at.[72], it was shown that the reduction in charges extracted using CELIV is possibly due to reduced work function of the cathode(ITO/TiO_2, in their case). The enhanced built-in voltage, therefore, reduces the charge reservoir of holes injected from the anode. This has two implications: 1) Reduction of S-shape in the photo-IV curve observed in organic photovoltaics[69, 68] 2) Onset of electroluminescence at higher forward bias voltage. However, in the present case, both the scenarios are not evident. Unlike a device based on P3HT:PCBM, there was no S-shape witnessed in the photo-IV of P3HT-based device. However it must be pointed out that the short-circuit current,J_{sc} was an order smaller in P3HT-based device as compared to P3HT:PCBM-based device, and hence relatively lower possibility of recombination at the contacts. The s-shape in photo-IV was witnessed for P3HT:PCBM without ZnO transport layer and it was subdued after light soak. The onset of electroluminescence should have been shifted Electroluminescence efficiency, on the other hand, has increased after light-soak evident from Figure 4.12.

Strong evidence of bulk ZnO or ZnO/Polymer interface effect: Figure 4.18 shows the fractional decrease in the charge extracted post UV-light soak for three different cases:

- A: $ITO/P3HT/\mathrm{MoO_3}/Ag$,
- B: $ITO/ZnO/P3HT/\mathrm{MoO_3}/Ag$,
- C: $ITO/ZnO/P3HT:PCBM/\mathrm{MoO_3}/Ag$,
- D: $ITO/P3HT:PCBM/\mathrm{MoO_3}/Ag$

In the above mentioned sample, the key differences are the presence/absence of ZnO layer and PCBM molecules. Ideally, the test to show the strong evidence of the role of interface layer would have been more conclusive if the comparison was done on P3HT-based device with and without ZnO. However, due to the limitation of CELIV technique which needs atleast one blocking contact(ZnO layer), the reference sample A: $ITO/P3HT/\mathrm{MoO_3}/Ag$ could not be used for CELIV test. The possible discontinous contact of PCBM with ITO layer in P3HT:PCBM-based device offers the sufficient blocking feature to perform CELIV on it. From the Figure 4.18, clearly the P3HT:PCBM based device without ZnO showed almost no effect of UV-light soak compared to the other two devices.

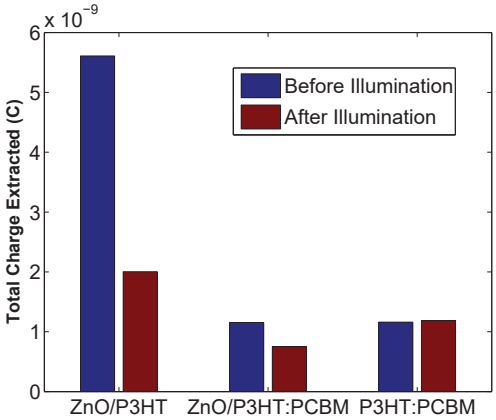

Figure 4.18: Charge extracted before and after UV-illumination studied for samples based on ZnO/P3HT, ZnO/P3HT:PCBM and P3HT:PCBM.

There was no noticeable enhancement in EL efficiency in the P3HT-based devices without ZnO layer before and after UV light-soak. The EL enhancement in the case of P3HT-based devices with ZnO layer after UV light-soak could then be attributed to the reduced work-function of the ZnO following oxygen photodesorption, and leading to efficient double injection and recombination. An interesting phenomenon called HCTE recombination seems to be involved in the observed electroluminescence.
The possibility of HCTE between the inorganic and organic materials which have been emphasized by other groups [121, 122] and [123]. The HCTE recombination at the interface of ZnO and P3HT seems to play a key role in our device afterthe light-soak. The threshold voltage (V_T) where there is a detectable electroluminescence starts is about 1.40 ± 0.05(equivalent to wavelength range (855 - 918)nm) noticed in the Figure 4.12 for the P3HT-based device. While an excitation spectrum would give a much better understanding into the origin of long-wavelength emission should it be from the tail state conduction bands to valence band radiative recombination.

However the possibility of HCTE recombination was further consolidated with another polymer-based device to be discussed in the chapter to follow. It was noticed in a PCDTBT-based device that the threshold voltage(V_T) for electroluminesnce was about $(1.05 \pm 0.05)V$ (equivalent to wavelength range (1078-1180)nm, which is close to the upper limit of detection for the Si-APD we have used). The oxygen photodesorption is aiding is the efficient HCTE recombination at the ZnO/Polymer interface, followed by monomolecular radiative recombination with in the polymer at higher bias voltage. The EL at the higher bias voltage +3V and PL of PCDTBT device is shown in the Appendix D.

Bulk-effect: The photo-treatment could be leading to further photodoping the polymer [46] medium in the presence of residual O_2, increasing the hole-carrier density and leading to improved ohmic conductivity, as obvious from the Figure 4.8(b) for the encapsulated device. It must be remembered that the encapsulated device does not necessarily mean that the device is completely devoid of oxygen. In the energetics picture, the fermi level of the polymer moves closer to the HOMO band of the polymer, thereby potentially reducing the depletion region between the cathode(ITO/ZnO) and the polymer, similar to the band-bending condition shown in Figure 4.14(b) for an unencapsulated device. This should have increased the number of charge extracted out of the device in CELIV, in contrast to what is observed. Clearly, photodoping is not one of the possibile phenomenon happening during the light-soak tests.

Bulk-effect: De-doping reminiscing the thermal annealing- There have been reports mentioning the decrease in charge extracted after thermal annealing could be a result of de-doping[124]. Thermally annealing the polymer above their glass transition temperature(T_g) enables to the escape of dopants like oxygen, thereby also leading to

decrease in hole conductivity[125]. Similar reduction in charges extracted, in the case where the device was tested under nitrogen environment, was observed by Seemann A. et al[124]. During the polymer de-doping, the charges trapped by the shallow traps like oxygen are detrapped under light exposure, thereby reducing the current in the ohmic regime as well as the charges extracted through CELIV, in accordance with the observed phenomena.

From the above discussion, the possible energy level alignment scenario at the interface of ITO and ZnO layers before and after UV light soak can be summarized as shown in the Figure 4.19. Figure 4.19.1 shows energy levels of ITO and ZnO layers before they were brought in contact. The levels designated [A] and [B] are the probable fermi energy levels for a pristine n-type ZnO(or UV soaked device) and surface-defects induced oxidized-ZnO, respectively. Figure 4.19.2 and 4.19.3 show the charge-depleted band-bending trends with respect to the two fermi levels of ZnO. Notice the thin depletion width in Figure 4.19.3 corresponds to both pristine-ZnO or UV-treated device. The thin depletion layer facilitates efficient tunneling-assisted injection of charges into the device from the cathode side leading to enhanced radiative recombination at lower biases applied. Similar light- soak tests have been performed on inverted polymer-diode devices by other groups [126, 127, 128] align with the results obtained here.

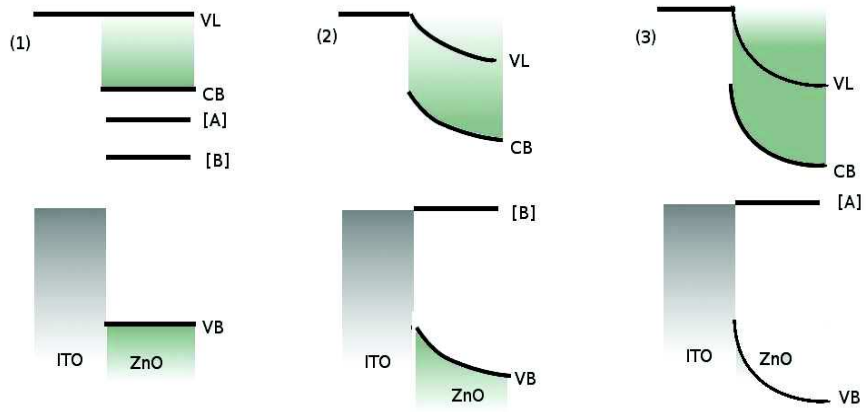

Figure 4.19: A cartoon of energy-levels alignment of metallic ITO and semiconductor ZnO 1) before contact with two possible fermi energy levels designated [A] and [B](see the text), 2) at the interface with higher work-function of ZnO at level [B], 3) at the interface with lower work-function of ZnO at level [A]. VL- Vacuum Level, CB - Conduction band edge, VB - Valence band edge

4.7 Conclusion

P3HT-based devices with the layer configuration $ITO/ZnO/P3HT/\mathrm{MoO_3}/Ag$ were tested with and without the charge-selective buffer layers(ZnO & $\mathrm{MoO_3}$). ZnO layer plays a decisive role in building the potential across the device under short-circuit conditions. Experiments including I-V, CELIV, photovoltage and Electroluminescence were performed to see the effects of encapsulation and light-soak on P3HT-based diodes. The exposure of the diode to the atmosphere clearly increased dopant(hole-type) concentration in the device leading to increased dark conductivity. A crucial observation is the tunability and revivability of the work function of ZnO under the UV light-soak. Exposure to UV is most likely leading to photodesorption of O_2 from the bulk interface of ZnO/P3HT in a device that is encapsulated. While reduced ohmic-regime current and charge extracted indicate towards dedoping of the polymer

itself, the enhanced photovoltage and electroluminescence do not support this argument.

What is not clear as of this point is whether the shift is just in the work-function of ZnO or the complete vacuum-level shift at the interface i.e. if the UV is curing the interfacial dipole if there exists one. In this regard, the same device configuration has been tested on two polymers, namely MDMO:PPV and PCDTBT in the chapter to follow immediately. Also, at this point we are not sure if MoO_3, which serves the purpose of providing ohmic contact for silver with polymer, is also a source of oxygen contaminants and/or if the silver atoms, which if sneak through the MoO_3 layer, could affect the band-bending properties at the anode interface. In Chapter 6, LBIC technique has been used to probe the device spatially with sub-micron resolution.

Chapter 5

Comparative study of Polymers

5.1 Introduction

The current chapter does a comparative study of the opto-electronic properties of three polymer-based devices namely P3HT, MDMO:PPV and PCDTBT under encapsulation. The chemical structure of the three polymers are shown in Figure 3.2 and their corresponding LUMO and HOMO levels in Table 5.1 for brevity. There are three-fold reasons in doing the comparative studies on these polymers. First of all, it serves the purpose of cross-checking if the results observed in the previous chapter were polymer-specific. Secondly, it is expected to give a better understanding about the energy level alignments at the polymer-contact interfaces, as the other interlayers and contacts are the same for all. Thirdly, each polymer has a different tendency of packing itself during a thin film formation which eventually decides the device's charge transport characteristics and its stability as well [23]. with a common device configuration, it is possible to compare the mobilities, trap densities and possibly assess their energetic location and different structural susceptibilities to the traps. As most of the concept related ground work has been laid in Chapter 4, the discussions

on the results & analysis are carried out hand-in-hand in here.

Unlike the previous chapter, no attempts were made to do the comparative study on the effect of encapsulating the device. All the devices made and tested in here were encapsulated. Though this reduced the complexity in data acquisition and analysis, comparing different polymers in congruence with the un/encapsulation will definitely throw some light on the polymers susceptibility to degradation/stability. In the following sections, current-voltage characteristics and CELIV/DiTC in dark analyzed, followed by the effect on the same before and after light-soaking on all the three polymer-based devices.

Polymer	LUMO (eV)	HOMO (eV)	Bandgap (eV)/(Ref)	Emission Peak (nm)
P3HT	-3.0	-5.0	2.0 /[129]	641
MDMO: PPV	-3.2	-5.3	2.1 /[129]	590
PCDTBT	-3.6	-5.5	1.9 /[130]	661

Table 5.1: Energy levels and emission peaks comparison for P3HT, MDMO:PPV & PCDTBT[a].

[a]The photo-and electroluminescence of the devices can be found in the supporting info Appendix D.

5.2 Current-Voltage Characteristics

5.2.1 Dark J-V

Figure 5.1(a) shows the current-voltage characteristics of the three polymers built with same configuration i.e. with ITO as transparent cathode, Silver as the top metal contact, ZnO as hole-blocking layer while MoO_3 forming an ohmic contact between Silver electrode and each of the polymers. All the devices were encapsulated before taking them out of glovebox and testing them. Table 5.2 shows the drift

mobility for each kind of devices measured from the SCLC regime along with the exponent of voltage (which is also the slope in logJ-logV plot) which was not fixed for the fits. Clearly P3HT has relatively higher mobility, followed by PCDTBT and MDMO:PPV. Appendix A, shows the procedure employed to extract the effective mobilities of these polymers. From the energy levels taken from the literature, the expected built-in voltages are also shown in the table 5.2. The V_{bi} is the difference in fermi-level of ITO/ZnO taken to be 4.35eV [131] and HOMO of the polymers, as the MoO_3 at the anode renders an ohmic contact between the polymer and silver electrode.The V_{oc} were measured to be $(0.65 \pm 0.02)V, (1.10 \pm 0.02)V, (0.95 \pm 0.02)V$ for P3HT, MDMO:PPV, PCDTBT respectively. While the V_{oc} and V_{bi} are within the range for P3HT, it is not the case with PCDTBT and MDMO:PPV devices. As no surface analysis were done before or after coating the layers of the device, the real reason for the loss or gain of open-circuit voltage in these devices is unclear. The current-voltage slopes did not seem to be limited within the voltage range studied and hence the voltage drop across small series resistances (usually $< 35\Omega$) were not considered. The dielectric constant required for the mobility calculation were derived from the displacement current component of the CELIV, as shown in the section[].

Polymer	P3HT	MDMO:PPV	PCDTBT
SCLC mobility, $(cm^2/V-s)$	(1.0 - 2.5) $\times 10^{-4}$	(4.0 - 5.5) $\times 10^{-7}$	(1.0 - 1.8) $\times 10^{-5}$
Slope of the SCLC fit	(1.95-2.1)	(2.4-2.9)	(1.9-2.2)
Expected $V_{bi}(V)$	~ 0.65	~ 0.95	~ 1.15
Measure $V_{oc}(V)$	0.65 ± 0.02	1.10 ± 0.02	0.95 ± 0.02

Table 5.2: SCLC fit parameters compared for P3HT, MDMO:PPV & PCDTBT - based devices

Some of the key observations here to note- MDMO:PPV shows higher slope of (2.4

- 2.9) and not 2, the expected exponent for a SCLC fit, as followed here by the P3HT and PCDTBT. Considering its very low mobility and the higher slope coefficient, the MDMO:PPV is be treated as an insulator for the fixed device configuration. . The negative current until about 300 mV in the case of MDMO:PPV is due to SMU's current detection limit.

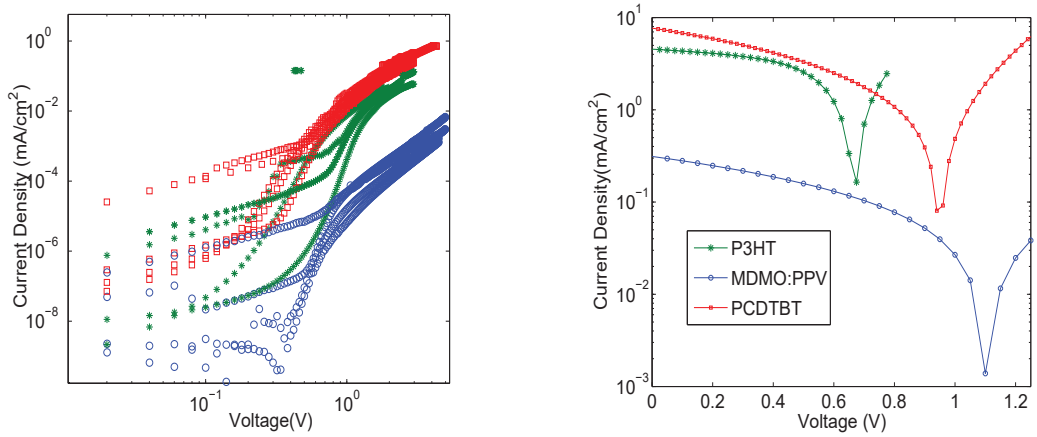

(a) (b)

Figure 5.1: (a) Dark J-V and (b) Photo-J-V characteristics of P3HT, MDMO:PPV and PCDTBT based devices.

5.3 CELIV

5.3.1 Dielectric Constant of active medium

The inset in Figure 5.2 shows the dark-CELIV performed on an encapsulated P3HT, MDMO:PPV & PCDTBT-based devices for various ramp rates. One can deduce the dielectric constant of the material sandwiched between the electrodes from the displacement current after depleting the device from charges. In other words, there is no additional charge injection and the capacitance (hence,dielectric) measured is

exclusively from the charges residing on the electrodes. The plot in Figure 5.2 shows that I_0 (current values shown inside the box in the inset) is plotted against various ramp rates of the voltage. The geometric capacitance, which is the slope of the fit, is $(1.21 \pm 0.01)nF$. For the device of active area $(0.070 \pm 0.005)cm^2$ and thickness $(180 \pm 5)nm$, the relative permittivity of the P3HT is calculated to be 3.7 ± 0.3. Likewise, for MDMO:PPV based device the relative permittivity is measured to be 3.3 ± 0.2, in accordance with the fitting parameter used in [132] using impedance spectroscopy tests and that of PCDTBT device is 4.36 ± 0.3. The dielectric constant measured semiemperically using either of the procedures has a high sensitivity to the area and especially the thickness of the device.

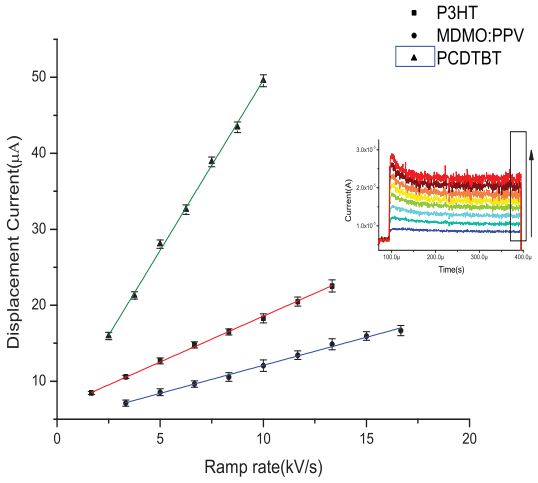

Figure 5.2: The displacement current J_0 for different ramp rates of input signal at 0V of offset voltage. The slope from the fit is the geometric capacitance of the device.

$$J_0 = \frac{\epsilon_r \epsilon_0}{d} \frac{dV}{dt}, \tag{5.1a}$$

$$C_d = \frac{\epsilon_r A \epsilon_0}{d}, \tag{5.1b}$$

Polymer	Mw	Concentration	film thickness	Dielectric Constant
P3HT	(50-70) kDa	20 mg/ml	175 ± 5	3.7 ± 0.3
MDMO: PPV	~ 50 kDa	7 mg/ml	185 ± 5	3.3 ± 0.2
PCDTBT	(20-40) kDa	7 mg/ml	60 ± 5	4.36 ± 0.3

Table 5.3: Dielectric constants of polymers measured using CELIV from P3HT, MDMO:PPV & PCDTBT -based devices

5.3.2 Charge Extraction

Charges extracted with constant ramp rate of (10kV/s) but by sweeping the initial offset bias is compared for all the three polymer-based devices. While the ramp rate is fixed for all the devices, the ramp period was increased in the case of MDMO:PPV device, considering its quite low mobility and slow extraction of charges. The very low reverse bias dark current lets one to sweep the device to higher reverse bias voltage. In the case of PCDTBT devices, the ramp period and amplitude were reduced due to high reverse leakage current in these devices. Figures 5.3(a),5.3(b),5.3(c) show the CELIV traces for P3HT, MDMO:PPV & PCDTBT based devices, and Figure 5.3(d) projects the charges extracted out of the devices at various offset biases.

Clearly, the density of charges extracted out of P3HT-based devices outnumbers those from MDMO:PPV or PCDTBT-based devices. This points to the possibilities that 1) the P3HT has higher affinity for Oxygen than the other polymers, and hence higher density of shallow and deep traps, or 2) although Polymer-MoO3/Ag interface

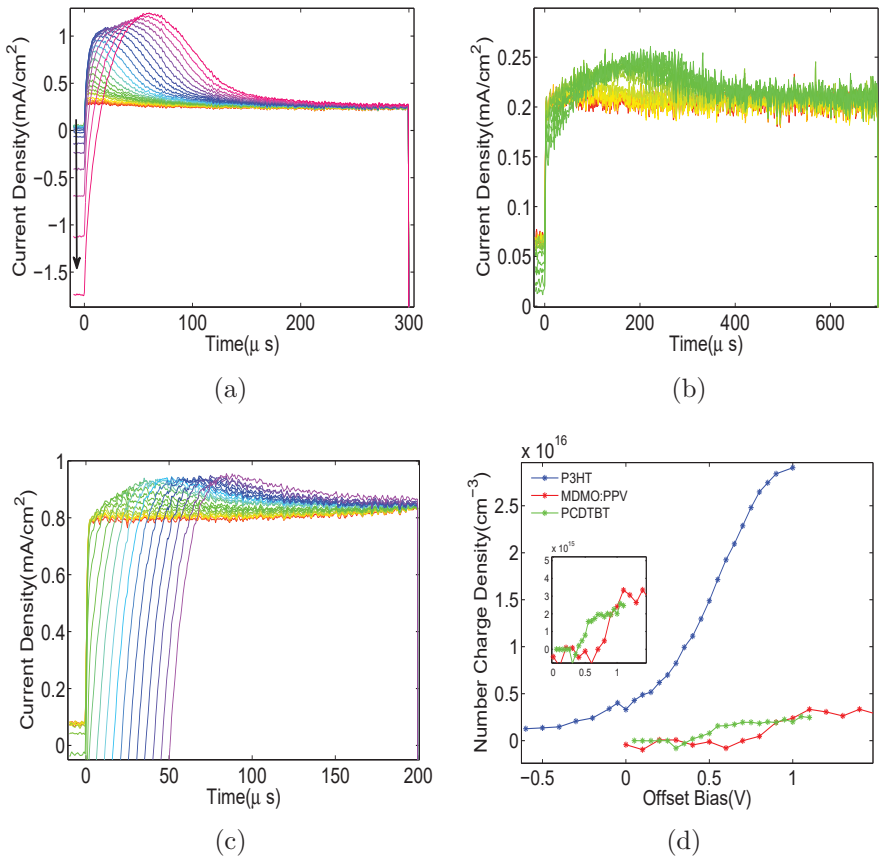

Figure 5.3: CELIV on a) P3HT, b) MDMO:PPV, c) PCDTBT at various offset voltages and d) total charge extracted out of each kind of device at various offset voltages. Ramp rates were fixed at 10kV/s for all the devices, although the ramp periods were different.

is supposed to form good ohmic contact it seems to be not the case in MDMO:PPV-based device, and hence there could be contact-limited poor hole injection at the anode. The charge mobility calculated from CELIV and I-V charateristics is summarized in the Figure 5.4. Of the three possibilities, the first one seems to be more likely reason for high density of charge extracted. For the 2nd possibility, it was observed from the EL studies that for all the polymers the turn on voltage was within (1.2-1.5)V, and hence the limited hole injection at the anode seems less likely.

5.3.3 Mobility calculations from CELIV

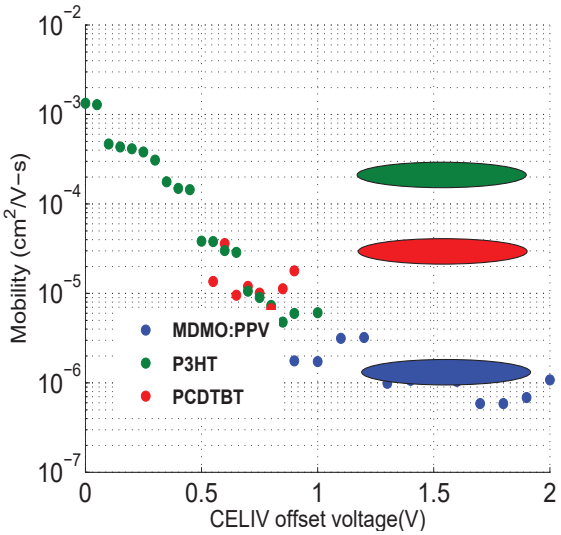

Figure 5.4: Charge mobilities measured from CELIV (dots) and SCLC (ellipses) regimes of steady state IV characteristics. The ellipses are not real data, but a closest approximation annotated to the actual CELIV data.

5.4 Light-soaking effects

Just like the preceding chapter, the devices were tested for IV, CELIV and EL before and after soaking the devices under light. Charge extraction using CELIV decreased post light-soak for all the three devices (not shown here). The increase in photovoltage with time was observed in the three kinds of devices. All the facts pointing to a common possibility of change to the work function of ZnO with the light (UV) exposure. However, consistent change in IV characteristics with the enhanced EL signal after light-soak, opened up some room to analyze the devices closely. Figure5.5 below shows the current-voltage characteristics of device configuration $ITO/ZnO/PCDTBT/MoO_3/Ag$ encapsulated, taken before and after light-soaking ($Intensity \sim 70mW/cm^2), Halogenlampat2500K$ for 10 minutes.

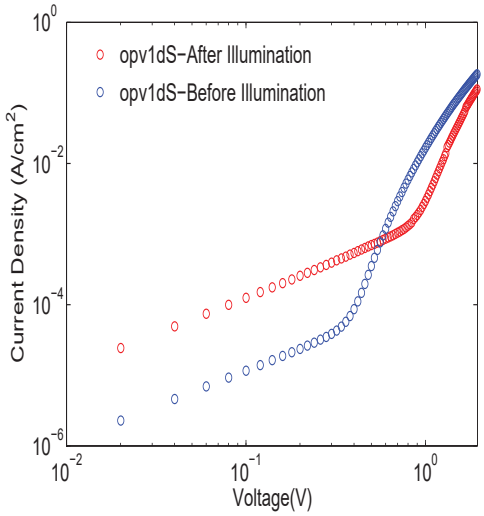

Figure 5.5: Dark current-voltage characteristics taken before and after light-soak on PCDTBT-based device.

Similar IV curves were observed on 9 out of 12 encapsulated devices tested. The plausible increase in built-in voltage, V_{bi}, as the onset of SCLC seems to be shifted. There is also an apparent increase in the ohmic current, possibly from the increase in the thermal equilibrium charge carriers due to photodoping. Although it appears like the SCLC is reduced after light-soak, it can be argued that it is merely an increase in the V_{bi} that delayed the onset of SCLC and hence seemingly reduced SCLC. If and when corrected for the internal V_{bi}, the SCLC might in fact be the same. In order to conclude that a precise information on the V_{bi} is absolutely necessary. In case where the SCLC is really depressed due to light-soaking, the current observation can be closely associated with the predictions of Lampert and Rose's work[60] when the SCLC is from the two-carrier injection and not just one-carrier. In their work, it was shown analytically that the Mott-Gurney's law of $J \propto V^2$ relationship in the case of single-carrier device holds true even in the case double-injection devices. One more very interesting observation was that the space-charge limited current will be reduced

in the double-injection case compared to the single-carrier case, along with increase in the number of thermal carrier. This effect according to the authors surfaces due to the recombination kinetics. To test their prediction, one way is to make two similar devices such that one supports only single-carrier injection and extraction, while the second device would have to inject two-carrier plasma by appropriately choosing the contacts. Another way is to test the device not with an intimate contact but with replaceable contacts. The first way doesn't guarantee the same active medium configurations (especially for the spin-coated amorphous medium), while the second way without intimate contact would introduce unpredictable series contact resistances. In this work, we were able to switch from single carrier (with an inefficient double injection) to two-carrier injection by modifying one of the contacts using UV-light on the same device. The intensity used to modify the contact is low enough that it is assumed that the active material in use is not modified during the light exposure. The electroluminescence count rate detected at various bias voltages for the same spot of the sample before and after light-soak is shown in Figure (5.6(a)). Although the enhancement in EL efficiency was observed in all the three polymer device kinds, the enhancement in PCDTBT-based devices showed many orders of increase in EL (What could be the possible reasons. - Is it the active medium was relatively thinner (70nm) unlike P3HT or MDMO:PPV or Is it that PCDTBT has better quantum efficiency.). So much so that the EL can be seen with bare eyes. This property of tunability of the ZnO's workfunction was implemented to stencil out the letter 'Q' onto the device, as shown in Figure (5.6(b)). In fact, this could be an interesting way of making diffraction-limited submicro LEDs that can be stencilled out of the devices, although it is understandable that they can be lossy.

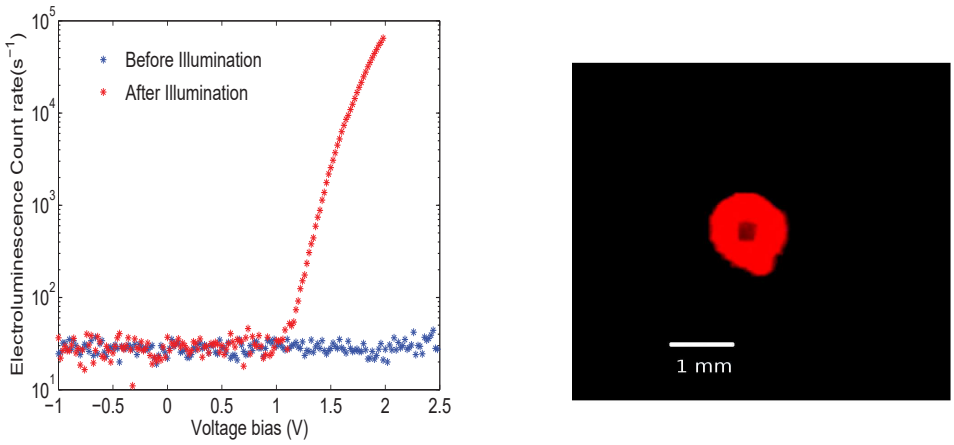

(a) (b)

Figure 5.6: a) Electroluminesnce at various bias voltages tested on the same device, before and after light-soak on PCDTBT-based device, b) UV-stenciled letter 'Q' showing electroluminescence from the PCDTBT-based device.

Similar effects were observed in P3HT-based and MDMO:PPV-based device with same layer configuration. The 'breathing effect' that was seen in terms of charge extraction from P3HT-based devices, has been revisited here again in MDMO:PPV based device but with EL studies. Figure(5.7(a)) shows the EL versus forward bias applied to the MDMO:PPV-based device, that shows the scans done before and after intermittent light-soaks. The EL count rates measured at 4V bias are plotted with respect to time after bouts of light exposure in Figure (5.7(b)). The device was soaked for 5 minutes using Halogen lamp set at 10V ($\sim 2500K$) each time.

5.5 Conclusion

The three polymer-based diodes with the same layered configuration have been tested for current-voltage and CELIV characteristics, and the effect of light on the same. The mobilities from the SCLC of dark JV and CELIV conform to the values upto the

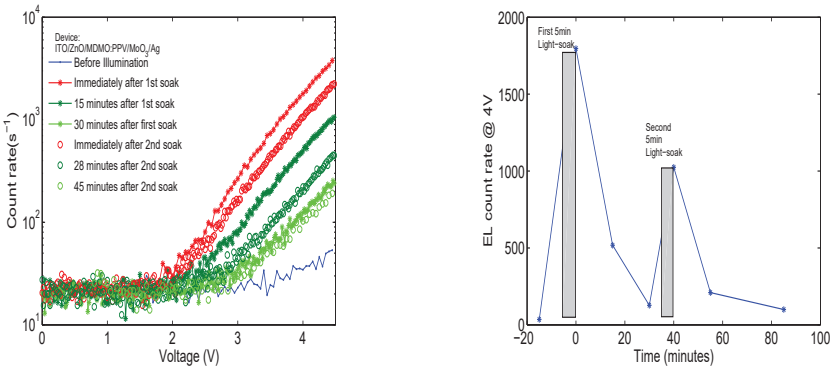

(a) (b)

Figure 5.7: a) Electroluminescence bias voltage tested on MDMO:PPV based device, immediately and after some time delay post light-soak shown for two such cycles, b) Electroluminescence intensity measured at 4V immediately after and with time delay post 5 minute light-soak using Halogen lamp at 2500K.

orders mentioned in the literature. The open-circuit voltages however did not follow the trend of energetic difference between the cathode (ITO/ZnO) and the HOMO of polymer as expected. The dark charge extracted from the devices, at any forward bias offset, were manifolds higher for the P3HT as compared to MDMO:PPV and PCDTBT, emphasizing the susceptibility of P3HT to oxygen and moisture which dope the polymer p-type. Effect of illumination: In CELIV, like before, the charge extracted has reduced after light soak. The increased ohmic-regime current, reduced SCL current along with efficient electroluminescence after light soak were observed in all the three polymers. This conforms to thoeretical outcome shown by Mark and Rose [60] for when the single-charge injection is replaced by double-injection. Like in P3HT-based device, HCTE recombination seems to be playing a key role in PCDTBT and MDMO:PPV based devices as well. The above results also emphasizes the point that the all the effects noticed in Chapter 4 are true irrespective of which polymer was under test and that oxygen photodesorption and modification at the interface of

Cathode and polymer is most likely the cause of observed effects. 'Breathing effect': Like the charge extracted using CELIV and J-V characteristics seen in Chapter 4, the EL signal also has revived back partially after a bout of light exposure. So the question not addressed yet is that, to what physical phenomenon should the signal revival time be associated with. Is it the time it takes for oxygen and/or moisture that are physically desorbed from the light-soak tending to be chemisorbed at the interface of ZnO and polymer? or is it the physical diffusion of these entities?

Chapter 6

Imaging: LBIC, Fluorescence, Bright-Field

6.1 Introduction

Laser beam induced current (LBIC) technique has been used for photocurrent profiling of the device prepared discussed in the ealier chapters. The motivation behind these studies is to probe the spatial defects or degradation incurred by the external entities like Oxygen, moisture etc., or by the UV light induced photooxidation/degradation, identify the contribution of different layers contituting the device, locate the effect of intentional inclusion of acceptor materials like PCBM, ZnO nanoparticles etc. in the device. The LBIC scans are further complemented with the Bright-field (BF) and fluorescence (FL) imaging. The excitation intensity fluctuation was monitored using a fraction of the excitation optical power using a Si photodiode and the light reflected off the sample is also monitored using a second Si photodiode. The second Si photodiode helps locating the edges of the top electrode of the device more precisely. The excitation laser light of wavelength 532 nm was chosen for LBIC. From the earlier studies, it was understood that the green light does minimal modification to the interface or active media properties over interrogation time at each

pixel and yet overlaps with the polymer peak absorption range. The excitation pulse powers varied within (5 - 250) nW over the focussed beam spot.

Laser beam spot-size at focus: The objective lenses with 100x magnification that has a numerical aperature of 0.75 was used for focussing the laser beam. The laser beam spot size at the focus is estimated to be $\sim 0.7\mu m$ at 1σ assuming the gaussian distribution of intensity of the form. The intensity distribution in the airy-rings around the central spot is neglibly small. Figure 6.1 shows image of the laser spot along with its intensity profile.

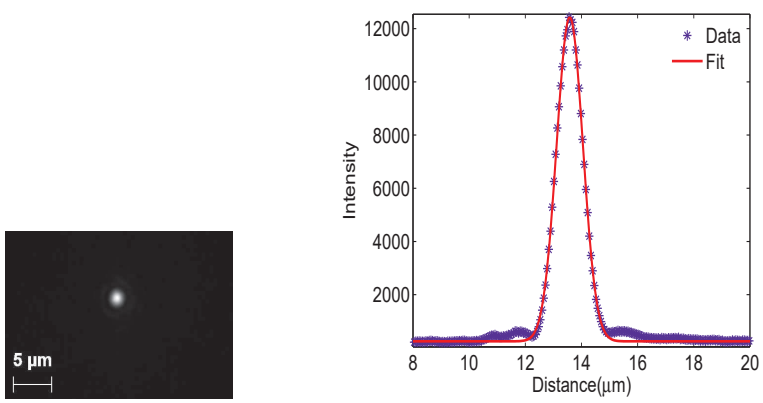

(a) (b)

Figure 6.1: a) Laser spot image at the focus of the 100X objective of numerical aperture 0.75, b) Intensity distribution across the laser spot diameter.

6.2 Effect of MoO_3 layer

It is crucial to know the role of each layer in the overall device performance. Most of the work discussed so far emphasized on the possible modifications to the ZnO/polymer interface upon light-soak. However the effect of MoO3 has not been taken into the discussion so far. Recent studies show that there is a possible polymer doping due to

MoO_3 [133, 134, 135] and/or modification between metal and metaloxide [136]. In one of the sets of samples that were prepared during the top-electrode size optimization processes, it was noticed that there was a lateral spatial mismatch between the top electrode combination, i.e. between MoO_3 and Ag in this case. This is due to the spatial separation of the two crucibles that are used to vapour-deposit MoO_3 and Ag, and a non-negligible thickness of the mask that is in the proximity of samples fixed to substrate holder in the PVD system. The thicknesses of MoO_3 and Ag were about $(7 \pm 1)nm$ and $(80 - 100)nm$, respectively. Figures 6.2(a) and 6.2(c), show the bright-field and fluorescence images of the left edge of the device respectively, while Figure 6.2(b) and 6.2(d) show similar images for the right edge of the device. The device is initially intended to be of the configuration $ITO/ZnO/P3HT/MoO_3/Ag$. However, due to the shadowing effect of the mask, the left edge of the device is devoid of MoO_3 under the Ag by about $100\mu m$ and the right edge of device has MoO_3 under Ag and extended about $100\mu m$ to the right of the edge. Here the edge is referred to the sides of topmost Ag electrode. The part of the image named as 'A' is the area of the substrate that are not covered by MoO_3 or Ag. The region labelled as 'B' is the area of the polymer covered only under Ag, the region labeled 'C' is the area covered under both MoO_3 and Ag, while the part labeled 'D' is the area of the polymer covered by only MoO_3 and not Ag.

From the fluorescence and bright-field images, some of the key points to notice are:

- Silver as a top electrode is protecting the polymer from degradation. The photoluminescence is quite prominent from the region that is covered under silver.

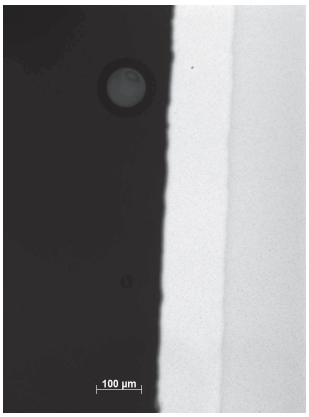

(a) Bright-Field (edge-1)

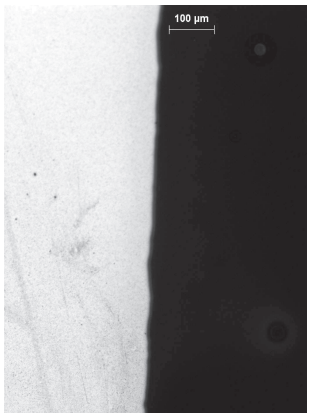

(b) Bright-Field (edge-2)

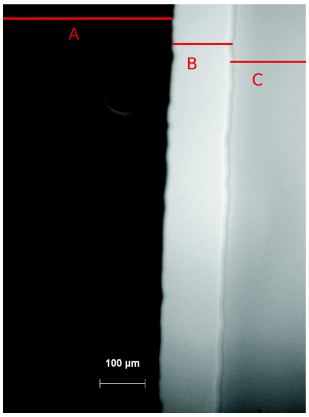

(c) photoluminescence (edge-1)

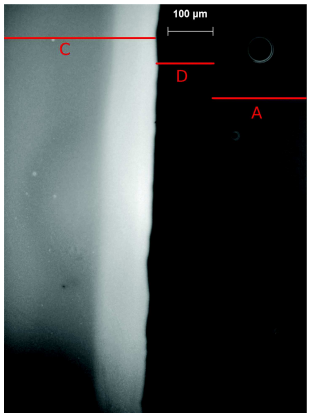

(d) photoluminescence (edge-2)

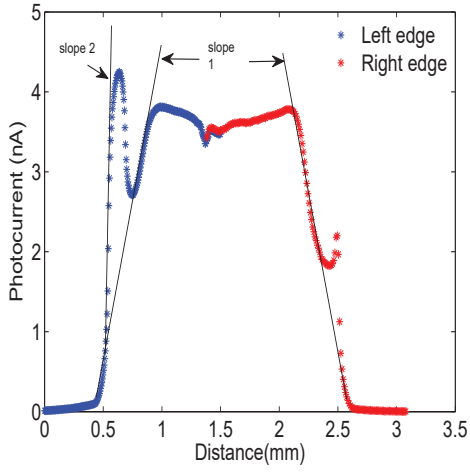

(e) LBIC across the width of the device

Figure 6.2: Optical imaging and photocurrent profiling of a P3HT-based device.

- Relatively high photoluminescence yield at the edges on either side of the electrode for about $100\mu m$ towards the center of the device, evident from the Figures 6.2(c) and 6.2(d). It is not clear at this point for the cause of enhanced photoluminescence at the electrode edges of the device that is encapsulated. The photodegradation due to oxygen/moisture ingressed at the edges should have degraded the photoluminescence.

Figure 6.2(e) shows the LBIC profile scanned on the device along the width of the top electrode. The width of the electrode estimated from the distance between the two photocurrent peaks noticed at either of the edges of the Ag electrode is same as the mask window used for depositing the electrodes which is about (2.00 ± 0.05)mm.

- A relatively smaller slope (indicated by 'slope 1') of the increasing photocurrent scanning into the device, indicative of device degradation from the edges towards the center.

- A high slope photocurrent spikes (indicated by 'slope 2') on either edges.

- Another interesting observation is the high photocurrent extracted in the absence of MoO_3 i.e. in the region 'B', seen on the left edge (edge1) of the device. There could be more than one reason for the photocurrent enhancement like, 1) a possible plasmonic enhancement by the silver particles, 2) interference of the incident with the reflected light leading to a constructive intereference in the active medium, 3) an unexpected hole-barrier by MoO_3 at the anode.

6.3 Effect of encapsulation

The previously mentioned lateral mismatch of the MoO_3 and Ag electrode was curbed by following two procedures.

1) using a thinner mask for the material vapour deposition, and 2) rotating the substrate holder in the vapour-deposition system during deposition.

Figure 6.3(a) shows the bright-field and fluorescence images along with LBIC scans of a small selected region on the encapsulated and unencapsulated devices close to the top electrode edge.

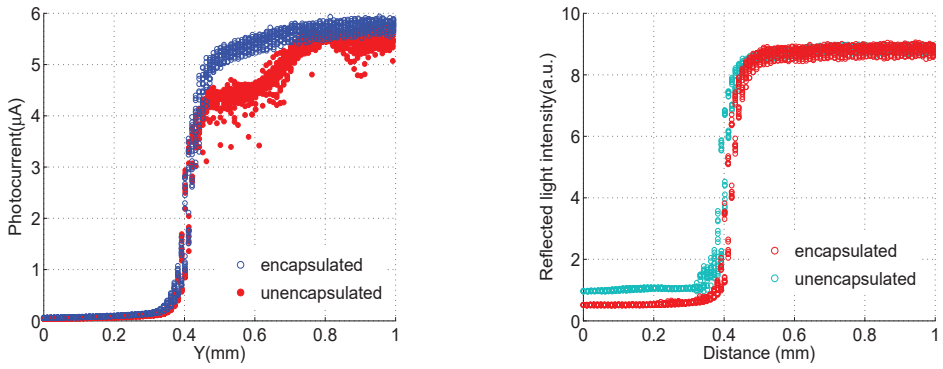

(a) (b)

Figure 6.3: a) LBIC of an encapsulated (blue) and an unencapsulated (red) P3HT based devices, b) Reflected light off the P3HT-based devices encapsulated and unencapsulated.

The degradation patterns were clearly noticed in the devices that were unencapsulated, and quite prominent at the edges, indicating the detrimental effects of the oxygen and/or moisture in the atmosphere. In the case of no encapsulation, pinholes in the top silver electrode is also another channel of device degradation. Similar defects have already been reported by [137] and [138]. These pinhole defects are quite

discernible from the photoluminescence images although not obvious from the bright-field image. There were no noticeable photoluminescence degraded spots in the case of encapsulated devices (not shown here). Time-resolved photoluminescence of the selected spots on and off the device shows the photoluminescence intensity quenched non-radiatively at the pinholes within the device and outside the device exposed to air.

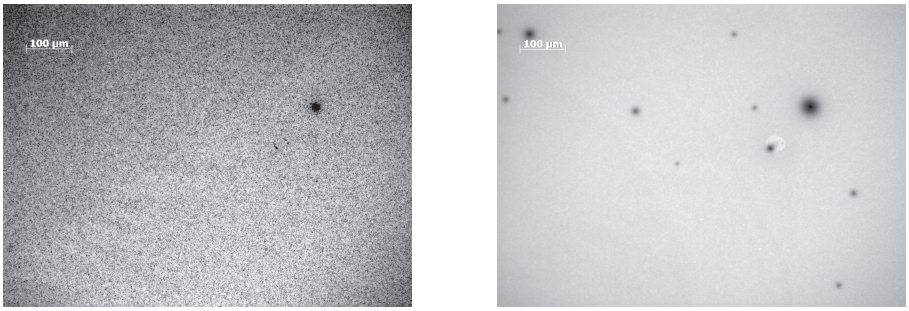

(a) (b)

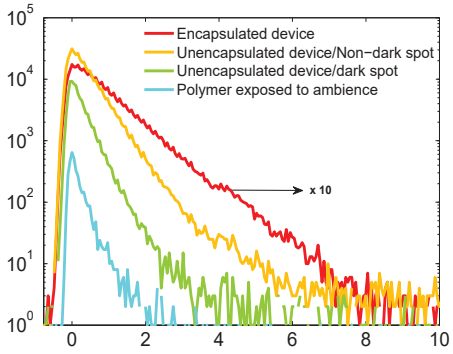

(c)

Figure 6.4: Steady-state a) bright-field and b) photoluminescence images, and c) Time-resolved photoluminescence of the selected spots in the unencapsulated device.

6.4 Effect of UV-exposure

In Chapters 4 and 5, it was noticed that there was a 'breathing' effect in terms of electroluminescence and charge extracted with time after bouts of UV exposure. LBIC was used to simulate the similar effects in terms of photocurrent. The encapsulated device was scanned for LBIC in 1D, followed by UV light exposure for 3 minutes over an area of diameter approximately $600\mu m$ under optical microscope. This time the focal spot size is limited by the spatial arc size of the light source (Hg Arc lamp) for the same 100x objective. While keeping the UV-exposed areal spot undisturbed (locked by engaging the stepper motors along X and Y axes (XY being plane of the sample)), repeated LBIC scans were performed intermittently for upto 45 hours after UV-exposure.

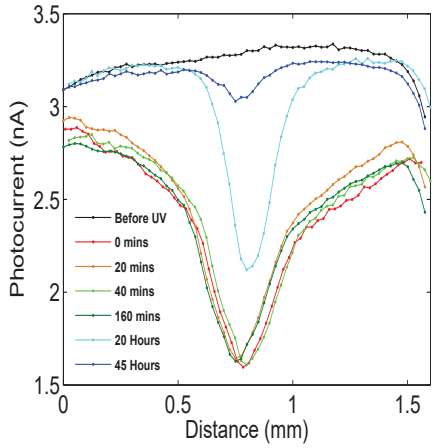

Figure 6.5: Time-evolution of LBIC before and after UV exposure.

The scan immediately after UV exposure showed a decreased photocurrent in the form of a 'valley' is shown in figure 6.5. This aligns with the photo-IV characteristics where the short-circuit current decreases while the open-circuit voltage increases after

UV-treatment. Although there was no noticeable change in the photocurrent for atleast upto 160 minutes, the photocurrent recovery was clear after 20 hours in the dark conditions and a very significant recovery in 45 hours post UV exposure.
The increase in V_{oc} was associated with the increase in the built-in voltage from the reduced work-function or vacuum shift, which in-turn seems to be due to the photodesorption of the O_2 molecules. The same argument holds true for the dip in the photocurrent observed after UV exposure. One of possibilities is that with the decrease in work function of ZnO, there must possibly be a barrier from the depletion region at the interface of ITO and ZnO, as shown in Figure 4.19. The other possibility is that with the physically desorbed oxygen available, there are more electron traps readily available leading to the reduced photocurrent.

6.5 Conclusion

LBIC scanner with a pixel resolution of $3\sigma \sim 2\mu m$ is achieved to study the microscopic spatial defects of the devices. For the duration of study (few months), the encapsulation has been effective in protecting the device from being ingressed with moisture (to a higher degree compared to Oxygen or other gases). Photoluminescence mode of detecting the spatial defects is more effective than the bright field imaging. The effect of UV-expsosure on the photocurrent off the diode at short-circuit conditions has be tested. The photocurrent revives back to pre-UV exposure state of the device within the period of about 45 hours. The revival in photocurrent conforms with signal revival in CELIV and electroluminescence tests done in Chapters4 and 5. Although the exact recuperation rate is not determined here, the test points to the possibility of measuring molecular oxygen (or other forms)'s rate of diffusion

and/or the rate of transitioning from the physically desorbed Oxygen to the chemical readsorption, should the arguments towards the conclusions of Chapter4 and 5 stay valid.

Chapter 7

Conclusions

7.1 Summary

The work presentated in this thesis has been motivated by the necessity to understand a) the charge injection, transport and extraction in and out of an organic semiconductor based diode, b) the role of different layers that constitute the device, c) the role of charge trap states (intrinsic/extrinsic) at the interface or bulk of the device. In this direction, the devices were subjected to exposure to the open air ambient conditions and light-soaking effects. The devices studied were "sandwich-type and inverted" polymer-based diodes with layer configuration- ITO/ZnO/Polymer/MoO_3/Ag.

Comparing unencapsulated P3HT-based diodes against the encapsulated ones, aided in identifying the key differences in the IV,CELIV, EL and PL characteristics incurred by the atmospheric entities, predominantly air and moisture. This has helped in ruling out the possibilities of extrinsic factors when studying the light-soak effects on the same devices. Hole mobilities in the polymers have been quantified and compared using steady-state IV characteristics and, CELIV/DiTC transients. The DiTC transients were useful to extract the relaxation time constants associated with

$R_{load}C_{geometric}$, charge transit time(t_{tr}), ohmic relaxation time (t_{Ω}).

The devices showed highest sensitivity to the light-soak in the UV. Comparing all the techniques done before and after the UV light-soak, it is understood that UV exposure is possibly leading the physical photodesorption of oxygen(hydrated) from the interface of ZnO and the polymers. This leads to the photoreduction of ZnO layer and further reducing the work-function of ZnO. In order to rule out the possibility that the observed light-soak effects were not polymer-specific, similar experiments were conducted on devices based on MDMO:PPV and PCDTBT. All the devices and tests pointed towards the probable work-function modification of ZnO. Although not tested, at this point the role of MoO_3 in the observed effects cannot be ruled out, which according to other scholars' work seems to be altering the dopant concentration of the polymers as well. One of the tests we did is to perform a microscopic LBIC scan at the edge of the device electrode, where a spatial offset of the MoO_3 layer with respect to silver electrode was noticed under microscopic optical imaging. A 'breathing effect' was observed in the IV, CELIV, EL, photovoltage, LBIC signals after repeated bouts of light exposure, where the signal would almost resume to pre-soak conditions. This phenomenon is attributed to the physical photodesorption of oxidizing agents during light exposure followed by chemical readsorption of the entities to the interface.

7.2 Future Work

Material Study:

Now that the setup has the ability to study IV, CELIV and photoexcitation studies, all in-situ on an optical microscope, further opto-electronics experiments based on

transient photocurrent and photo-CELIV can be implemented to study photogeneration electron/holes relaxation processes at microscopic scale in devices based on blends of nanoparticles/clusters in polymer-based devices. We believe that these two experiments could further enhance understanding of the materials.

Technical improvement:

Chapter 4 and 5 indicated the possibility of HCTE radiative recombination at the interface of inorganic ZnO layer and the organic polymer. The existing set-up can be improved by coupling a monochromator with luminescence detection port of the optical microscope and silicon APDs, and/or detector with higher sensitivity to the infra-red wavelengths ($\geq$ 1100) like InGaAs low-light detectors. Studying the double injection DiTC and the onset time of EL is achievable with the existing setup. This can give a better picture of where exactly is the origin of radiative recombination.

Sample configuration:

In Chapter 6, although there has been an attempt to distinguish the contribution of MoO_3 especially at the edges of the device using LBIC, the future attempt would be towards making a device with/without different layers in the same device. This can be achieved by wiping out part of the ZnO film (before annealing) and controlling the mask alignment in thermal vapour deposition system to deposit silver after depositing MoO_3. This ensures that the contribution of individual layers, spatial defects, edge effects and light-soak effects are consistent with the device recipe and photoexcitation intensities for any given device at a time.

Conceptual inconsistency:

In Section 5.2.1 showed inconsistency with respect to current understanding of the origin of open-circuit voltage (V_{oc}) and that measured V_{oc} was not equal to the expected difference in work function of cathode and the HOMO of the polymer, provided the Ag/MoO_3 forms an ohmic contact with all the three polymers tested. There is necessity to repeat the device fabrication and testing to probe the 'true' contact for of Ag with polymer.

Bibliography

[1] Michael Faraday. Experimental researches in electricity vol. 1, 1839.

[2] E Becquerel. On electron effects under the influence of solar radiation. *Comptes Rendues*, 9:561, 1839.

[3] W Smith. Photoconductive effect. *J. Soc. Telegraph Engineers*, 2:31, 1873.

[4] John Bardeen and Walter Hauser Brattain. The transistor, a semi-conductor triode. *Physical Review*, 74(2):230, 1948.

[5] William Shockley. The theory of p-n junctions in semiconductors and p-n junction transistors. *Bell Labs Technical Journal*, 28(3):435–489, 1949.

[6] Daryl M Chapin, CS Fuller, and GL Pearson. A new silicon p-n junction photocell for converting solar radiation into electrical power. *Journal of Applied Physics*, 25(5):676–677, 1954.

[7] Yugang Sun and John A Rogers. Inorganic semiconductors for flexible electronics. *Advanced materials*, 19(15):1897–1916, 2007.

[8] Sandro Lattante. Electron and hole transport layers: their use in inverted bulk heterojunction polymer solar cells. *Electronics*, 3(1):132–164, 2014.

[9] Peng Fei Bai, Robert A. Hayes, Ming Liang Jin, Ling Ling Shui, Zi Chuan Yi, L. Wang, Xiao Zhang, and Guo Fu Zhou. Review of paper-like display technologies. *Progree in Electromagnetics Research- pier*, 147:95–116, 2014.

[10] Barrett Comiskey, JD Albert, Hidekazu Yoshizawa, and Joseph Jacobson. An electrophoretic ink for all-printed reflective electronic displays. *Nature*, 394(6690):253, 1998.

[11] Claes G Granqvist. Electrochromics for smart windows: Oxide-based thin films and devices. *Thin Solid Films*, 564:1–38, 2014.

[12] N Thejo Kalyani and SJ Dhoble. Organic light emitting diodes: Energy saving lighting technologya review. *Renewable and Sustainable Energy Reviews*, 16(5):2696–2723, 2012.

[13] Simon Muench, Andreas Wild, Christian Friebe, Bernhard Häupler, Tobias Janoschka, and Ulrich S Schubert. Polymer-based organic batteries. *Chem. Rev*, 116(16):9438–9484, 2016.

[14] Leif Nyholm, Gustav Nyström, Albert Mihranyan, and Maria Strømme. Toward flexible polymer and paper-based energy storage devices. *Advanced Materials*, 23(33):3751–3769, 2011.

[15] Henning Sirringhaus. 25th anniversary article: Organic field-effect transistors: the path beyond amorphous silicon. *Advanced materials*, 26(9):1319–1335, 2014.

[16] Giuseppina Pace, Andrea Grimoldi, Marco Sampietro, Dario Natali, and Mario Caironi. Printed photodetectors. *Semiconductor Science and Technology*, 30(10):104006, 2015.

[17] Stephane Altazin, Raphael Clerc, Romain Gwoziecki, Jean-Marie Verilhac, Damien Boudinet, Georges Pananakakis, Gerard Ghibaudo, Isabelle Chartier, and Romain Coppard. Physics of the frequency response of rectifying organic schottky diodes. *Journal of Applied Physics*, 115(6):064509, 2014.

[18] Daniel T Simon, Sindhulakshmi Kurup, Karin C Larsson, Ryusuke Hori, Klas Tybrandt, Michel Goiny, Edwin WH Jager, Magnus Berggren, Barbara Canlon, and Agneta Richter-Dahlfors. Organic electronics for precise delivery of neurotransmitters to modulate mammalian sensory function. *Nature materials*, 8(9):742–746, 2009.

[19] Daniel T Simon, Erik O Gabrielsson, Klas Tybrandt, and Magnus Berggren. Organic bioelectronics: bridging the signaling gap between biology and technology. *Chemical Reviews*, 116(21):13009–13041, 2016.

[20] Dion Khodagholy, Jonathan Rivnay, Michele Sessolo, Moshe Gurfinkel, Pierre Leleux, Leslie H Jimison, Eleni Stavrinidou, Thierry Herve, Sébastien Sanaur, Róisín M Owens, et al. High transconductance organic electrochemical transistors. *Nature communications*, 4, 2013.

[21] Giuseppe Tarabella, Gaurav Nanda, Marco Villani, Nicola Coppedè, Roberto Mosca, George G Malliaras, Clara Santato, Salvatore Iannotta, and Fabio Cicoira. Organic electrochemical transistors monitoring micelle formation. *Chemical Science*, 3(12):3432–3435, 2012.

[22] Fabio Cicoira and Clara Santato. Organic light emitting field effect transistors: advances and perspectives. *Advanced Functional Materials*, 17(17):3421–3434, 2007.

[23] William R Mateker, Thomas Heumueller, Rongrong Cheacharoen, IT Sachs-Quintana, Michael D McGehee, Julien Warnan, Pierre M Beaujuge, Xiaofeng Liu, and Guillermo C Bazan. Molecular packing and arrangement govern the photo-oxidative stability of organic photovoltaic materials. *Chemistry of Materials*, 27(18):6345–6353, 2015.

[24] DD Eley. Phthalocyanines as semiconductors. *Nature*, 162(4125):819–819, 1948.

[25] Hideo Akamatu and Hiroo Inokuchi. On the electrical conductivity of violanthrone, iso-violanthrone, and pyranthrone. *The Journal of Chemical Physics*, 18(6):810–811, 1950.

[26] Hideo Akamatu, Hiroo Inokuchi, and Yoshio Matsunaga. Electrical conductivity of the perylene-bromine complex. *Nature*, 173:168–169, 1954.

[27] Murray A Lampert and Peter Mark. Current injection in solids. 1970.

[28] William R Salaneck, Kazuhiko Seki, Antoine Kahn, and Jean-Jacques Pireaux. *Conjugated Polymer and Molecular Interfaces: Science and Technology for Photonic and Optoelectronic Application*. CRC Press, 2001.

[29] Ching W Tang. Two-layer organic photovoltaic cell. *Applied Physics Letters*, 48:183, 1986.

[30] Gang Yu, Jun Gao, Jan C Hummelen, Fred Wudl, and Alan J Heeger. Polymer photovoltiac cells: Enhanced efficiencies via a network of internal donor-acceptor heterojunctions. *Science*, 270(5243):1789, 1995.

[31] Minh Trung Dang, Lionel Hirsch, and Guillaume Wantz. $P3HT : PCBM$, best seller in polymer photovoltaic research. *Advanced Materials*, 23(31):3597–3602, 2011.

[32] Feng Liu and Jean-Michel Nunzi. Enhanced organic light emitting diode and solar cell performances using silver nano-clusters. *Organic Electronics*, 13(9):1623–1632, 2012.

[33] Eva Bundgaard and Frederik C Krebs. Low band gap polymers for organic photovoltaics. *Solar Energy Materials and Solar Cells*, 91(11):954–985, 2007.

[34] Roland Schmechel and Heinz Von Seggern. Electronic traps in organic transport layers. *physica status solidi (a)*, 201(6):1215–1235, 2004.

[35] Haoyan Wei, L Scudiero, and Hergen Eilers. Infrared and photoelectron spectroscopy study of vapor phase deposited poly (3-hexylthiophene). *Applied Surface Science*, 255(20):8593–8597, 2009.

[36] WR Salaneck, O Inganäs, B Themans, JO Nilsson, B Sjögren, J-E Österholm, JL Brédas, and S Svensson. Thermochromism in poly (3-hexylthiophene) in the solid state: A spectroscopic study of temperature-dependent conformational defects. *The Journal of chemical physics*, 89(8):4613–4619, 1988.

[37] FJ Zhang, A Vollmer, J Zhang, Z Xu, JP Rabe, and N Koch. Energy level alignment and morphology of interfaces between molecular and polymeric organic semiconductors. *Organic Electronics*, 8(5):606–614, 2007.

[38] Ze-Lei Guan, Jong Bok Kim, He Wang, Cherno Jaye, Daniel A Fischer, Yueh-Lin Loo, and Antoine Kahn. Direct determination of the electronic structure of

the poly (3-hexylthiophene): phenyl-[6, 6]-c61 butyric acid methyl ester blend. *Organic Electronics*, 11(11):1779–1785, 2010.

[39] Carsten Deibel, Daniel Mack, Julien Gorenflot, Achim Schöll, Stefan Krause, Friedrich Reinert, Daniel Rauh, and Vladimir Dyakonov. Energetics of excited states in the conjugated polymer poly (3-hexylthiophene). *Physical Review B*, 81(8):085202, 2010.

[40] T Walter, R Herberholz, C Müller, and HW Schock. Determination of defect distributions from admittance measurements and application to cu (in, ga) se2 based heterojunctions. *Journal of Applied Physics*, 80(8):4411–4420, 1996.

[41] Tanvir Muntasir and Sumit Chaudhary. Understanding defect distributions in polythiophenes via comparison of regioregular and regiorandom species. *Journal of Applied Physics*, 118(20):205504, 2015.

[42] Pablo P Boix, Germà Garcia-Belmonte, Udane Muñecas, Marios Neophytou, Christoph Waldauf, and Roberto Pacios. Determination of gap defect states in organic bulk heterojunction solar cells from capacitance measurements. *Applied Physics Letters*, 95(23):317, 2009.

[43] Roderick CI MacKenzie, Chris G Shuttle, George F Dibb, Neil Treat, Elizabeth von Hauff, Maxwell J Robb, Craig J Hawker, Michael L Chabinyc, and Jenny Nelson. Interpreting the density of states extracted from organic solar cells using transient photocurrent measurements. *The Journal of Physical Chemistry C*, 117(24):12407–12414, 2013.

[44] Julia Schafferhans, Andreas Baumann, Carsten Deibel, and Vladimir Dyakonov. Trap distribution and the impact of oxygen-induced traps on the charge transport in poly (3-hexylthiophene). *Applied Physics Letters*, 93(9):093303, 2008.

[45] Michael J Travers, Daniel C Cowles, and G Barney Ellison. Reinvestigation of the electron affinities of o2 and no. *Chemical physics letters*, 164(5):449–455, 1989.

[46] Jing-Mei Zhuo, Li-Hong Zhao, Rui-Qi Png, Loke-Yuen Wong, Perq-Jon Chia, Jie-Cong Tang, Sankaran Sivaramakrishnan, Mi Zhou, Eric C-W Ou, Soo-Jin Chua, et al. Direct spectroscopic evidence for a photodoping mechanism in polythiophene and poly (bithiophene-alt-thienothiophene) organic semiconductor thin films involving oxygen and sorbed moisture. *Advanced materials*, 21(46):4747–4752, 2009.

[47] Raymond Bonnett. Photosensitizers of the porphyrin and phthalocyanine series for photodynamic therapy. *Chemical Society Reviews*, 24(1):19–33, 1995.

[48] H Hintz, H-J Egelhaaf, H Peisert, and T Chassé. Photo-oxidation and ozonization of poly (3-hexylthiophene) thin films as studied by uv/vis and photoelectron spectroscopy. *Polymer Degradation and Stability*, 95(5):818–825, 2010.

[49] Mohamed SA Abdou, Francesco P Orfino, Yongkeun Son, and Steven Holdcroft. Interaction of oxygen with conjugated polymers: charge transfer complex formation with poly (3-alkylthiophenes). *Journal of the American Chemical Society*, 119(19):4518–4524, 1997.

[50] Andreas Sperlich, Hannes Kraus, Carsten Deibel, Hubert Blok, Jan Schmidt, and Vladimir Dyakonov. Reversible and irreversible interactions of poly (3-hexylthiophene) with oxygen studied by spin-sensitive methods. *The Journal of Physical Chemistry B*, 115(46):13513–13518, 2011.

[51] Matthieu Manceau, Agnès Rivaton, Jean-Luc Gardette, Stéphane Guillerez, and Noëlla Lemaître. The mechanism of photo-and thermooxidation of poly (3-hexylthiophene)(p3ht) reconsidered. *Polymer Degradation and Stability*, 94(6):898–907, 2009.

[52] PG Le Comber and WE Spear. Electronic transport in amorphous silicon films. *Physical Review Letters*, 25(8):509, 1970.

[53] H Bässler. Charge transport in disordered organic photoconductors a monte carlo simulation study. *physica status solidi (b)*, 175(1):15–56, 1993.

[54] Vinay Ambegaokar, BI Halperin, and JS Langer. Hopping conductivity in disordered systems. *Physical Review B*, 4(8):2612, 1971.

[55] Hagen Klauk. *Organic electronics II: more materials and applications*, volume 2. John Wiley & Sons, 2012.

[56] GAH Wetzelaer and Paul WM Blom. Ohmic current in organic metal-insulator-metal diodes revisited. *Physical Review B*, 89(24):241201, 2014.

[57] P De Bruyn, AHP Van Rest, GAH Wetzelaer, Dago M de Leeuw, and Paul WM Blom. Diffusion-limited current in organic metal-insulator-metal diodes. *Physical review letters*, 111(18):186801, 2013.

[58] J Steiger, R Schmechel, and H Von Seggern. Energetic trap distributions in organic semiconductors. *Synthetic metals*, 129(1):1–7, 2002.

[59] PN Murgatroyd. Theory of space-charge-limited current enhanced by frenkel effect. *Journal of Physics D Applied Physics*, 3(2):151, 1970.

[60] Murray A Lampert and A Rose. Volume-controlled, two-carrier currents in solids: The injected plasma case. *Physical Review*, 121(1):26, 1961.

[61] Y Roichman and N Tessler. Charge transport in conjugated polymers: The influence of charge concentration. *Synthetic metals*, 135:443–444, 2003.

[62] C Tanase, PWM Blom, and DM De Leeuw. Origin of the enhanced space-charge-limited current in poly (p-phenylene vinylene). *Physical Review B*, 70(19):193202, 2004.

[63] WF Pasveer, Jeroen Cottaar, C Tanase, Reinder Coehoorn, PA Bobbert, PWM Blom, DM De Leeuw, and MAJ Michels. Unified description of charge-carrier mobilities in disordered semiconducting polymers. *Physical review letters*, 94(20):206601, 2005.

[64] Robert H Parmenter and Wolfgang Ruppel. Two-carrier space-charge-limited current in a trap-free insulator. *Journal of Applied Physics*, 30(10):1548–1558, 1959.

[65] Carsten Deibel and Vladimir Dyakonov. Polymer-fullerene bulk heterojunction solar cells. *Reports on Progress in Physics*, 73(9):096401, 2010.

[66] Nicolas Blouin, Alexandre Michaud, and Mario Leclerc. A low-bandgap poly (2, 7-carbazole) derivative for use in high-performance solar cells. *Advanced Materials*, 19(17):2295–2300, 2007.

[67] Mikkel Jørgensen, Kion Norrman, Suren A Gevorgyan, Thomas Tromholt, Birgitta Andreasen, and Frederik C Krebs. Stability of polymer solar cells. *Advanced materials*, 24(5):580–612, 2012.

[68] Alexander Wagenpfahl, Daniel Rauh, Moritz Binder, Carsten Deibel, and Vladimir Dyakonov. S-shaped current-voltage characteristics of organic solar devices. *Physical Review B*, 82(11):115306, 2010.

[69] Benjamin Y Finck and Benjamin J Schwartz. Understanding the origin of the s-curve in conjugated polymer/fullerene photovoltaics from drift-diffusion simulations. *Applied Physics Letters*, 103(5):053306, 2013.

[70] Wolfgang Tress, Annette Petrich, Markus Hummert, Moritz Hein, Karl Leo, and Moritz Riede. Imbalanced mobilities causing s-shaped iv curves in planar heterojunction organic solar cells. *Applied Physics Letters*, 98(6):23, 2011.

[71] Bertrand Tremolet de Villers, Christopher J Tassone, Sarah H Tolbert, and Benjamin J Schwartz. Improving the reproducibility of p3ht: Pcbm solar cells by controlling the pcbm/cathode interface. *The Journal of Physical Chemistry C*, 113(44):18978–18982, 2009.

[72] Anton Sundqvist, Oskar J Sandberg, Mathias Nyman, Jan-Henrik Smått, and Ronald Österbacka. Origin of the s-shaped jv curve and the light-soaking issue in inverted organic solar cells. *Advanced Energy Materials*, 2016.

[73] Thomas Kirchartz, Bart E Pieters, James Kirkpatrick, Uwe Rau, and Jenny Nelson. Recombination via tail states in polythiophene: fullerene solar cells. *Physical Review B*, 83(11):115209, 2011.

[74] Andrea Maurano, Chris G Shuttle, Rick Hamilton, Amy M Ballantyne, Jenny Nelson, Weimin Zhang, Martin Heeney, and James R Durrant. Transient opto-electronic analysis of charge carrier losses in a selenophene/fullerene blend solar cell. *The Journal of Physical Chemistry C*, 115(13):5947–5957, 2011.

[75] Dan Credgington, Fiona C Jamieson, Bright Walker, Thuc-Quyen Nguyen, and James R Durrant. Quantification of geminate and non-geminate recombination losses within a solution-processed small-molecule bulk heterojunction solar cell. *Advanced Materials*, 24(16):2135–2141, 2012.

[76] In-Wook Hwang, Jin Young Kim, Shinuk Cho, Jonathan Yuen, Nelson Coates, Kwanghee Lee, Martin Heeney, Iain McCulloch, Daniel Moses, and AJ Heeger. Bulk heterojunction materials composed of poly (2, 5-bis (3-tetradecylthiophen-2-yl) thieno [3, 2-b] thiophene): Ultrafast electron transfer and carrier recombination. *The Journal of Physical Chemistry C*, 112(21):7853–7857, 2008.

[77] Yu Xie, Yong Li, Lixin Xiao, Qiquan Qiao, Rabin Dhakal, Zhiling Zhang, Qihuang Gong, David Galipeau, and Xingzhong Yan. Femtosecond time-resolved fluorescence study of p3ht/pcbm blend films. *The Journal of Physical Chemistry C*, 114(34):14590–14600, 2010.

[78] Jorge Piris, Tieneke E Dykstra, Artem A Bakulin, Paul HM van Loosdrecht, Walter Knulst, M Tuan Trinh, Juleon M Schins, and Laurens DA Siebbeles.

Photogeneration and ultrafast dynamics of excitons and charges in p3ht/pcbm blends. *The Journal of Physical Chemistry C*, 113(32):14500–14506, 2009.

[79] Hideo Ohkita, Steffan Cook, Yeni Astuti, Warren Duffy, Steve Tierney, Weimin Zhang, Martin Heeney, Iain McCulloch, Jenny Nelson, Donal DC Bradley, et al. Charge carrier formation in polythiophene/fullerene blend films studied by transient absorption spectroscopy. *Journal of the American Chemical Society*, 130(10):3030–3042, 2008.

[80] G Juška, K Arlauskas, M Viliūnas, and J Kočka. Extraction current transients: new method of study of charge transport in microcrystalline silicon. *Physical review letters*, 84(21):4946, 2000.

[81] Ian H Campbell, John P Ferraris, Thomas W Hagler, Michael D Joswick, Ian D Parker, and Darryl L Smith. Measuring internal electric fields in organic light-emitting diodes using electroabsorption spectroscopy. *Polymers for Advanced Technologies*, 8(7):417–423, 1997.

[82] GG Malliaras, JR Salem, PJ Brock, and JC Scott. Photovoltaic measurement of the built-in potential in organic light emitting diodes and photodiodes. *Journal of Applied Physics*, 84(3):1583–1587, 1998.

[83] Biswajit Ray, Aditya G Baradwaj, Bryan W Boudouris, and Muhammad A Alam. Defect characterization in organic semiconductors by forward bias capacitance–voltage (fb-cv) analysis. *The Journal of Physical Chemistry C*, 118(31):17461–17466, 2014.

[84] Christoph J Brabec, Antonio Cravino, Dieter Meissner, N Serdar Sariciftci, Thomas Fromherz, Minze T Rispens, Luis Sanchez, Jan C Hummelen, et al. Origin of the open circuit voltage of plastic solar cells. *Advanced Functional Materials*, 11(5):374–380, 2001.

[85] VD Mihailetchi, PWM Blom, JC Hummelen, and MT Rispens. Cathode dependence of the open-circuit voltage of polymer: fullerene bulk heterojunction solar cells. *Journal of Applied Physics*, 94(10):6849–6854, 2003.

[86] James C Blakesley and Dieter Neher. Relationship between energetic disorder and open-circuit voltage in bulk heterojunction organic solar cells. *Physical Review B*, 84(7):075210, 2011.

[87] Germa Garcia-Belmonte, Pablo P Boix, Juan Bisquert, Martijn Lenes, Henk J Bolink, Andrea La Rosa, Salvatore Filippone, and Nazario Martín. Influence of the intermediate density-of-states occupancy on open-circuit voltage of bulk heterojunction solar cells with different fullerene acceptors. *The Journal of Physical Chemistry Letters*, 1(17):2566–2571, 2010.

[88] EH Rhoderick. Metal-semiconductor contacts. *IEE Proceedings I Communications, Speech and Vision [see also IEE Proceedings-Communications]*, 1(129):1, 1982.

[89] H Ishii, N Hayashi, E Ito, Y Washizu, K Sugi, Y Kimura, M Niwano, Y Ouchi, and K Seki. Kelvin probe study of band bending at organic semiconductor metal interfaces: examination of fermi level alignment. *Physica status solidi (a)*, 201(6):1075–1094, 2004.

[90] Raymond T Tung and . The physics and chemistry of the schottky barrier height. *Applied Physics Reviews*, 1(1):011304, 2014.

[91] Slawomir Braun, William R Salaneck, and Mats Fahlman. Energy-level alignment at organic/metal and organic/organic interfaces. *Advanced Materials*, 21(14-15):1450–1472, 2009.

[92] Yinhua Zhou, Canek Fuentes-Hernandez, Jaewon Shim, Jens Meyer, Anthony J Giordano, Hong Li, Paul Winget, Theodoros Papadopoulos, Hyeunseok Cheun, Jungbae Kim, et al. A universal method to produce low–work function electrodes for organic electronics. *Science*, 336(6079):327–332, 2012.

[93] Kenji Nomura, Hiromichi Ohta, Akihiro Takagi, Toshio Kamiya, Masahiro Hirano, and Hideo Hosono. Room-temperature fabrication of transparent flexible thin-film transistors using amorphous oxide semiconductors. *Nature*, 432(7016):488–492, 2004.

[94] Xinge Yu, Tobin J Marks, and Antonio Facchetti. Metal oxides for optoelectronic applications. *Nature materials*, 15(4):383–396, 2016.

[95] Anderson Janotti and Chris G Van de Walle. Hydrogen multicentre bonds. *Nature materials*, 6(1):44–47, 2007.

[96] Fumiyasu Oba, Atsushi Togo, Isao Tanaka, Joachim Paier, and Georg Kresse. Defect energetics in zno: A hybrid hartree-fock density functional study. *Physical Review B*, 77(24):245202, 2008.

[97] Hyeunseok Cheun, Canek Fuentes-Hernandez, Yinhua Zhou, William J Potscavage Jr, Sung-Jin Kim, Jaewon Shim, Amir Dindar, and Bernard Kippelen. Electrical and optical properties of zno processed by atomic layer deposition in inverted polymer solar cells. *The Journal of Physical Chemistry C*, 114(48):20713–20718, 2010.

[98] QH Li, T Gao, YG Wang, and TH Wang. Adsorption and desorption of oxygen probed from zno nanowire films by photocurrent measurements. *Applied Physics Letters*, 86(12):123117, 2005.

[99] Donald A Melnick. Zinc oxide photoconduction, an oxygen adsorption process. *The Journal of Chemical Physics*, 26(5):1136–1146, 1957.

[100] Andrea Maurano, Chris G Shuttle, Rick Hamilton, Amy M Ballantyne, Jenny Nelson, Weimin Zhang, Martin Heeney, and James R Durrant. Transient optoelectronic analysis of charge carrier losses in a selenophene/fullerene blend solar cell. *The Journal of Physical Chemistry C*, 115(13):5947–5957, 2011.

[101] Steffan Cook, Akihiro Furube, and Ryuzi Katoh. Analysis of the excited states of regioregular polythiophene p3ht. *Energy & Environmental Science*, 1(2):294–299, 2008.

[102] Ying W Soon, Hoduk Cho, Jonathan Low, Hugo Bronstein, Iain McCulloch, and James R Durrant. Correlating triplet yield, singlet oxygen generation and photochemical stability in polymer/fullerene blend films. *Chemical Communications*, 49(13):1291–1293, 2013.

[103] VI Arkhipov and H Bässler. Exciton dissociation and charge photogeneration in pristine and doped conjugated polymers. *physica status solidi (a)*, 201(6):1152–1187, 2004.

[104] Martin M Perlman. Thermally stimulated currents and voltages and dielectric properties. *Journal of The Electrochemical Society*, 119(7):892–898, 1972.

[105] Masashi OHYAMA, Hiromitsu KOZUKA, and Sumio SAKKA. Preparation of zno films with preferential orientation by sol-gel method. *Journal of the ceramic society of Japan*, 104(1208):296–300, 1996.

[106] Nadia Grossiord, Jan M Kroon, Ronn Andriessen, and Paul WM Blom. Degradation mechanisms in organic photovoltaic devices. *Organic Electronics*, 13(3):432–456, 2012.

[107] Matthieu Manceau, Agnès Rivaton, Jean-Luc Gardette, Stéphane Guillerez, and Noëlla Lemaître. Light-induced degradation of the p3ht-based solar cells active layer. *Solar Energy Materials and Solar Cells*, 95(5):1315–1325, 2011.

[108] Kwang Ho Lee, Ho Won Jang, Ki-Beom Kim, Yoon-Heung Tak, and Jong-Lam Lee. Mechanism for the increase of indium-tin-oxide work function by o 2 inductively coupled plasma treatment. *Journal of Applied Physics*, 95(2):586–590, 2004.

[109] R Schlaf, H Murata, and ZH Kafafi. Work function measurements on indium tin oxide films. *Journal of Electron Spectroscopy and Related Phenomena*, 120(1):149–154, 2001.

[110] Maria Vasilopoulou, Anastasia Soultati, Panagiotis Argitis, Thomas Stergiopoulos, and Dimitris Davazoglou. Fast recovery of the high work function of tungsten and molybdenum oxides via microwave exposure for efficient organic photovoltaics. *The journal of physical chemistry letters*, 5(11):1871–1879, 2014.

[111] Irfan, Huanjun Ding, Yongli Gao, Cephas Small, Do Young Kim, Jegadesan Subbiah, and Franky So. Energy level evolution of air and oxygen exposed molybdenum trioxide films. *Applied Physics Letters*, 96(24):116, 2010.

[112] Irfan Irfan, Alexander James Turinske, Zhenan Bao, and Yongli Gao. Work function recovery of air exposed molybdenum oxide thin films. *Applied Physics Letters*, 101(9):093305, 2012.

[113] Valentin D Mihailetchi, HX Xie, Bert de Boer, LJ Anton Koster, and Paul WM Blom. Charge transport and photocurrent generation in poly (3-hexylthiophene): methanofullerene bulk-heterojunction solar cells. *Advanced Functional Materials*, 16(5):699–708, 2006.

[114] Peter Capper, Safa Kasap, Arthur Willoughby, Cole W Litton, Thomas C Collins, and Donald C Reynolds. *Zinc oxide materials for electronic and optoelectronic device applications*. John Wiley & Sons, 2011.

[115] Anderson Janotti and Chris G Van de Walle. Fundamentals of zinc oxide as a semiconductor. *Reports on Progress in Physics*, 72(12):126501, 2009.

[116] Cheng Li, Yana Vaynzof, Girish Lakhwani, Gareth J Beirne, Jianpu Wang, and Neil C Greenham. Observation of oxygen vacancy migration in memory devices based on zno nanoparticles. *Journal of Applied Physics*, 121(14):144503, 2017.

[117] J Joshua Yang, Matthew D Pickett, Xuema Li, Douglas AA Ohlberg, Duncan R Stewart, and R Stanley Williams. Memristive switching mechanism for metal/oxide/metal nanodevices. *Nature nanotechnology*, 3(7):429–433, 2008.

[118] Dmitri B Strukov, Gregory S Snider, Duncan R Stewart, and R Stanley Williams. The missing memristor found. *nature*, 453(7191):80, 2008.

[119] DH Zhang. Adsorption and photodesorption of oxygen on the surface and crystallite interfaces of sputtered zno films. *Materials Chemistry and Physics*, 45(3):248–252, 1996.

[120] Y Shapira, SM Cox, and David Lichtman. Chemisorption, photodesorption and conductivity measurements on zno surfaces. *Surface Science*, 54(1):43–59, 1976.

[121] Anurag Panda, C Kyle Renshaw, Ardavan Oskooi, Kyusang Lee, and Stephen R Forrest. Excited state and charge dynamics of hybrid organic/inorganic heterojunctions. ii. experiment. *Physical Review B*, 90(4):045303, 2014.

[122] C Kyle Renshaw and Stephen R Forrest. Excited state and charge dynamics of hybrid organic/inorganic heterojunctions. i. theory. *Physical Review B*, 90(4):045302, 2014.

[123] M Eyer, S Sadofev, J Puls, and S Blumstengel. Charge transfer excitons at znmgo/p3ht heterojunctions: Relation to photovoltaic performance. *Applied Physics Letters*, 107(22):221602, 2015.

[124] Andrea Seemann, Tobias Sauermann, Christoph Lungenschmied, Oskar Armbruster, Siegfried Bauer, H-J Egelhaaf, and Jens Hauch. Reversible and irreversible degradation of organic solar cell performance by oxygen. *Solar Energy*, 85(6):1238–1249, 2011.

[125] Zivayi Chiguvare, Jürgen Parisi, and Vladimir Dyakonov. Influence of thermal annealing on the electrical properties of poly (3-hexylthiophene)-based thin film diodes. *Zeitschrift für Naturforschung A*, 62(10-11):609–619, 2007.

[126] Junghwan Kim, Geunjin Kim, Youna Choi, Jongjin Lee, Sung Heum Park, and Kwanghee Lee. Light-soaking issue in polymer solar cells: Photoinduced energy level alignment at the sol-gel processed metal oxide and indium tin oxide interface. *Journal of Applied Physics*, 111(11):114511, 2012.

[127] Dahvyd Wing, Avner Rothschild, and Nir Tessler. Schottky barrier height switching in thin metal oxide films studied in diode and solar cell device configurations. *Journal of Applied Physics*, 118(5):054501, 2015.

[128] Cheahli Leow, Takashi Harada, Toshihiro Ohnishi, and Michio Matsumura. Light-soaking effects on zno-nanorods/polymer hybrid photovoltaics. *RSC Advances*, 5(29):22647–22653, 2015.

[129] Markus C Scharber, David Mühlbacher, Markus Koppe, Patrick Denk, Christoph Waldauf, Alan J Heeger, and Christoph J Brabec. Design rules for donors in bulk-heterojunction solar cellstowards 10% energy-conversion efficiency. *Advanced materials*, 18(6):789–794, 2006.

[130] Salem Wakim, Serge Beaupré, Nicolas Blouin, Badrou-Réda Aich, Sheila Rodman, Russell Gaudiana, Ye Tao, and Mario Leclerc. Highly efficient organic solar cells based on a poly (2, 7-carbazole) derivative. *Journal of Materials Chemistry*, 19(30):5351–5358, 2009.

[131] C Jiang, RR Lunt, PM Duxbury, and PP Zhang. High-performance inverted solar cells with a controlled zno buffer layer. *RSC Advances*, 4(7):3604–3610, 2014.

[132] HCF Martens, HB Brom, and PWM Blom. Frequency-dependent electrical response of holes in poly (p-phenylene vinylene). *Physical Review B*, 60(12):R8489, 1999.

[133] Michael Kröger, Sami Hamwi, Jens Meyer, Thomas Riedl, Wolfgang Kowalsky, and Antoine Kahn. P-type doping of organic wide band gap materials by transition metal oxides: A case-study on molybdenum trioxide. *Organic Electronics*, 10(5):932–938, 2009.

[134] Sylvain Chambon, Lionel Derue, Michel Lahaye, Bertrand Pavageau, Lionel Hirsch, and Guillaume Wantz. Moo3 thickness, thermal annealing and solvent annealing effects on inverted and direct polymer photovoltaic solar cells. *Materials*, 5(12):2521–2536, 2012.

[135] Mathias Nyman, Staffan Dahlström, Oskar J Sandberg, and Ronald Österbacka. Unintentional bulk doping of polymer-fullerene blends from a thin interfacial layer of moo3. *Advanced Energy Materials*, 6(15), 2016.

[136] Mark T Greiner, Lily Chai, Michael G Helander, Wing-Man Tang, and Zheng-Hong Lu. Metal/metal-oxide interfaces: how metal contacts affect the work function and band structure of moo3. *Advanced Functional Materials*, 23(2):215–226, 2013.

[137] Roland Rösch, David M Tanenbaum, Mikkel Jørgensen, Marco Seeland, Maik Bärenklau, Martin Hermenau, Eszter Voroshazi, Matthew T Lloyd, Yulia Galagan, Birger Zimmermann, et al. Investigation of the degradation mechanisms of a variety of organic photovoltaic devices by combination of imaging techniquesthe isos-3 inter-laboratory collaboration. *Energy & Environmental Science*, 5(4):6521–6540, 2012.

[138] Krishna Feron, Timothy J Nagle, Lynn J Rozanski, Bill B Gong, and Christopher J Fell. Spatially resolved photocurrent measurements of organic solar cells: tracking water ingress at edges and pinholes. *Solar Energy Materials and Solar Cells*, 109:169–177, 2013.

Appendix A

A.1 Absorption Spectra of zinc oxide film

Figure A.1 shows the absorption spectra of ZnO thin film on a glass substrate annealed at 180℃for 15 minutes in air. The typical band gap of $\sim 3.2eV$ for ZnO thin film is obvious from the absorption edge onset at $\sim 388nm$.

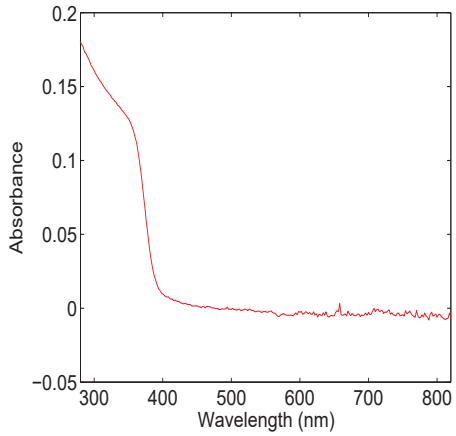

Figure A.1: Absorption spectra of ZnO spin-coated on top of glass substrate and annealed at 180℃for 15 minutes in air.

A.2 AFM scan of ZnO surface

Figure A.2 shows the topography of a ZnO layer on top of ITO substrate annealed at 180℃for the same 15 minutes measuring an average roughness, $R_a \sim 9nm$. The film thickness was measured to be about (40-50) nm using Dektek profilometer.

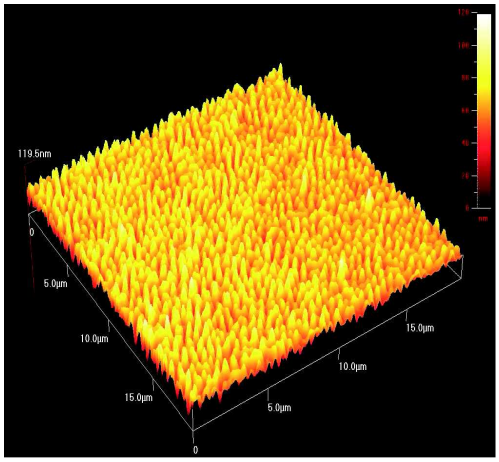

Figure A.2: AFM scan of ZnO layer spin-coated on top of ITO(on glass) substrate and annealed at 180℃for 15 minutes.

A.3 Incident Photo-to-Current Efficiency

Figure A.3 shows the Incident Photon-to-Current Efficiency (IPCE) of the P3HT-based devices with and without ZnO layer and the absorption spectra of thin films of P3HT with ZnO and without ZnO layer on a glass substrate are also shown. ZnO aids in extracting higher photocurrent by collecting the electrons from the conduction band while blocking the holes from valence band of the polymer reaching the cathode. The photocurrent peak seen at about 370 nm is due to the electron-hole pairs generated in ZnO layer.

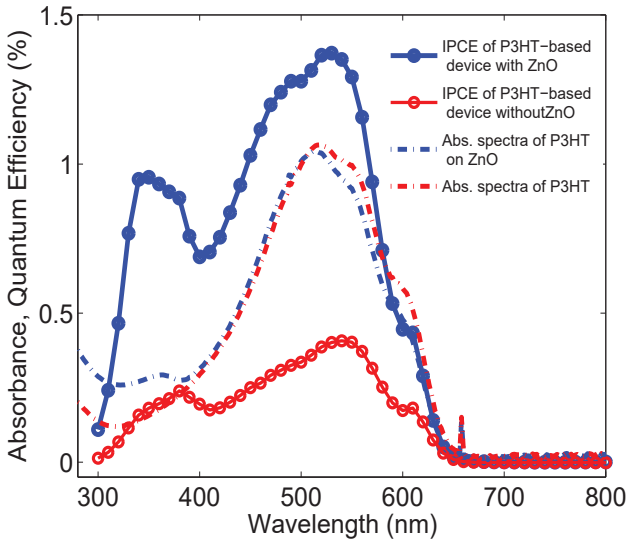

Figure A.3: Incident photon to current conversion efficiency of the P3HT-based devices with and without ZnO layer and their absorption spectra.

Appendix B

B.1 Mobility from Space-Charge limited current

In order to extract the effective mobility of the charges from the space-charge limited current regime of the current-voltage characteristics, the characteristics are visually checked for a constant slope behaviour in linear J-V characteristics and/or for depressing behaviour in a logJ-logV characteristics. The former can be graphically tested by plotting the resistance measured at each voltage bias, as shown in figure B.1(a) in the case of P3HT-based device. There was a continous decrease in the resistance with the forward bias applied infering that the J-V characteristics were not limited by the series resistance, (R_s), at least in the currents of our interest. Therefore the series resistance was not included in the data analysis. Figure B.1(b) shows an example of R_s correction applied on the one of the data sets and the effect of incorrect deduction of voltage drop due to larger R_s is visible in the form of concaving upwards of the IV characteristics. Similar tests were done on MDMO:PPV and PCDTBT based devices.

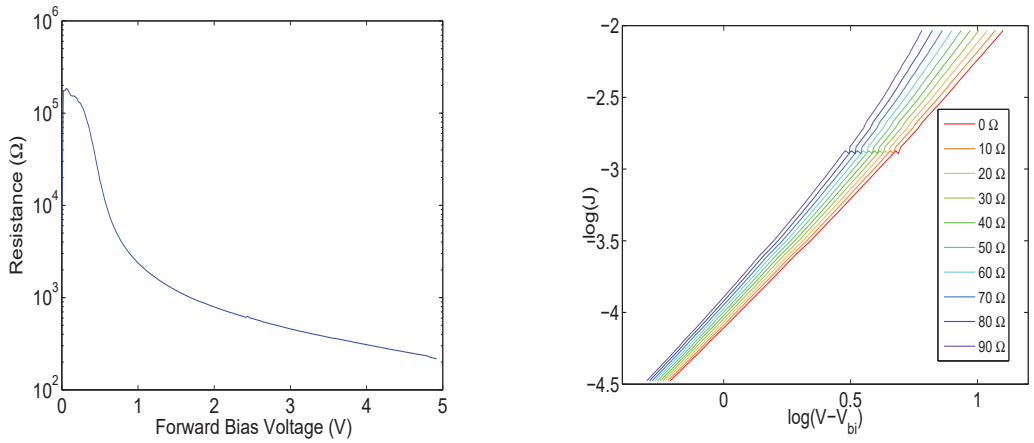

(a) (b)

Figure B.1: a) Resistance vs forward bias voltage for a P3HT-based device, b) Effect of subtracting the voltage loss due to series resistance in the device on the I-V characteristics of a P3HT-based device with a fixed $V_{bi} = 450mV$.

The data is plotted on a log-log scale in order to identify the SCLC regime. The V_{bi} is estimated from the fermi level of the ITO/ZnO and HOMO of the polymer in use, shown in the table[]. As the V_{bi} is not known precisely, it was decided to sweep discrete V_{bi} to be subtracted from the bias voltage before plotting the log-log of current and voltage, as shown in Figure B.2. Only those data sets of corrected biases were considered, for which the Current(I) values did not deviate by 3-4 folds with respect to those of uncorrected data set i.e. for which $V_{bi} = 0$. The chosen data sets were given regression fit using the linear equation (B.1a) assuming the charge mobility is field-independent. Matlab functions **polyfit** and **lsqcurvefit** were used for the fits.

$$log(J) = C + mlog(V - V_{bi}) \tag{B.1a}$$

$$log(J) = log(\frac{9}{8}\frac{\epsilon_0\epsilon_r\mu}{L^3}) + 2log(V - V_{bi}) \tag{B.1b}$$

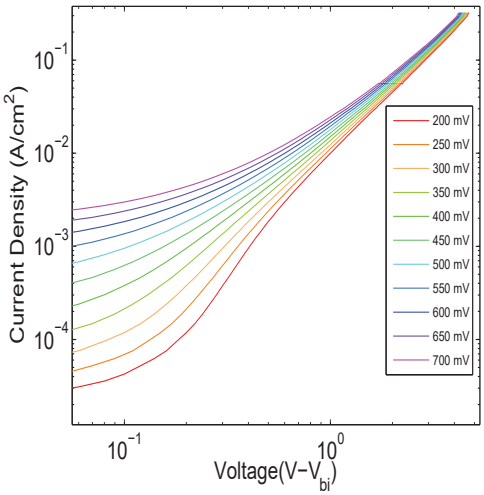

Figure B.2: Current-Voltage characteristics in logarithmic scale with built-in voltage varied between 200 mV to 700 mV in the steps of 50 mV.

For the specific cases where it seemed that current increased faster than the trend of V^2, with no correction of voltage drop due to R_s, exponential dependence of mobility on the electric field was considered as a model fit. The parameters m and C extracted from the regression fit were used as initial guesses to fit the same data using Murgatroyd's model of SCLC. For pristine and encapsulated devices that were studied in this work, it was a simple SCLC trend. A unique case that seemed to follow the trend of Murgatroyd's model was aged(tested after 1 year from the date of device fabrication) and unencapsulated $ITO/ZnO/P3HT/MoO_3/Ag$ device, whose characteristics are shown in Figure B.3.

$$J \simeq (9/8)\epsilon\mu_0(V - V_{bi})^2 exp(0.89\sqrt{((V - V_{bi})/E_0 L)}))/L^3 \tag{B.2}$$

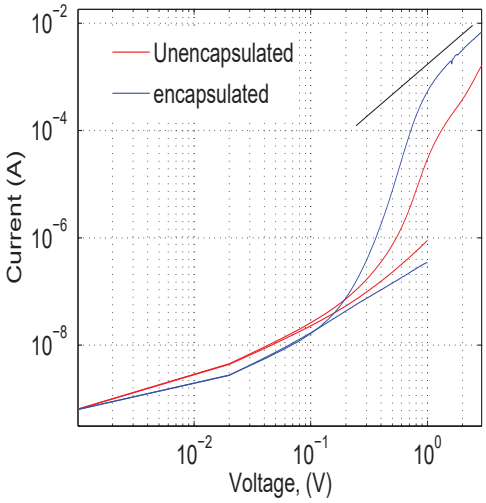

Figure B.3: Current-Voltage characteristics of an encapped and unencapsulated P3HT-based device tested after 1 year, while the devices were stored in ambient but dark conditions. The black line is visual aid of slope equal to 2, the SCLC regime.

Appendix C

C.1 Charge mobility from CELIV

Figure C.1(a) shows the CELIV signal off of P3HT-based device, where the discrete color gradient from red to violet curves are for increasing initial bias offsets. Figure C.1(b) shows the charges extracted out of the device, by integrating the area under the curve, but above the displacement current. The charge mobility is calculated semi-empirically, using Equation 2.15d, for various initial bias voltages. For increasing levels of initial bias voltages, there is an increasing density of charges injected(extracted) out the CELIV ramp signal. Figure C.1(c) shows a trend of decreasing mobility that varied by an order with the increase in charge density injected(& extracted) in(& out of) the device. The equation for mobility calculation does not show any dependence on the charge density, and hence it is not clear if there is an actual phenomenological decrease in the mobility or the shift in CELIV peak is just the result of convolution of many such peaks. The mobility calculation, which is sensitive to only the CELIV peak position, is obscured by the flattening of the CELIV peak with the increasing offset voltage as well. For a polymer like P3HT that has relatively higher conductivity, it is hard to locate the peak position, especially at lower offset voltage, which means the calculated mobilities are possibly underestimated.

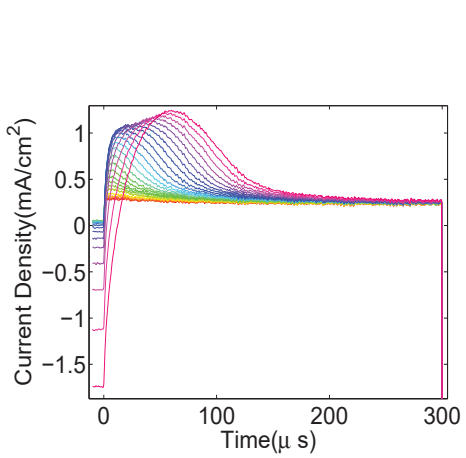

(a)

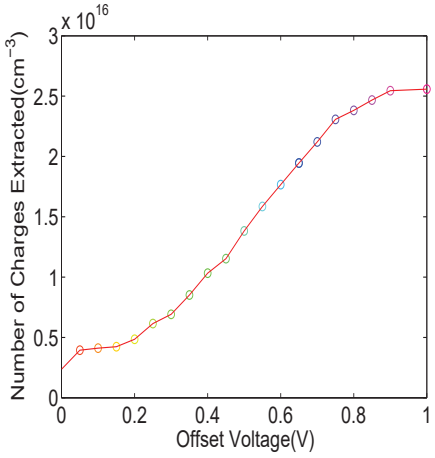

(b)

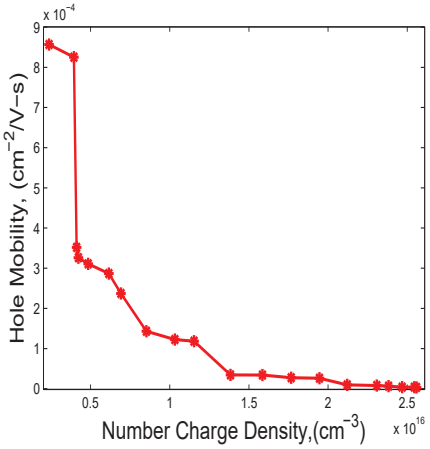

(c)

Figure C.1: a) Current dynamics of CELIV output from a P3HT-based device for an increasing initial offset voltage going from red to violet color, b) Charge extracted of each initial offset voltage, c) Semi-empirical calculation of charge mobility from the cELIV peak position.

Appendix D

D.1 Photo- and Electroluminescence Spectra

Figure D.1(a) shows normalized photoluminescence (PL) spectra of the three polymers P3HT, MDMO:PPV and PCDTBT. The excitation spot was chosen right in the middle of the device using optical microscope. The optical excitation and emission was performed from the ITO side of the device. The excitation wavelength was 405nm for all the tests. Figure D.1(b) shows the normalized electroluminescence (EL) spectra measured at 3V bias to the device, along with it PL spectra to indicate that the observed EL is a direct result of efficient injection of charges into the active medium. While the P3HT and MDMO:PPV based devices showed increased EL (not shown here) after UV light soak, they were not as intense as PCDTBT-based devices and hence were only detectable using avalanche detectors.

D.2 Lamps Spectra

The light sources used for the light-soaking experiments were tested with both halogen lamp and mercury arc lamp, and their correponding emission spectra as shown in the Figure D.2. The halogen lamp was chosen for low intensity test, whereas the arc lamp for higher intensity tests. The lamps were coupled into the microscope past a

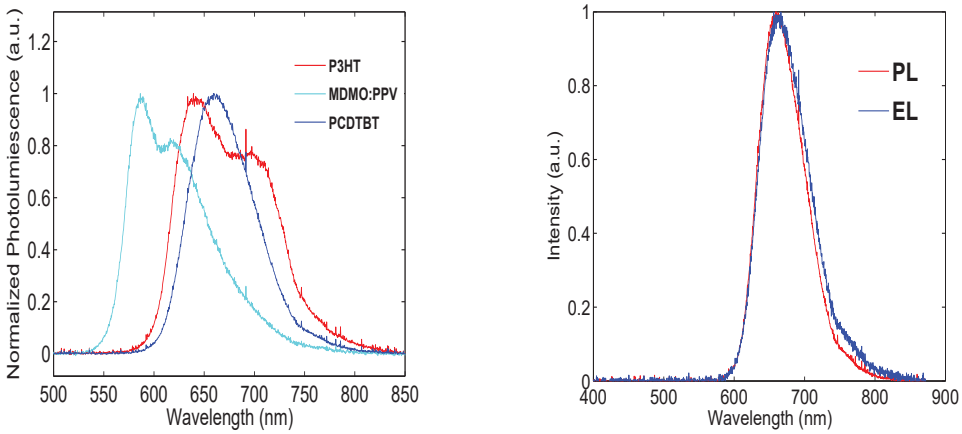

(a) (b)

Figure D.1: a) Normalized photoluminescence of the polymers in a device configuration, b) Normalized electro and photoluminescence of PCDTBT-based device.

bandpass filter (300-900)nm.

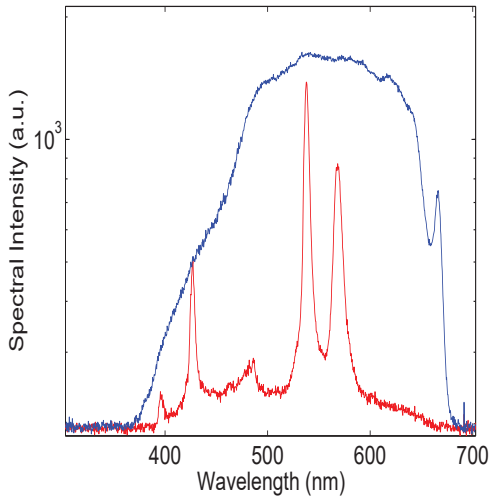

Figure D.2: Optical spectra of the Lamps used to soak the devices. The red curve correponds to Hg Arc lamp and the blue curve is halogen lamp spectra.

UNIVERSITE BRETAGNE LOIRE

université angers

Thèse de Doctorat

Sanyasi Rao Bobbara

Effect of Encapsulation and Light-soak on Charge Transport Properties in Organic Semiconductor-based Diodes

Résumé

Les semiconducteurs organiques (SO) ont attiré une grande attention ces dernières années en raison de leur facilité de fabrication, de leurs modifications des propriétés optiques et électriques et de leur rentabilité. Ils forment la classe de matériaux les plus adaptés à l'électronique flexible et à la bioélectronique, en particulier en association avec des matériaux inorganiques / hybrides solubles en solution. Cependant, la mobilité des charges dans ces matériaux est fortement affectés par leur désordre structurel et énergétique introduit par les défauts qui "piègent" les transporteurs de charge. Selon l'emplacement physique des pièges et leur distribution en énergie, ils pourraient affecter de manière significative le transport de charge dans un dispositif. Le présent travail s'efforce de sonder l'interface et les états défectueux en masse dans des diodes à base de polymère. Au lieu de cela, une partie de l'étude implique de caractériser le système avec et sans encapsulation, en utilisant des techniques pour enregistrer le comportement de courant-tension à l'état stationnaire (IV), les transitoires d'extraction de charge par la tension augmentant linéairement (CELIV) et les courants transitoires d'injection en obscurité (DiTC), ainsi que la photoluminescence (PL) et l'électroluminescence (EL) des systèmes. Les mêmes caractéristiques ont été effectuées pour observer l'effet de pénétration de la lumière ultraviolet (UV) sur les systèmes. Tous les tests ont été effectués sur trois polymères différents, à savoir P3HT, MDMO:PPV et PCDTBT. La comparaison des dispositifs encapsulés et non encapsulés donne un aperçu des différences caractéristiques des mesurables lors de l'exposition à l'air et humidité. Les tests de pénétration lumineuse indiquent la modification de la fonction de travail de la cathode après une désorption d'oxygène assistée par UV sur l'interface polymère/cathode. Un effort simultané s'est traduit par une étude in situ de la dynamique de transport des charges dans les semi-conducteurs organiques sur une large gamme de temps à une échelle microscopique.

Mots clés
Cellule solaire organique, transport de charges, encapsulation

Abstract

Organic semiconductors (OSs) have garnered a great attention in the recent years due to their ease of processibility, optical and electrical property-tunability, and to their cost-effectiveness. They form the class of materials most suitable for flexible electronics and bioelectronics, especially in association with solution-processable inorganic/hybrid materials. However, the charge mobility in these materials is strongly affected by their structural and energetic disorder introduced by the defects that ‘trap’ the charge carriers. Depending upon the physical location of the traps and their distribution in energy, they could significantly affect the charge transport in a device. The present work strives to probe the interface and bulk defect states in polymer-based diodes. In lieu of that, a part of the study involved characterizing the device with and without encapsulation, using techniques to record steady-state current-voltage (IV)behaviour, transients of charge extraction by linearly increasing voltage (CELIV) and dark-injection transient currents (DiTC), as well as photoluminescence (PL) and electroluminescence (EL) off the devices. The same characteristics have been carried out to observe the effect of ultra-violet (UV) light-soak on the devices. All the tests were performed on three different polymers, namely P3HT, MDMO:PPV and PCDTBT. The comparison of the encapsulated versus unencapsulated devices gives an insight into characteristic differences in the measurables upon exposure to air and moisture. The light-soak tests indicate the modification of the cathode work function after a UV-assisted oxygen desorption off the polymer/cathode interface. A simultaneous effort went into an in-situ investigation of charge transport dynamics in organic semiconductors over wide time range at a microscopic scale.

Key Words
Organic solar cell, charge transport, encapsulation